Washington University in St. Louis

Washington University Open Scholarship

McKelvey School of Engineering Theses & Dissertations

McKelvey School of Engineering

Winter 12-15-2021

Electrodeless Electrochemistry Enabled by Nonthermal Plasma

Harold Oldham
Washington University in St. Louis

Follow this and additional works at: https://openscholarship.wustl.edu/eng_etds

Part of the Physical Chemistry Commons

Recommended Citation

Oldham, Harold, "Electrodeless Electrochemistry Enabled by Nonthermal Plasma" (2021). *McKelvey School of Engineering Theses & Dissertations*. 730.
https://openscholarship.wustl.edu/eng_etds/730

This Dissertation is brought to you for free and open access by the McKelvey School of Engineering at Washington University Open Scholarship. It has been accepted for inclusion in McKelvey School of Engineering Theses & Dissertations by an authorized administrator of Washington University Open Scholarship. For more information, please contact digital@wumail.wustl.edu.

WASHINGTON UNIVERSITY IN ST. LOUIS

Department of Energy, Environmental & Chemical Engineering

Dissertation Examination Committee:
Elijah Thimsen, Chair
Peng Bai
Marcus Foston
Kimberly Parker
Bryce Sadtler

Electrodeless Electrochemistry Enabled by Nonthermal Plasma

by
Trey Oldham

A dissertation presented to
The Graduate School
of Washington University in
partial fulfillment of the
requirements for the degree
of Doctor of Philosophy

December 2021
St. Louis, Missouri

© 2021, Trey Oldham

Table of Contents

List of Figures v

List of Tables vii

Acknowledgments viii

Abstract of the Dissertation xi

Chapter 1 1

Introduction 1

1.1 Electrified Chemical Processing 1

1.2 Plasma: The Fourth State of Matter 5

1.3 Overview of Dissertation 8

Chapter 2 11

Electrochemical Characterization Method Development 11

2.1 Electrochemical Reaction Equilibria 11

2.2 Characterization of the Reduction Potential 17

2.2.1 Conventional Electrochemical Systems 17

2.2.2 Plasma-Liquid Systems 17

2.3 Experimental 20

2.3.1 Materials 20

2.3.2 Electrochemical Cell Construction 20

2.3.3 Electrochemical Measurements: Metal Electrodes 20

2.3.4 Electrochemical Measurements: Reference Electrodes 21

2.3.5 Double Langmuir Probe Measurements 21

2.4 Results & Discussion 22

2.4.1 Electrochemical Measurements 22

2.4.2 Plasma Conductivity Measurements 26

2.5 Conclusions 29

Chapter 3 32

Electrochemical Characterization of a Plasma-Liquid Interface 32

3.1 Introduction 32

3.2 Experimental 36

3.2.1 Plasma Source 36

3.2.2 Electrochemical Characterization of Plasma-Liquid Interface 37
3.2.3 Colorimetric Assays of Redox Indicators 38
3.2.4 Electrochemical Reduction 39
3.2.5 Spectroscopic Characterization 39
3.2.6 Product Analysis 40
3.2.7 Conductivity Measurements 40
3.2.8 Quantification of Reactive Oxygen and Nitrogen 41
3.2.9 Mass Transport Effects 42
3.3 Results & Discussion 43
3.4 Conclusions 52
Chapter 4 53
Electrochemical Structure of a Plasma-Liquid Interface 53
4.1 Introduction 53
4.2 Experimental 56
4.2.1 Materials 56
4.2.2 Plasma System 56
4.2.3 Spatial Electrochemical Measurements 57
4.2.4 Ultraviolet-Visible Absorption Spectroscopy 58
4.2.5 Multispectral Imaging 59
4.2.6 Multispectral Imaging Processing 60
4.2.7 pH Effects 61
4.3 Results & Discussion 62
4.3.1 Electrochemical Mapping 62
4.3.2 UV-Vis Absorption Spectroscopy 66
4.3.3 Multispectral Imaging 67
4.3.4 pH Independent Redox Indicator 72
4.4 Conclusions 74
Chapter 5 76
Plasma Parameters and the Reduction Potential at a Plasma-Liquid Interface 76
5.1 Introduction 76
5.2 Experimental 79
5.2.1 Plasma Source 79

5.2.2 Light Scattering 81

5.2.3 Electrochemical Characterization 84

5.2.4 Ultraviolet-Visible Absorption Spectroscopy 85

5.2.5 Electrical Characterization 85

5.3 Data Analysis & Fitting 85

5.3.1 Laser Light Scattering 85

5.3.2 Fitting Procedure 89

5.3.3 Floating Potential Calculation 90

5.4 Results & Discussion 91

5.4.1 Laser Light Scattering of Argon Plasma Jet 91

5.4.2 Model Verification using Helium Plasma Jet 101

5.5 Conclusions 104

Chapter 6 105

Concluding Remarks 105

Appendix I 108

Laser Heating 108

Appendix II 112

Effect of Scattering Parameter on Spectral Distribution Function 112

Appendix III 116

Charge and Potential Formation of Floating Surface in Contact with Nonthermal Plasma ... 116

References 124

List of Figures

Chapter 1 1

Figure 1.1. Photovoltaic Module Cost and Shipments 2

Figure 1.2. Conventional Aqeuous Electrochemical Cell...4

Figure 1.3. Plasma in Nature and in Lab 5

Chapter 2 11

Figure 2.1. Electron energy of Cu and Ag...12

Figure 2.2. Electron energy of metal *M* and electrolyte solution *S*...14

Figure 2.4. Schematic depiction of ΔE_{ME} and ΔE_{RE} measurements in galvanic cell 23

Figure 2.5. Measurement of ΔE_{RE} as a function of applied current in Cu-Ag electrochemical cell 26

Figure 2.6. Double Langmuir Curve IV Traces..28

Chapter 3 32

Figure 3.1. Experimental Apparatus..36

Figure 3.2. Negative Relative Reduction Potential at the Plasma-Liquid Interface 42

Figure 3.3. Absorption spectra of redox indicator solutions...45

Figure 3.4. Stability of MV in water..46

Figure 3.5. Effect of Applied RF Power on Electrochemical Parameters 50

Figure 3.6 Effect of Stirring on Reaction Rate 52

Chapter 4 53

Figure 4.1. Atmospheric Pressure Plasma Jet..57

Figure 4.2. Spatial Reduction Potential Distribution Near Plasma-Liquid Interface (PLI) 64

Figure 4.3. UV-Vis Absorption Spectra of Redox Products...65

Figure 4.4. Calibration Curve of Indigo Carmine...67

Figure 4.5. Multispectral Imaging 68

Figure 4.6. Lateral Profiles of Average Absorbance Change 69

Figure 4.7. UV-Vis Absorption Spectrum of $Fe(CN)_6^{3-}/Fe(CN)_6^{4-}$ 72

Figure 4.8. Multispectral Imaging and Lateral Profile of Average Absorbance Change of $Fe(CN)_6^{3-}/Fe(CN)_6^{4-}$ 73

Chapter 5 76

Figure 5.1. Laser Thomson scattering of a radiofrequency argon plasma jet 80

Figure 5.2. Schematic of the experimental laser light scattering setup 83

Figure 5.3. Rotational Raman Spectrum 93

Figure 5.4. Thomson Scattering Spectrum 94

Figure 5.5. Electron density and electron temperature as a function of applied RF power 95

Figure 5.6. Schematic Representation of the charged plasma-liquid interface 96

Figure 5.7. Voltage waveforms for various applied RF powers 98

Figure 5.8. Experimentally measured reduction potential and model predicted potential as a function of RF power 99

Figure 5.9. Ultraviolet-Visible Absorption Spectrum of Indigo Carmine 101

Figure 5.10. Effect of electrolyte Debye length on reduction potential 103

Appendix I 108

Figure AI.1. Electron temperature as a function of laser fluence 111

Appendix II 112

Figure. AII.1. Effect of scattering parameter and electron temperature on spectral distribution function 115

Appendix III 116

Figure AIII.1. Qualitative profiles of electric potential, electron density, and ion density 120

Figure AIII.2. Schematic of Electrically Isolated Substrate Exposed to Nonthermal Plasma 121

Figure AIII.3. Example of Maxwellian Electron Energy Distribution Function (EEDF) for a mean electron temperature of 1 eV 123

List of Tables

Chapter 2 11

Table 2.1: Summary of ΔE_{ME} and ΔE_{ME} for Cu-Ag Galvanic cell 24

Table 2.2: Summary of ΔE_{ME} and ΔE_{ME} for Zn-Cu Galvanic cell 24

Chapter 3 32

Table 3.1: Summary of Reactive Oxygen and Nitrogen Species (RONS) Quantification..........49

Chapter 4 53

Table 4.1: Indigo carmine concentration after plasma treatment 65

Chapter 5 76

Table 5.1: Summary of plasma parameters 96

Appendix III 116

Table AIII.1:Examples of various ion-to-electron mass ratios (M_+/m_e) and electron-to-ion thermal velocity ratios (v_e/v_+) for select ions 117

Acknowledgments

I'd like to thank Dr. Elijah Thimsen for constantly challenging me throughout my Ph.D. while still providing mentorship and guidance along the way. I would also like to thank Drs. Marcus Foston, Kimberly Parker, Bryce Sadtler, and Peng Bai for serving on my committee and their constructive feedback. My deepest gratitude to the late Dr. Palghat Ramachandran for being an endless source of encouragement, inspiration, and motivation while at Washington University.

Thanks to Eugene Kim, Junseok Lee, Anushree Ghosh, Jiayu Li, Phillip Johnson, Jeff Czajka, and Weiyi Pan for keeping me in the loop on department gossip and making seminars a little more bearable. A sincere thanks to my labmates; I truly lucked out by ending up in a lab (or zoo, depending on who you ask) with a strong sense of camaraderie. A big 'preesh to Necip Üner, Qinyi Chen, Kirby Simon, Dr. Xiaoshuang (A.K.A. boss) Chen, Eric Husmann, AJ Cendejas, and Dillon Moher for each teaching me something new and our (way) off-topic chats over the years.

I'm deeply indebted to my friends and family outside of WashU – I could not have made it if it were not for your encouragement, antics, and meme threads. My deepest gratitude to my mom and stepdad who fully supported me without hesitation, despite never completely understanding what it was I was doing. Thanks to Paul and Jamie for revitalizing my creative thinking during my short December breaks with deceptive gift-wrapping. I'm equally thankful to Bailee and Peyton for letting me hide out with them and avoid questions from the "grown-ups" during said breaks. A big shout out to James Williams and Sonia Patel – between casually strolling the (simulated?) streets of Chicago and your mid-pandemic wedding, you two were the best at providing distractions. Thank you to Amanda Bacsko and Taylor Smith for making sure that I'd always take some time off, even if it usually meant I'd be stuck listening to Party in the USA with them (on repeat). Thanks to Clay Jacobs for syncing schedules and sharing in venting/Seoul Taco/Switch power hours. A big thanks to Patrick McKenzie for always indulging my last-minute planning, letting me maintain some level of impulsiveness throughout grad school. I am extremely thankful to Shani Millar-Vaughn and Avni Solanki for their patience/putting up with me in the home stretch. The two of you showed me unrelenting support and were around to provide encouragement when I needed it most.

I want to extend my gratitude to the Davenports who have been there for me since the beginning. I could not have made it without the unconditional support of Devin, Lyra, Maeve, and Charlotte, which came in various forms including trolling, nagging, video chats, and countless voice memos. You really helped me hone my “explain it like I’m 5” skills by ELI5’ing a plasma to an actual five-year-old. Between the 3 AM bedtime story sessions reading K is for Knifeball, sending on-demand piano requests, and outsourcing babysitting Lyra and Maeve to someone on a different continent using only FaceTime – you all played a part in keeping Uncle Choo Choo sane.

Finally, I would like to express my appreciation to Drs. Necip Üner and Qinyi Chen. I cannot begin to express how fortunate I was to have met both of you and would not have make it this far without your assistance. From the Thanksgiving we spent together stressing over our MRS talks, to the one spent searching for cheesecake, the two of you have been there through all of the highs, lows, and everything in between. Even after leaving WashU, you both continued looking out for me. Necip, by setting me up with an opportunity that would otherwise be impossible to find. Qinyi, by forcing me to go over a presentation that she knew I had absolutely not practiced. I’m eternally grateful for making such great friends who always have my back, regardless of any time zone differences (P.S. I think we can finally say that “The Big 3” is complete!).

Trey Oldham

Washington University in St. Louis

December 2021

Dedicated to the memory of Professor Palghat Ramachandran.

ABSTRACT OF THE DISSERTATION

Electrodeless Electrochemistry Enabled by Nonthermal Plasma

by

Trey Oldham

Doctor of Philosophy in Energy, Environmental & Chemical Engineering

Elijah Thimsen, Chair

Washington University in St. Louis, 2021

The increasing availability and decreasing cost of electricity generated by renewable resources have motivated research into electrified chemical processing, whereby electrical energy is used to drive chemical transformations. Electricity-intensive processing techniques such as electrochemistry using solid electrodes has attracted attention in this context for the synthesis of organic compounds, such as high-value pharmaceuticals and renewable chemical production. Selective chemical transformations are achieved in conventional aqueous electrochemical systems by using external circuitry to bias solid electrodes, allowing for the preferential transfer of electrons between the electrode-liquid interface. Despite having the ability to promote controlled electrochemical reactions, configurations using solid electrodes are known to suffer from complications including surface fouling by carbonaceous coatings and are limited by material-dependent operational conditions.

Another way to utilize electricity to drive chemical reactions is by employing nonthermal plasma, which is a partially ionized gas comprised of hot electrons ($T \geq 10000$ K) and relatively cold ions and neutrals that remain at, or near, ambient temperature. Nonthermal atmospheric plasma interacting with liquids act as a potent source of highly reactive species including radicals,

photons, atomic and molecular ions, and electrons, which participate in charge-transfer processes across the interface formed between the plasma and electrolyte solution (i.e. plasma-liquid interface). In turn, these reactive species facilitate reduction-oxidation (redox) reactions within solution without the need of a counter electrode. Thus, plasma-liquid systems are designated as electrodeless electrochemical systems, an approach that is hypothesized to ameliorate the issues of electrode fouling experienced using solid electrodes. Despite these features compared to conventional electrochemical systems, remarkably little is known about the electrochemical nature of the plasma-liquid interface, hindering the ability to rationally design redox reactions.

The work of this dissertation is focused on understanding the fundamental electrochemical structure at a plasma-liquid interface. The first aim of this thesis is the development of a methodology capable of performing *in situ* measurements of the reduction potential in plasma-liquid systems. While the reduction potential is a key parameter in electrochemistry that determines the rate and direction of the redox reaction, a standard protocol for characterization of the reduction potential has not been established for plasma-liquid systems. The second aim of this dissertation is to elucidate the spatial locations of the reduction and oxidation half-reactions in an electrodeless electrochemical system. While the redox half-reactions simultaneously occur on the surfaces of well-defined, solid electrodes in conventional electrochemistry configurations, the absence of solid electrodes obfuscates the locations of the half-reactions (i.e. the electrodeless cathode and anode) in plasma-liquid systems. The final aim of this work is to develop a framework for understanding how to tune the reduction potential in solution, analogous to the external circuitry used in conventional electrochemical systems. More specifically, establishing a correlation between the state variables of the plasma (i.e. electron temperature and electron density) and the reduction potential in solution.

Chapter 1

Introduction

1.1 Electrified Chemical Processing

The global capacity of renewable energy, specifically in the form of solar photovoltaics (PV), surpassed 500 GW at the end of 2018, with an estimated projection of an additional to be installed by 2023.[1] As shown in Figure 1.1a, the average cost of PV modules has rapidly decreased from \$3.50 to 0.38 per peak watt from 2006 to 2020, respectively.[2] Similarly, the number of PV module shipments increase from 0.3 to 21.7 million peak kilowatt from 2006 to 2020, respectively, as shown in Figure 1.1b.[2] As such, the increasing abundance and decreasing costs of producing electricity from renewable resources has given rise to interest in novel electricity-intensive processing techniques. In the context of chemical processing, electricity-intensive techniques utilize electrical energy as inputs to promote otherwise non-spontaneous reduction-oxidation (redox) reactions, as opposed to chemical reagents used in chemical-based approaches. Here, a redox reaction refers to a type of chemical transformation in which the oxidation state, or charge state, of atoms are changed as a result of an electron transfer processes.

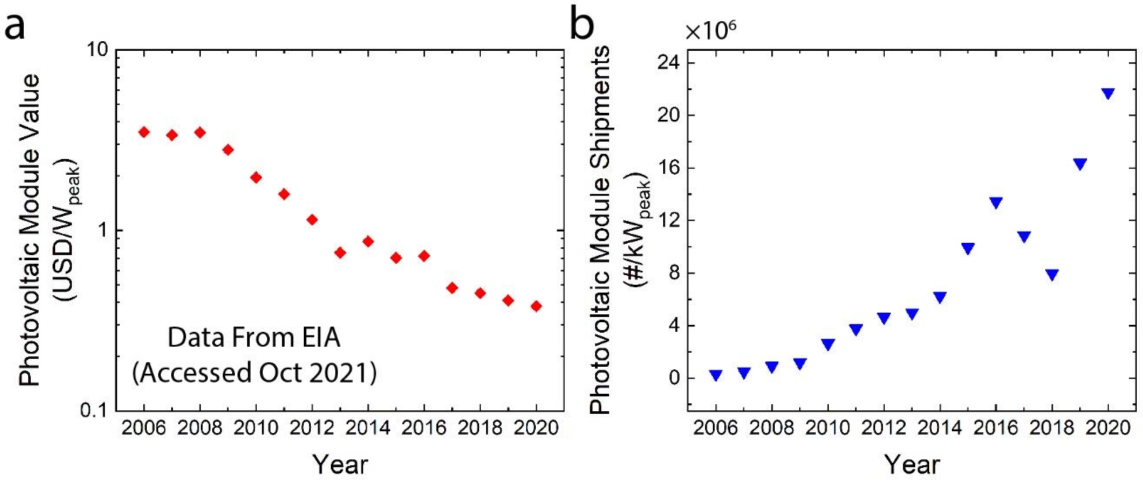

Figure 1.1. Photovoltaic Module Cost and Shipments. (a) Average cost of photovoltaic module in USD per peak watt and (b) number of photovoltaic module shipments in millions per peak kilowatt from 2006-2020.[2]

The driving force for redox reactions in chemical reduction processes arises from differences in the energies of the electrons between chemical reagents. More specifically, electrons are transferred from a chemical species with high energy electrons to another species to minimize the total electron energy. Chemical reduction becomes more challenging in the case of aromatic compounds due to the intrinsic stability of their chemical bonds. In order to reduce these bonds, reactions using chemical reagents capable of generating free electrons in solution, or solvated electrons,[3] are required. Such reactions, such as Birch reduction,[4] have been utilized industrially, such as the case of Pfizer's synthesis of an anti-Parkinson's drug candidate sumanirole.[5,6] However, the generation of solvated electrons in these processes requires harsh chemical environments including the use of pyrophoric alkali metals as reagents in a solvent of liquid ammonia at cryogenic temperatures (–35 °C). While milder alternatives have been proposed,[7,8] these methods still rely on the use of alkali metals. Another approach to promote Birch reduction is through electrochemical reduction.[9]

Electrochemical reduction is distinct from chemical reduction in that electrons are provided by an electrically conductive electrode rather than a chemical reagent. In electrochemical reduction, the energy of electrons in the electrode is modulated using an external power supply in order to preferentially transfer electrons from the electrode to the species of interest. An electrochemical approach allows for the precise tuning of electron energy in the electrode to selectively promote the reaction of interest. In the context of the Birch reduction reaction, electrochemical reduction has been demonstrated to offer a scalable alternative for synthesizing pharmaceutically relevant molecules and can be performed under ambient conditions using non-toxic reagents.[9]

In conventional aqueous electrochemistry systems, vessels known as electrochemical cells are used to perform electrochemical experiments (Figure 1.2). In general, the components of an electrochemical cell include solid electrodes which are immersed in an inert solvent containing an electrolyte. A typical electrochemical experiment is only concerned with the reduction and/or oxidation of a single analyte, which reacts at the working electrode. The working electrode is in electrical contact with a counter electrode, where the complementary redox reaction takes place. Given the fact that redox reactions can be driven by carefully tuning electron energy in an electrode, careful monitoring of the reduction potential at the electrode-electrolyte interface is crucial. As the reaction of interest occurs at the working electrode, experimentalists are only concerned with monitoring and maintaining the potential at this electrode-electrolyte interface. A reference electrode, an electrode with a well-defined and stable equilibrium potential, is used to measure the potential across the working electrode-electrolyte interface. An external power supply, such as a potentiostat, is used to control the applied bias of the working electrode with respect to the counter electrode as a function of the voltage measured between the working and reference electrode.

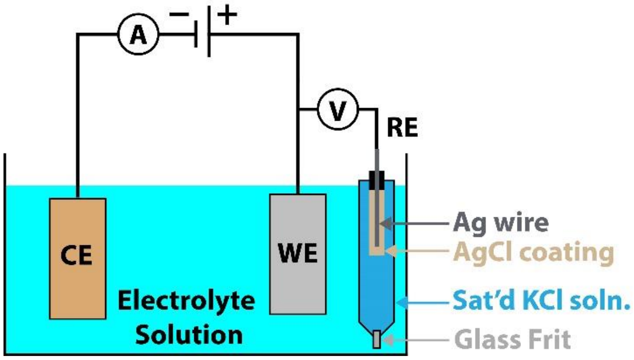

Figure 1.2. Conventional Aqeuous Electrochemical Cell. Schematic representation of a conventional electrolytic cell where current is passed between the counter electrode (CE) and working electrode (WE), while the potential at the working electrode-solution interface is monitored by a reference electrode (RE).

Despite the ability to perform highly selective chemical transformations, conventional electrochemical systems also have their drawbacks. In particular, electrochemical cells using solid electrodes are known to suffer from fouling of the electrode surface by carbonaceous coatings.[10–12] Additionally, the electrode is limited to a certain voltage operational window determined by the material of the electrode.[13] Another way to utilize electricity to drive chemical reactions by using nonthermal plasma. Free plasma jets in contact with liquids are able to promote electrochemical reactions without the need of solid electrodes. An electrodeless approach is hypothesized to ameliorate the issues of electrode fouling while simultaneously circumventing the material-dependence limitation of solid electrodes. Furthermore, the addition of a supporting electrolyte, which has been shown to impact chemical conversion in conventional electrochemical systems,[14] is not required in plasma-liquid systems.

1.2 Plasma: The Fourth State of Matter

Plasma describes a partially ionized gas containing free electrons, ions, neutrals (atoms, molecules, radicals), and energetic photons. A more rigorous description of a plasma is a quasi-neutral gas comprised of charged and neutral particles whose interactions are predominantly collective. Here, quasi-neutrality requires that total number of electrons and ions (multiplied by their charge number) are approximately zero, such that the medium is macroscopically electrically neutral. Collective effects refer to the long-range attractive and repulsive forces experienced between a single charged particle simultaneously interacting with many free electrons and ions. Due to these unique properties, plasma is considered the fourth fundamental state of matter.

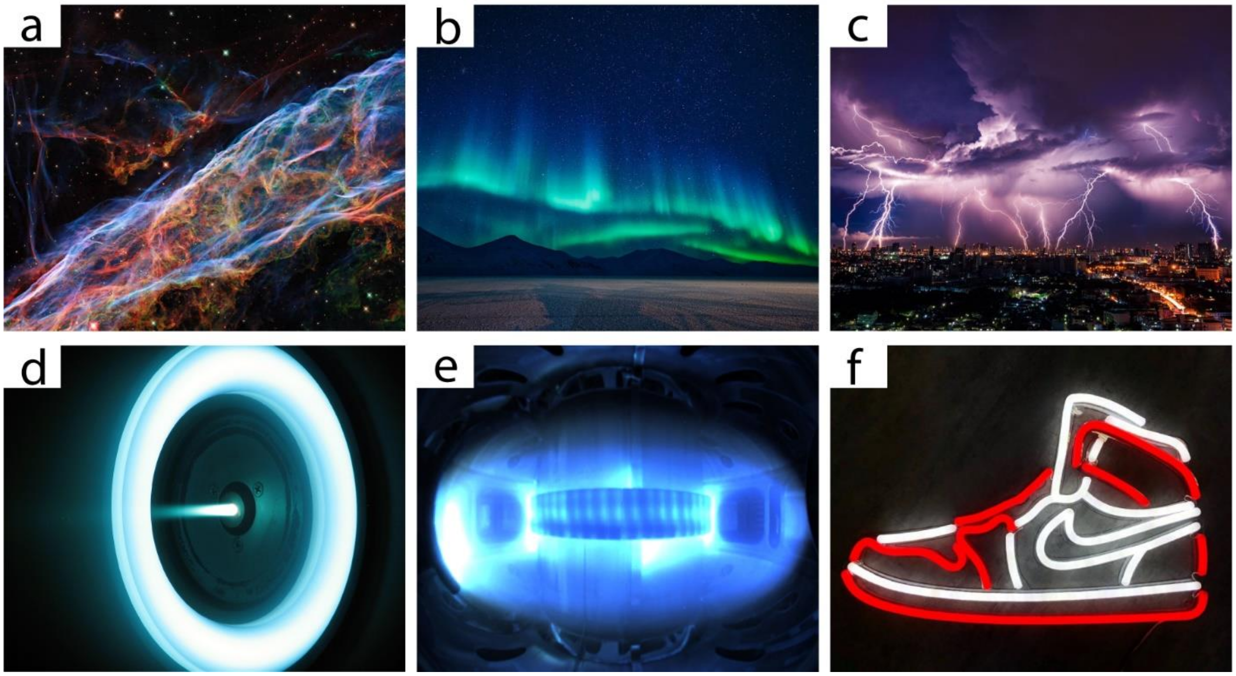

Figure 1.3. Plasma in Nature and in Lab (a) The Veil nebula is an example of an astrophysical plasma generated from by a supernova, with light emission due to hydrogen (red), sulfur (green), and oxygen (blue).[15] (b) The aurora borealis is an example of a terrestrial plasma, caused by the solar wind entering Earth's upper atmosphere.[16] (c) Lightning is another example of a terrestrial plasma.[17] (d) A Hall-effect thruster is an example of an artificially produced plasma generated using xenon.[18] (e) A tokamak is a type of fusion reactor that uses strong magnetic fields to confine plasma in the shape of a torus.[19] (f) Neon lighting is an example a type of gas-discharge lamp that uses various gases to produce lighting.[20]

Plasma is a ubiquitous phase of matter, which naturally occurs in the form of astrophysical (Figure 1.3a) and terrestrial (Figures 1.3b-c) sources. Artificially generated plasmas have been found to be particularly useful for both industrial and scientific research (Figures 1.3d-e). Given the vast variety of artificially produced plasmas, it is useful to describe the plasma based on characteristic features such as temperature, pressure, generation source, etc. The most common classification of plasma is based on the relative temperatures of the constituent particles. More specifically, based on the relative temperatures of the electrons (T_e), ions (T_i), and background gas (T_g) the plasma can be classified as either being a thermal or nonthermal plasma.[21,22]

A thermal plasma, or an equilibrium plasma, refers to a system in which the electrons, ions, and background gas are in thermal equilibrium with one another $T_e \approx T_i \approx T_g$. The typical temperature range of a thermal plasma is on the order of $T \geq 11600$ K, or equivalently, $k_BT \geq 1$ eV.[22,21] Given the high temperatures of species in the plasma, it is conventionally to discuss the temperatures are conventionally described in terms of electronvolts (eV) by multiplying the temperature by the Boltzmann constant, k_B. To give a sense of numbers, room temperature T = 298 K corresponds to approximately $k_BT = 0.026$ eV. Nonthermal plasmas refer to multiiple-temperature systems, where the temperature of the electrons are on the order of $k_BT_e \geq 1$ eV, while the ions and background gas remain at, or near, ambient temperature $T_i \approx T_g$.[21,22] The large discrepancy in the temperatures of the electrons and ions in a nonthermal plasma is due to the preferential heating of the less massive and more mobile electrons. In addition to the temperatures of the constituent particles of a plasma, another important metric is the density of charged species. Here, it is customary to describe the plasma density based using a number density, which is the number of particles occupying a particular volume. For low pressure nonthermal plasmas used for semiconductor processing, typical electron densities, n_e, are on the order of 10^{14}-10^{19} m^{-3}.[22] For comparison, the number density of gas molecules, n_g, at atmospheric pressure and room temperature is roughly on the order of 10^{25} m^{-3}.

Owing to their unique features, nonthermal plasmas are used for a wide variety of applications including material processing,[23] lighting devices,[24] and nanomaterial synthesis.[25] Until recently, the majority plasma sources used for research and industrial applications operated at low pressures (1 mTorr – 1 Torr).[22] In terms of plasma-surface interactions, research was limited to solid surfaces or solvents with very low vapor pressures.[26] More recently, nonthermal plasma sources able to operate at atmospheric pressure (760 Torr) have extended the breadth of applications for plasma technology. The use of atmospheric pressure plasma jets (APPJs) have been used for applications including surface cleaning,[27,28] dry etching,[29,30] and adhesive bonding.[31,32] Nonthermal atmospheric pressure plasmas have also enabled the study of plasma-liquid interactions, which is the focal point of this work.

Nonthermal atmospheric pressure plasmas in contact with liquids have shown great potential for applications including for rapid would healing,[33–35] wastewater treatment,[36–39] and nanomaterial synthesis.[40–43] These applications utilize the fact that exploit how plasmas operating in ambient air produce a variety of reactive gas phase species which can dissolve into the liquid phase and react at the plasma-liquid interface.[34,44] Species such as water vapor, oxygen, and nitrogen react in the gas phase and dissolve in the liquid, generating long-lived reactive oxygen and nitrogen species (RONS) including H_2O_2, NO_3^-, and NO_2^-.[45] The long-lived RONS are typically associated with promoting oxidation reactions within the liquid phase, and are the basis for the subset of plasma-liquid interactions known as plasma-activated water (PAW).[46] Plasmas generated using noble gases (*e.g.* helium, argon) operating in open air act as a source of free electrons and ions in the gas phase. Liquid-facing plasmas can inject free electrons into aqueous solutions thereby generating solvated electrons.[47,48] In turn, the solvated electrons are able to promote reduction reactions within the liquid, such as the reduction of metallic salts into metal nanoparticles.[40] Similarly, plasmas consisting of noble gas and hydrogen mixtures have been shown to produce atomic hydrogen, a highly reducing species, which was used to mediate the reduction of silver ions into metallic nanoparticles.[49]

Clearly, plasma-liquid interactions are capable of promoting both reduction and oxidation reactions within electrolyte solution, giving rise to the emerging field of plasma electrochemistry.[50] Free atmospheric pressure plasmas are able to act as an electrodeless systems, which is hypothesized to circumvent the fouling issue experienced in the case of solid electrodes. Furthermore, plasma electrochemical cells have been shown to produce highly reducing species such as solvated electrons, which would otherwise require harsh chemical environments to generate.[4,51] Despite these advantages over conventional electrochemical cells, plasma-liquid systems have not been evaluated from an electrochemistry perspective. More specifically, key parameters used to achieve highly selective chemical transformations, such as the reduction potential, are often overlooked in plasma-liquid systems. In order to rationally design plasma electrochemistry systems to promote desired chemical transformations, it is important to first elucidate the electrochemical structure in an electrodeless system.

1.3 Overview of Dissertation

The ability to perform electrochemical reactions without electrodes makes nonthermal plasma an excellent candidate for electrified-chemical processing. However, there are a number of challenges that must be addressed in order for plasma electrochemistry to be a viable means of performing controlled electrochemistry. The purpose of this dissertation is to evaluate plasma-liquid systems using fundamental electrochemistry concepts rather than the conventional plasma physics approach. The structure of the dissertation is as follows:

Chapters 2 provides a brief overview of fundamental concepts in electrochemistry to set the stage for understanding plasma electrochemistry. Based on these principles, an experimental method for characterizing the reduction potential in plasma-liquid systems is proposed and tested using well-defined, electrochemical cells with known reduction potentials.

Chapter 3 applies the electrochemical characterization toolkit introduced in Chapter 2 to characterize the reduction potential near a plasma-liquid interface. Spectrophotometric methods performed on plasma-treated molecular colorimetric redox indicators are used to independently verify the results of the reduction potential measurements.

Chapter 4 expands upon the work of Chapter 3, performing spatial measurements of the reduction potential in order to elucidate the locations of the anode and cathode in an electrodeless electrochemical system. In addition to electrochemical characterization, *in situ* visualization of the spatial distribution of molecular colorimetric redox indicators is used as independent confirmation of the locations of the half-reactions determined by the spatial electrochemical measurements.

Chapter 5 explores the relationship between the plasma parameters (electron temperature and electron density) in the gas phase to the reduction potential in solution. More specifically, the measured plasma parameters are used as model inputs for predict the reduction potential at the plasma-liquid interface and compared to experimentally measured reduction potentials.

Chapter 2

Electrochemical Characterization Method Development

2.1 Electrochemical Reaction Equilibria

Given the focus on plasma electrochemistry in this dissertation, a brief overview of key concepts in conventional electrochemistry will help set the stage for understanding reduction-oxidation (redox) reactions at the plasma-liquid interface. Redox reactions are a result of electron-transfer processes occurring at the interface formed between dissimilar phases in order to establish electrochemical equilibrium. More specifically, the driving force for electron transfer processes arises from differences in the electrochemical potentials of electrons, $\overline{\mu}_e$, between separate phases that are brought into electrical contact. Note that the electrochemical potential of electrons is equivalent to the Fermi level, E_F, used to discuss energy levels in solid state physics.[52]

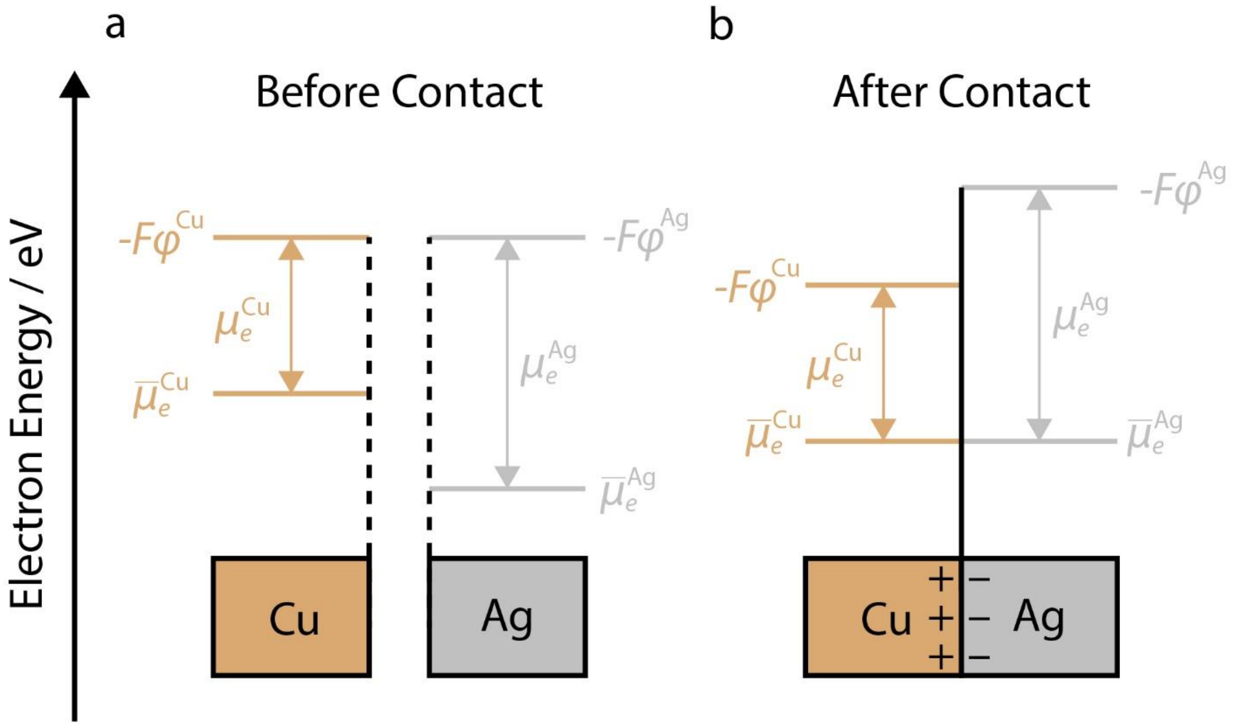

Figure 2.1. Electron energy of Cu and Ag. Diagram of electron energy ($\bar{\mu}_e$) of Cu metal and Ag metal (a) before and (b) after brought into contact. Chemical potential of electrons given by μ_e while electrostatic potential energies are given by $F\varphi$.

Before discussing electrochemical equilibrium in the context of electrochemical cells, let us first consider the simple case of two different metals that are initially electrically isolated from one another, such as the case of silver (Ag) and copper (Cu) shown in Figure 2.1a. In this example, the electrochemical potential of electrons in phase β (*i.e.* Ag or Cu), $\bar{\mu}_e^\beta$, can be expressed as the sum of the chemical potential and electrostatic potential energy given by[53]

$$\bar{\mu}_e^\beta = \mu_e^\beta + z_e F\varphi^\beta \tag{2.1}$$

where μ_e^β is the chemical potential of electrons in phase β, z_e is the charge number of an electron ($z_e = -1$), F is the Faraday constant, and φ^β is the electrostatic potential in phase β. To avoid confusion with the various usages of “potential” used in the electrochemistry literature, the electrochemical potential of electrons ($\bar{\mu}_e$) will be referred to electron energy herein. When the two metals are brought into electrical contact, electrons from the metal with the greater electron energy $\overline{\mu}_e$ (higher Fermi level) will be transferred to the metal with the lower electron energy (lower Fermi level) in order to equilibrate their electron energies (Figure 2.1b). In the case of Ag and Cu, the equilibrium expression would be

$$\overline{\mu}_e^{Cu} = \overline{\mu}_e^{Ag} . \tag{2.2}$$

To satisfy this condition, the electrons in Cu, which are initially higher in energy, are transferred to Ag. Using Equation 2.1 to express the equilibrium condition in terms of the chemical potential and electrostatic potential energy of each metal yields

$$\mu_e^{Cu} - F\varphi^{Cu} = \mu_e^{Ag} - F\varphi^{Ag} . \tag{2.3}$$

Introducing a simplifying expression for the change in electrostatic potential, $\Delta\varphi$, given by

$$\Delta\varphi = \varphi^{Ag} - \varphi^{Cu} \tag{2.4}$$

and similarly, an expression for the change in chemical potential of electrons expressed as

$$\Delta\mu_e = \mu_e^{Ag} - \mu_e^{Cu} \tag{2.5}$$

Equation 2.3 can be rearranged and simplified to relate the change in electrostatic potential to the change in chemical potential of electrons by

$$\Delta\varphi = \frac{\Delta\mu_e}{F} . \tag{2.6}$$

Here, we see that bringing two separate metals into electrical contact with one another (*i.e.* creating a short-circuit) forces their electron energies to become equal. As a result, a flow of electrical

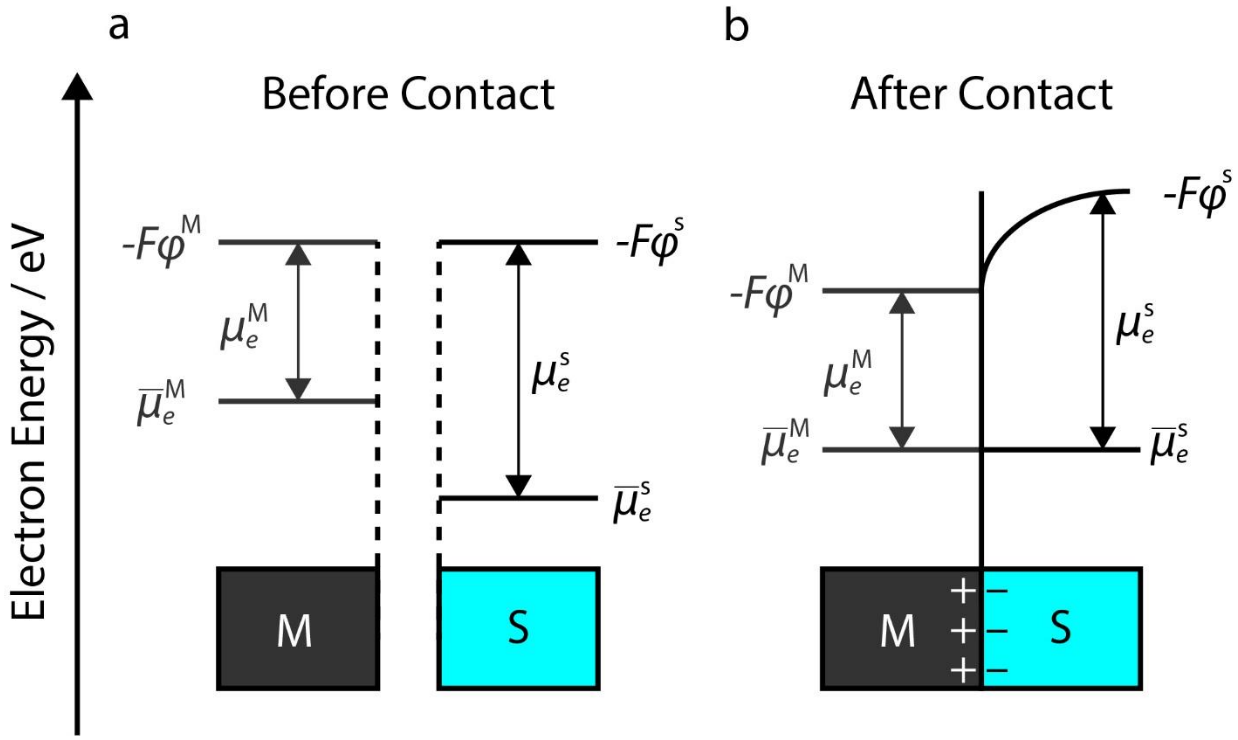

Figure 2.2. Electron energy of metal *M* and electrolyte solution *S*. Diagram of electron energy ($\bar{\mu}_e$) of metal *M* and electrolyte *S* (a) before and (b) after brought into contact. Chemical potential of electrons given by μ_e while electrostatic potential energies are given by $F\varphi$.

current develops and induces an electrostatic potential difference with a magnitude that is related to the difference in electron energy prior to contact.

Extending the discussion of electrochemical equilibrium in the context of electrochemical cells, consider a half-cell comprised of a solid metal electrode immersed in an aqueous electrolyte solution. The electrolyte contains a redox couple containing both the oxidized (*O*) and reduced (*R*) forms, which react reversibly with the general form

$$v_O O + ne \rightleftarrows v_R R \tag{2.7}$$

where v_O and v_R are the stoichiometric coefficients for *O* and *R*, respectively, *n* is the number of electrons taking part in the charge-transfer reaction, and *e* is an electron residing in the metal electrode. Prior to establishing contact between the metal electrode and electrolyte (Figure 2.2a), the ‘Fermi level’ of the solution, $\overline{\mu}_e^s$, can be written as[54]

$$\overline{\mu}_e^s = \frac{\overline{\mu}_R^s - \overline{\mu}_O^s}{n} = \overline{\mu}_e^{R/\mathrm{O}} \ . \tag{2.8}$$

where $\overline{\mu}_R^s$ and $\overline{\mu}_O^s$ are the electrochemical potentials of the *R* and *O* forms of the redox couple in the solution, respectively, and $\overline{\mu}_e^{R/O}$ is the electron energy of the *R/O* redox couple. Similar to the previous case, when the metal electrode and solution are brought into contact, the initial difference in their electron energies drives a charge transfer process between the phases thereby creating an electrostatic potential difference. Setting the electron energies of the metal and solution equal to one another, the chemical potential and electric potential energies can be related as follows

$$\varphi^M - \varphi^{R/\mathrm{O}} = \frac{\mu_e^M - \mu_e^{R/\mathrm{O}}}{F} \tag{2.9}$$

where φ^M and μ_e^M are the electrostatic and chemical potentials for the electrode made comprised of metal *M* in the electrochemical half-cell (Figure 2.2b). Taking this a step further, we can introduce the reduction potential, *E*, which can be defined as[55,56]

$$E = -\frac{\mu_e}{F} \ . \tag{2.10}$$

Note, this expression is with respect to the vacuum level. The chemical potential of electrons in Equation 2.10 is replaced with the electron energy when taken with respect to an arbitrary reference point. Combining Equations 2.1 and 2.10, Equation 2.9 can be re-written as

$$\varphi^{M} - \varphi^{R/\mathrm{O}} = E_{R/O} - E_{M} \ . \tag{2.11}$$

Here, we see that the electrostatic potential difference formed when the metal and solution are brought into contact is equal to the differences in the reduction potentials of the two phases prior to contact. In the case of the *R/O* redox couple, a concentration dependence on the relative composition of the solution can be introduced by expanding the chemical potential term as[53]

$$\mu_e^{R/O} = \mu_e^{*R/O} - \frac{R_g T}{n} \ln\left(\frac{C_R^{\nu_R}}{C_O^{\nu_O}} \right) \tag{2.12}$$

where $\mu_e^{*R/O}$ is the standard state chemical potential of electrons for the *R/O* redox couple, R_g is the gas constant, T is the absolute temperature, and C_R and C_O are the molar concentrations of R and O, respectively. Dividing both sides by the Faraday constant, we arrive at the Nernst equation[13]

$$E_{R/O} = E_{R/O}^{\circ} + \frac{R_g T}{nF} \ln\left(\frac{C_O^{\nu_O}}{C_R^{\nu_R}} \right) \tag{2.13}$$

where $E_{R/O}^{\circ}$ is the standard reduction potential for the *R/O* redox couple. Similar to the cases of two different metals brought into contact, Equation 2.11 demonstrates that charge transfer is initiated between the metal and electrolyte solution are brought into contact that produces an electrostatic potential difference. In this case, the induced electrostatic potential difference is equal to the differences in the reduction potentials between the solution and the metal prior to contact. For a redox couple in solution, the differences in reduction potentials can be tuned by adjusting the concentrations of R and O in the solution.

2.2 Characterization of the Reduction Potential

2.2.1 Conventional Electrochemical Systems

In conventional electrolytic cells, highly selective chemical transformations are achieved by controlling the reduction potential at the electrode-electrolyte interface. In a conventional electrolytic cell, a three-electrode configuration is adopted where the reduction and oxidation reactions take place on the surfaces of the working and counter electrodes, which are connected via an external circuit. Given that the reaction of interest occurs at the working electrode, the reduction potential at the electrode-electrolyte interface is monitored using a reference electrode, which is an electrode maintains a constant, well-defined known voltage. The measured voltage difference between the working electrode and reference electrodes is referred to as the electrode potential. The external circuit is used to bias to the working electrode, and any changes in the measured electrode are used as a feedback loop to adjust the applied bias. The key idea behind these systems is that the working electrode constrains the local reduction potential in solution to a particular value and that the redox reactions proceed in the direction to reach local equilibrium with that reduction potential.

2.2.2 Plasma-Liquid Systems

Nonthermal plasma in contact with liquids yield a variety of reactive species including free electrons, atomic and molecular ions, radicals, and high energy photons. These excited species can be transported from the gas phase into the liquid, initiating charge-transfer reactions at the interface formed between the plasma and liquid.[57] The plasma-liquid interface is an electrochemical interface that has been utilized to perform electrochemical reactions including carbon dioxide reduction,[58,59] nitrogen fixation,[60,61] and the hydrogen evolution rection.[62] Plasma-produced species including atomic hydrogen[49] and solvated electrons[47,63] have been shown to reduce metal salts into colloidal nanoparticles,[64–66] while reactive oxygen and nitrogen species (RONS) have been used for oxidation reactions in the plasma activated water (PAW) literature.[67–69] Despite the fact that the plasma-liquid interface has been used to promote reduction-oxidation (redox) reactions, only a few reports evaluating the reduction potential at the plasma-liquid interface exist.[57,70]

The PAW literature is typically concerned with characterizing the so-called oxidation-reduction potential (ORP) of solutions before and after plasma treatments, using a device known as an ORP sensor.[70] The operating principle of an ORP sensor is based on immersing an inert metal electrode, typically a platinum wire, in the test solution.[71] When brought into contact with the solution, the Pt electrode and species within the solution will exchange electrons in order to equilibrate and produce an electric potential, which is measured with respect to a reference electrode, typically a saturated silver-silver chloride (Ag/AgCl) electrode. While ORP measurements are useful for understanding the net redox behavior of solutions exposed to plasma, these offline measurements are not particularly useful for understanding how to use plasma-liquid systems for controlled electrochemistry.

Identifying and characterizing an equivalent parameter to the electrode potential measured conventional electrochemical systems is not a straightforward matter in plasma-liquid systems. Even in the case plasma-assisted electrochemistry configurations, the significant voltage drop across the plasma prevents the implementation of a reference electrode near the plasma-liquid interface.[50] Rather than measuring the voltage near the plasma-liquid interface relative to an external reference, a more useful measurement would be one made relative to the unaffected bulk solution. Measuring differences in the local electrostatic potential in electrolyte solutions using reference electrodes has been used in various research fields.[72,73] In the corrosion literature, the scanning reference electrode technique (SRET) uses identical reference electrodes to sense ionic current within solution in order to monitor localized corrosion in real-time.[74,75] The SRET method is also used to identify local anodic and cathodic regions in solution based on the relative values of the voltage differences.[74,76] The voltage difference measured identical reference electrodes is related to (ionic) current in solution by Ohm's law using[77,78]

$$\boldsymbol{j} = -\sigma \nabla \varphi \tag{2.14}$$

where $\boldsymbol{j}$ is the current density, σ is the electrical conductivity of the solution, and $\nabla \varphi$ is the spatial gradient in the electrostatic potential.

While SRET has clearly demonstrated the ability to identify anodic and cathodic regions in solution, the applicability of this method to characterize electrodeless electrochemical systems has not been addressed or investigated. Herein, the purpose of this work is to determine if the voltage measured between identical reference electrodes within solution can be used to assess the reduction potential in solution using well-defined electrochemical systems. More specifically, the method will be used to measure the reduction potential in galvanic and electrolytic cells under controlled conditions. Recall that the magnitude of the electrostatic potential is equal to the difference in reduction potentials of the phases involved in the reaction. Given that the current density sensed by the reference electrodes is related to the spatial gradient of the electrostatic potential, the hypothesis is that the measurement should be proportional to the reduction potential of the electrochemical cell if the solution is the largest resistance to current flow. The applicability to plasma-liquid systems will be evaluated based on estimates of the relative conductivities between the plasma and solution.

2.3 Experimental

2.3.1 Materials

Copper (II) nitrate trihydrate (purum p.a., 98.0-103%), silver nitrate (ACS reagent, ≥99.0%), zinc nitrate hexahydrate (reagent grade, 98%), sodium nitrate (ReagentPlus®, ≥99.0%) agar powder, and potassium chloride solution (~3 M KCl, saturated with silver chloride) were purchased from MilliporeSigma. All chemicals were used as received without further purification. All solutions were prepared using Type III ultrapure (18.2 MΩ cm) water from a Direct-Q 3 Water Purification System (MilliporeSigma). Copper (trace metals basis, 99.98%), silver (trace metals basis, 99.99%), and zinc (trace metals basis, 99.9%) were purchased from MilliporeSigma.

2.3.2 Electrochemical Cell Construction

Electrochemical cells were constructed by preparing individual half-cells in 180 mL glass crystallizing dishes. The Ag, Cu, and Zn electrodes were rectangular metal strips with nominal dimensions of 5 mm × 25 mm. Solutions of $AgNO_3$, $Cu(NO_3)_2$, and $Zn(NO_3)_2$ were each prepared in concentrations of 0.01 M and 1.00 M. The salt bridge used to complete the electrochemical cell was constructed by bringing a 100 mL solution of 2.0 M $NaNO_3$ containing 1.00 g of agar to a boil.

2.3.3 Electrochemical Measurements: Metal Electrodes

The voltage differences of the metal electrodes of the Cu-Ag and Zn-Cu galvanic cells were measured using a source meter unit (SMU, Model 2400, Keithley), sourcing a current of $i = 0.0$ mA and measuring the voltage. For the Cu-Ag electrochemical cell, the positive lead was attached to the Ag electrode and referenced to the Cu electrode for both the galvanic and electrolytic cell configurations. In the case of the Zn-Cu galvanic cell, the positive lead was connected to the Cu electrode and referenced to the Zn electrode.

2.3.4 Electrochemical Measurements: Reference Electrodes

The voltage difference between identical Ag/AgCl reference electrodes using a digital multimeter (DMM6500, Keithley) under short-circuit conditions. For the Cu-Ag electrochemical cell, the reference electrode taken to be the positive lead was placed in the Ag half-cell and measured with respect to the reference electrode in the Cu half-cell for both the galvanic and electrolytic cell configurations. The voltages difference in the Zn-Cu galvanic cell was measured taking the reference electrode in the Cu half-cell to be the positive lead and measured with respect to the Zn half-cell.

2.3.5 Double Langmuir Probe Measurements

The plasma conductivity was determined using a double Langmuir probe (DLP, Impedans LTD) using platinum tips that were 0.36 mm in diameter, 1.5 mm in length, and separated by a spacing of 3.0 mm. The plasma source characterized was a helium atmospheric pressure plasma jet (APPJ) generated a radiofrequency (RF, 13.56 MHz) power supply (AG 0613, T&C Power Conversion) connected to an impedance matching network (AIT-600 RF Auto Tuner, T&C Power Conversion). The powered electrode was an aluminum ring mounted on a fused silica tube with inner and outer diameters of 7 and 9.5 mm, respectively. An identical aluminum ring electrode was connected to ground and mounted at a lower position on the tube. The spacing between the powered and grounded electrodes was 9.5 mm. The helium flow rate was maintained at 30.5 standard liters per minute by means of a critical flow orifice that was 300 µm in diameter. The plasma was generated using an applied RF power of 200 W in open air, operating as a free jet. The platinum tips of the DLP were positioned 10 mm below the end of the APPJ tube ending and centered about the luminous region of the plasma. The DLP probe tips were biased over the range of −100 to +100 V in increments of 1 V, while simultaneously measuring the resulting current. Approximating the DLP geometry using a parallel axis (paraxial) cylinder model, where the interelectrode voltage and current can be used to calculate the electrical conductivity between the cylinders, current-voltage (IV) traces from the DLP measurements were used to approximate the plasma conductivity.

2.4 Results & Discussion

2.4.1 Electrochemical Measurements

The goal of this work was to understand if the measured voltage difference between identical reference electrodes could be used as a tool to characterize the reduction potential in solution using well-defined electrochemical systems. To address this, we perform a comparative study evaluating the voltage differences measured between (i) solid metal electrodes and (ii) reference electrodes which are in separate half-cells in a well-defined electrochemical cell. The voltage difference between metal electrodes, ΔE_{ME}, was measured under open-circuit conditions (*i.e.* $i = 0.0$ mA) taking the metal with the more positive reduction potential to be the positive lead of the voltmeter and the metal with the more negative reduction potential to be the negative lead. The voltage difference between reference electrodes, ΔE_{RE}, was determined under closed-circuit conditions (*i.e.* $i \neq 0.0$ mA) measuring the local potential of a reference electrode in the electrolyte solution of the half-cell containing the metal with the more positive reduction potential with respect to an identical reference electrode in the electrolyte of the half-cell containing the metal with the more negative reduction potential. Note that the measurements of ΔE_{ME} and ΔE_{RE} were performed under different operating conditions for the galvanic cells. This is due to the fact that

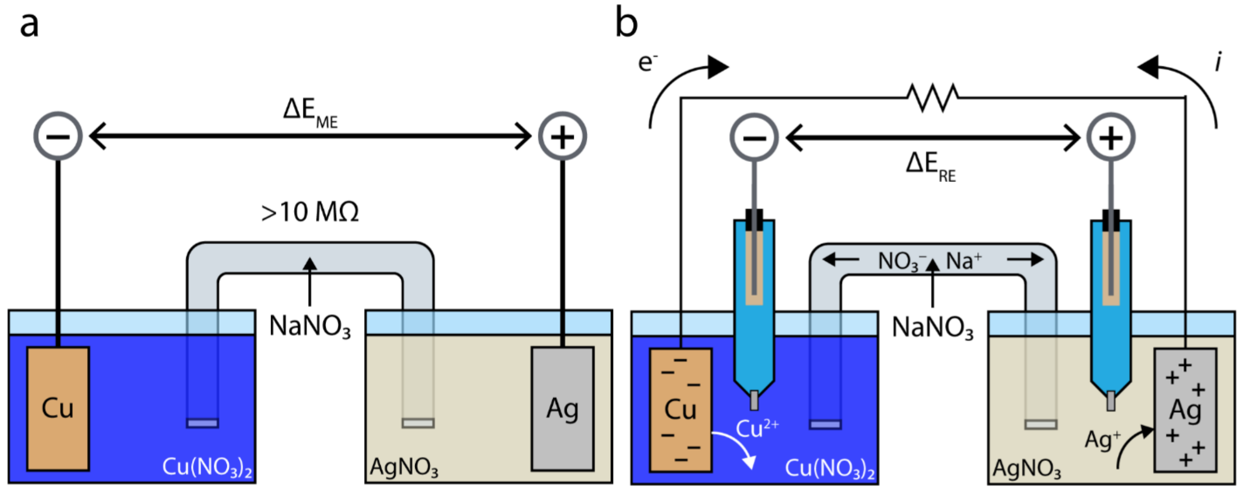

Figure 2.4. Schematic depiction of ΔE_{ME} and ΔE_{RE} measurements in galvanic cell. (a) Schematic representation of ΔE_{ME} measurement procedure, where the voltage was measured between the metal electrodes under open-circuit conditions. (b) Schematic illustrating the procedure for ΔE_{RE} measurements, where identical Ag/AgCl reference electrodes were measuring the local potentials in solution under short-circuit conditions. In both cases, the measured voltages were taken with the positive lead going to the Ag/Ag^+ half-cell and referenced to the negative lead in the Cu/Cu^{2+} half-cell.

ΔE_{ME} was nominally 0.0 V under closed-circuit conditions, and ΔE_{RE} was nominally 0.0 V under open-circuit conditions.

A schematic illustrating how the ΔE_{ME} and ΔE_{RE} measurements were performed for the Cu-Ag galvanic cell is shown in Figure 2.4, with the values of the measurements for various concentrations of $AgNO_3$ and $Cu(NO_3)_2$ listed in Table 2.1. Recall that the cell potential various as a function of concentration given by the Nernst equation in Equation 2.13. In galvanic cells, the cell voltage is taken to be the difference in reduction potentials of the cathode (*i.e.* half-cell where reduction occurs) and the anode (*i.e.* half-cell where reduction occurs). Given this convention, $\Delta E_{\mathrm{ME}} = E_{\mathrm{Ag}} - E_{\mathrm{Cu}}$ is equivalent to the measurement of the cell voltage. The most striking difference between the two measurement techniques is that the magnitudes are similar (*i.e.* $|\Delta E_{\mathrm{ME}}| \approx |\Delta E_{\mathrm{RE}}|$) for each combination of $AgNO_3$ and $Cu(NO_3)_2$ concentrations, but the signs of the measured voltages are opposite of one another (*i.e.* $\Delta E_{\mathrm{ME}} \approx -\Delta E_{\mathrm{RE}}$). A similar trend between the ΔE_{ME} and ΔE_{RE} measurements was also observed in the case of the Zn-Cu galvanic cell, which is summarized in Table 2.2. Namely, the magnitudes of both measurements were similar for the different combinations of $Cu(NO_3)_2$ and $Zn(NO_3)_2$ concentrations, but the signs were opposite of one another. Thus, the reference electrode method appears to be able to measure the magnitude of the cell voltage, which is related to the reduction potential difference between the half-cells, but consistently measured the opposite sign compared to the ΔE_{ME} measurements of the cell voltage.

Table 2.1: Summary of ΔE_{ME} and ΔE_{ME} for Cu-Ag Galvanic cell. Measured values of ΔE_{ME} performed under open-circuit conditions and ΔE_{RE} performed under short-circuit conditions for the Cu-Ag galvanic cell for various electrolyte concentrations.

$[Cu^{2+}]/[Ag^{+}]^2$	$[Ag^{+}]$ / M	$[Cu^{2+}]$ / M	ΔE_{ME} / V	ΔE_{RE} / V
10000	0.01	1	0.301	−0.313
1	1	1	0.427	−0.401
100	0.01	0.01	0.433	−0.420
0.01	1	0.01	0.524	−0.487

Table 2.2: Summary of ΔE_{ME} and ΔE_{ME} for Zn-Cu Galvanic cell. Measured values of ΔE_{ME} performed under open-circuit conditions and ΔE_{RE} performed under short-circuit conditions for the Zn-Cu galvanic cell for various electrolyte concentrations.

$[Zn^{2+}]/[Cu^{+2}]$	$[Cu^{2+}]$ / M	$[Zn^{2+}]$ / M	ΔE_{ME} / V	ΔE_{RE} / V
100	0.01	1	0.832	−0.852
1	0.01	0.01	0.860	−0.884
1	1	1	0.881	−0.893
0.01	1	0.01	0.971	−0.951

Given that the corrosion literature attributes the voltage difference of the SRET technique as a response to ionic current in solution, the Cu-Ag electrochemical cell was operated using a galvanostat (current source) to vary the current flow between the electrodes of the half-cells shown schematically in Figure 2.4a. In this case, ΔE_{RE} was measured as a function of current supplied between the metal electrodes taking the Ag half-cell and Cu half-cell to be the positive and negative leads, respectively. The source meter supplied current to the electrochemical cell with the Ag and Cu electrodes to be the positive and negative leads, respectively. Here, a negative current corresponds to electrons flowing from the Cu electrode to the Ag electrode (red arrow Figure 2.4a, Cu is oxidized and Ag is reduced) while a positive current indicates electrons are flowing from the Ag electrode to the Cu electrode (blue arrow Figure 2.4a, Ag is oxidized and Cu is reduced). The measured values of ΔE_{RE} as a function of applied current are shown in Figure 2.4b. Under open-circuit conditions (i = 0.0 mA), the nominal value of ΔE_{RE} was found to be 0 V. This observation is consistent with the idea that the voltage measured between the reference electrodes is due to ionic current flow. When the source meter was used to set $\Delta E_{\mathrm{ME}} = 0$ V, the measured current was found to be $i = -15.0$ mA and the voltage between the reference electrodes was $\Delta E_{\mathrm{RE}} = -0.412$ V. As the polarity of the current was reversed to $i = +15.0$ mA, the voltage differences measured between the reference electrodes was found to be $\Delta E_{\mathrm{RE}} = +0.418$ V.

The results of the ΔE_{RE} measurements under the electrolytic cell configuration provide several insights regarding the reference electrode technique. As mentioned, the measured voltage difference of $\Delta E_{\mathrm{RE}} = 0$ V when the current between metal electrodes was forced to i = 0.0 mA is consistent with the corrosion literature, which attributes the measured voltage due to the flow of ionic current within solution.[73,74] This is also supported by the observed magnitude of ΔE_{RE} remaining unchanged for a given pair of $\pm i$. Another important takeaway was that for negative currents ($i < 0.0$ mA), the electrochemical cell was acting as a galvanic cell. In each case where the reduction of Ag^+ was occurring at the Ag half-cell, sign of ΔE_{RE} was found to be negative. Conversely, for all $i > 0$ mA, oxidation was taking place at the Ag half-cell while reduction was occurring in the Cu half-cell. Under these conditions, the sign of ΔE_{RE} was found to be positive. Taken together, the experimental results suggest that the sign of the measurement can be used as an indicator for the type of reaction occurring (*i.e.* $\Delta E_{RE} < 0$ for reduction and $\Delta E_{RE} > 0$ V for oxidation).

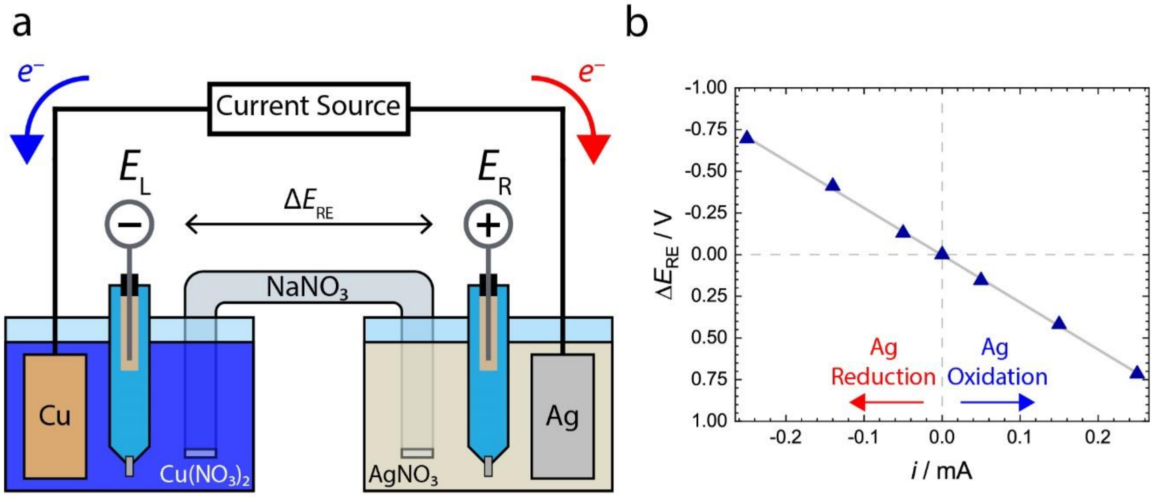

Figure 2.5. Measurement of ΔE_{RE} as a function of applied current in Cu-Ag electrochemical cell. (a) Schematic representation of how the ΔE_{RE} measurements were performed as a function of current applied between the electrodes in the Cu-Ag electrochemical cell. The electrolyte concentrations were 0.01 M for both $Cu(NO_3)_2$ and $AgNO_3$. Red and blue arrows indicate direction of negative and positive current flow, respectively. (b) The measured values of ΔE_{RE} as a function of current sourced between the Ag and Cu electrodes. Red and blue arrows indicate currents that correspond to Ag reduction and oxidation, respectively.

2.4.2 Plasma Conductivity Measurements

The conductivity a helium atmospheric pressure plasma jet was estimated using current-voltage measurements acquired using a double Langmuir probe (DLP). Approximating the Pt probe tips that are inserted into the plasma as parallel axis (paraxial) cylinders, the electric field can be found using Gauss' law[77]

$$\int \boldsymbol{E} \cdot d\boldsymbol{A} = \frac{Q_{enc}}{\varepsilon} \tag{2.15}$$

where $\boldsymbol{E}$ is the electric field vector, $\boldsymbol{A}$ is the area vector, Q_{enc} is the charge enclosed, and ε is the permittivity. The radial component of the electric field is given by

$$E_r = \frac{\lambda}{2\pi\varepsilon_0\varepsilon_r r} \tag{2.16}$$

where λ is the linear charge density, ε_0 is the permittivity of free space, ε_r is the relative permittivity, and r is the radial distance from the outer radius of the electrode r_0. Integrating Equation 2.16 with respect to the x-axis gives the interelectrode voltage, V

$$V = \frac{\lambda}{\pi\varepsilon_0\varepsilon_r} \ln\left(\frac{2a}{r_0} - 1\right) \tag{2.17}$$

where a is the interelectrode spacing between the platinum tips. The current density, $\boldsymbol{j}$, between electrodes is given by

$$\boldsymbol{j} = \sigma\boldsymbol{E}\,. \tag{2.18}$$

where σ is the plasma conductivity. The interelectrode current, i, is found by integrating the current density with respect to the area enclosed which gives

$$i = \frac{\sigma\lambda L}{\varepsilon_0\varepsilon_r} \tag{2.19}$$

where L is the length of the Pt electrodes. Rearranging the Equations 2.17 and 2.19 in terms of the linear charge density, and solving for conductivity gives

$$\sigma = \frac{i}{V\pi L}\ln\left(\frac{2a}{r_0}-1\right). \tag{2.20}$$

Using the experimental IV traces (Figure 2.6) obtained from the DLP for the helium plasma jet, the conductivity was found to be $\sigma \approx 780$ µS cm^{-1}. The conductivity in a weakly ionized plasma can be calculated using the expression[79]

$$\sigma = q_e \mu_{e,+} n_e \tag{2.21}$$

where q_e is the fundamental charge, $\mu_{e,+}$ is the electron mobility for a particular ionic species, and n_e is the electron density. In the case of a helium at atmospheric pressure, the mobility is given by $\mu_e = 0.1194$ m^2 V^{-1} s^{-1}.[80] Using an electron density of $n_e = 1\cdot10^{21}$ m^{-3} Equation 2.21 yields a plasma conductivity value of σ = 19,302 µS cm^{-1}.

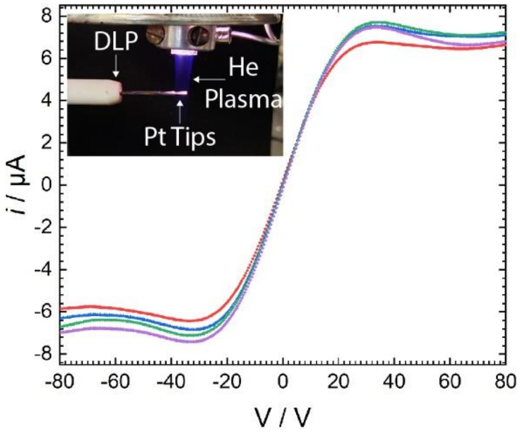

Figure 2.6. Double Langmuir Curve IV Traces. Characteristic IV traces obtained by DLP for atmospheric pressure helium plasma jet (shown in the inset image).

The conductivity values for the solutions will be investigated in the following few chapters vary over the range of 10^2 to 10^4 μS cm^{-1}. However, for the sake of the discussion, a solution with a nominal conductivity of σ = 300 μS cm^{-1} will be assumed. The estimates for the plasma conductivity obtained from the DLP measurements and the calculation are approximately greater than the solution conductivity by factors of 2.5 and 600, respectively. In this case, the relatively similar conductivity values suggest that the solution will not necessarily be the largest resistance to current flow in plasma-liquid systems. Here, the electrostatic potential drop cannot be assumed to only occur in the liquid; rather, a portion would be expected to drop in the plasma. Thus, the reference electrode measurement will only reflect the true difference in reduction potentials between two zones (*e.g.* the plasma-liquid interface and bulk solution) under certain circumstances.

2.5 Conclusions

In the case of electrochemical cells, the separate zones (*i.e.* half-cells) each have a particular reduction potential. When these half-cells are short-circuited, their electrons energies must equilibrate thereby initiating charge-transfer reactions. In response to this charge-transfer process, an electrostatic potential difference develops that is equal to the differences in the reduction potentials of the half-cells before contact. If one can assume that the electrolyte solution is the largest resistance to current flow, the electrostatic potential drop is expected to only occur within the liquid. Under these special circumstances, the reference electrode measurement will be representative of the differences in reduction potentials.

In the case of a galvanic cell, the differences in the reduction potential between the half-cells is given by the cell potential. For both the Cu-Ag and Zn-Cu galvanic cells examined, the cell potentials were directly determined in the ΔE_{ME} measurements. The similar magnitudes observed between the ΔE_{ME} and ΔE_{RE} measurements suggested that the reference electrode method was also a measurement of the difference in reduction potential between the half-cells, albeit opposite in sign. In other words, in the ideal scenario where the electrostatic potential drop only occurs in the solution, the upper-bound of the ΔE_{RE} measurement is equal in magnitude to the difference in reduction potential between the zones the reference electrodes are measuring.

In the case of the electrolytic cell experiments, the measurement of ΔE_{RE} as a function of current was consistent with reports attributing the measured voltage to (ionic) current. Here, the reference electrodes were measuring the local potential in the Ag half-cell with respect to the Cu half-cell. In the case of $i < 0.0$ mA, reduction was taking place in the Ag half-cell. The magnitude of ΔE_{RE} varied as i became more negative, but the sign of ΔE_{RE} was consistently negative. Conversely, oxidation was taking place in the Ag half-cell for all $i > 0.0$ mA, where the sign of ΔE_{RE} was found to be positive in all cases. Thus, the measured sign of ΔE_{RE} in the electrolytic and galvanic cell experiments suggest that the technique is able to indicate whether an oxidation or reduction half-reaction is taking place. More specifically, $\Delta E_{\mathrm{RE}} < 0$ V suggest that reduction is occurring, while $\Delta E_{\mathrm{RE}} > 0$ V indicate that oxidation is taking place.

For plasma-liquid systems, estimates for the conductivity of plasma and electrolyte solution were found to be on similar orders of magnitude. In this case, the assumption that the solution is largest resistance to current flow is not always applicable. In other words, it is reasonable to expect that a portion of the electrostatic potential drop will occur in the plasma. Consequently, the voltage difference measured between two zones in a plasma-liquid system (*e.g* the solution near plasma-liquid interface and bulk solution) will be less than, or equal to, the true difference in reduction potential. In solutions with relatively low conductivities, the measured

ΔE_{RE} will be more representative of the true difference in reduction potential. The relative magnitude of ΔE_{RE} can still provide insights regarding whether a reaction is thermodynamically favorable under a particular set of conditions or not. Additionally, the sign of the ΔE_{RE} measurement could also prove useful for determining regions in which reduction or oxidation are favored. This is particularly useful in the case of electrodeless systems, where the locations of redox reactions are not immediately obvious.

Chapter 3

Electrochemical Characterization of a Plasma-Liquid Interface

3.1 Introduction

Nonthermal plasmas operating at atmospheric pressure have been used for a variety of applications in the fields of medicine,[81–84] agriculture,[85,86] material processing,[32] and nanomaterial synthesis.[40,87,42] These applications typically utilize plasmas as a potent source of energetic species including radicals,[88] atomic and molecular ions, and high-energy photons[89] to initiate chemical reactions in aqueous media.[88–90] Atmospheric pressure plasmas using noble gases, such as helium and argon, have been shown to inject free electrons into aqueous media, wherein they become solvated and induce electrochemical reactions.[50,63] These electrochemical, or reduction-oxidation (redox) reactions occurring at the interface of plasmas in contact with liquids offer the capability of performing electrochemistry without solid electrodes. An electrodeless approach is hypothesized to circumvent the disadvantages of physical electrodes, such as susceptibility to fouling[11,10] and oxidation.[91] As such, plasma electrochemistry has attracted attention as a means of achieving novel electrochemistry. However, remarkably little is known about the electrochemical nature of the plasma-liquid interface, hindering the ability to rationally design redox reactions.

Redox reactions in conventional electrochemical systems are understood in terms of the reduction potential, which is the key parameter that describes the energy of electrons and their propensity to reduce chemical species. Typically, the reduction potential is controlled by applying a voltage to a working electrode comprised of a metal or semiconductor that is immersed in the liquid electrolyte. The working electrode is connected to a counter electrode via an external circuit (*e.g.* conducting wire, power supply, etc.), allowing current to flow between the two electrodes. The reduction potential is determined by measuring the voltage difference between the working electrode and a nearby reference electrode, which is an electrode with a well-defined chemical composition that forms a chemically stable interface with the unknown solution. The reference electrode senses the local reduction potential, and the voltage is affected by both the local electrostatic potential and chemical potential of different species. If the goal is to isolate the chemical potential contribution, then the measurement is performed under conditions where an assumption can be made that the electrostatic potential difference between the working and reference electrodes is negligible. In the case of a free plasma jet in contact with a liquid, the electrostatic potential in the plasma is significantly greater than in the reference electrode and the assumption is no longer valid. While some characterization of the reduction potential in plasma-liquid systems have been reported,[68,92] these measurements were performed offline and did not directly measure the effect that the plasma has on the reduction potential. Given that the redox reaction of interest is occurring in the liquid phase, the goal should be to characterize the reduction potential on the liquid side of the plasma-liquid interface. Rather than measuring the potential of the plasma itself, characterization of the potential directly beneath the liquid surface at the plasma interface would be more representative of the reduction environment controlling reactions in solution. The reduction potential of the plasma-liquid interface (PLI) is given the symbol E_{PLI}.

The measurement of E_{PLI} should be referenced to a potential at some position in the solution which is not immediately affected by the plasma-liquid interface, such as the potential in the bulk solution, E_{inf}. The value of E_{inf} is influenced by the relative concentrations of the oxidized and reduced forms of the species in solution, which can be expressed using the Nernst equation. Consider a simple electrochemical half-reaction of the form

$$O^{z} + ne^{-} \rightarrow R^{z-n} , \tag{3.1}$$

where O and R are the oxidized and reduced forms of the O^{z}/R^{z-1} redox couple, respectively. The Nernst equation can be expressed as[13]

$$E_{\mathrm{inf}} = E_0 + \frac{RT}{nF} \ln \frac{C_O^*}{C_R^*} , \tag{3.2}$$

where E_0 is the standard reduction potential of the redox couple, R is the ideal gas constant, T is the temperature, n is the number of electrons involved in the electron-transfer reaction, F is the Faraday constant, and $C_O{}^*$ and $C_R{}^*$ are the concentrations of the oxidized and reduced species in the bulk, respectively. For a single redox couple in solution, the difference between E_{PLI} and E_{inf} can be written using the same functional form as the overpotential used in electrochemistry as

$$\eta_{\mathrm{PLI}} = E_{\mathrm{PLI}} - E_{\mathrm{inf}} . \tag{3.3}$$

Recall from Chapter 2, the magnitude of η_{PLI} only provides an upper-bound for the reduction potential difference between the plasma-liquid interface and the bulk solution. Herein, η_{PLI} will be considered to be the relative reduction potential of the plasma-liquid interface, which can be used to determine the direction of the redox reaction. If it is negative, then the reaction proceeds from oxidized to reduced, and if it is positive, then the reaction proceeds from reduced to oxidized.

In this work, we present a method of electrochemically characterizing the relative reduction potential of plasmas in contact with solutions comprised of a single redox couple. The method relies upon measuring the difference in potential directly beneath the plasma-liquid interface relative to the potential in the bulk solution. Using redox indicators, which are compounds that undergo oxidation state-dependent color changes, colorimetric assays were performed to compare reduction kinetics to electrochemical measurements. Indigo carmine (IC) and methyl viologen (MV) were selected as model redox indicators for two reasons: (1) the use of a redox indicator defines the half-reaction in which the electrical measurements are referenced to (i.e. determines the value of E_{inf}) and (2) the different properties of the molecular probes allow us to provide alternative approaches for determining if the plasma is decomposing the organic molecular probe. The observed reaction of the redox indicators at extremely small values η_{PLI} suggest that the electrostatic potential is dropped in both the plasma and the liquid, as discussed in Chapter 2.

3.2 Experimental

3.2.1 Plasma Source

The plasma source used in all experiments was an atmospheric pressure plasma jet (APPJ), shown in Figure 3.1a. The plasma was generated using a 13.56 MHz RF power supply (AG 0613, T&C Power Conversion) connected to an impedance matching network (AIT-600 RF Auto Tuner, T&C Power Conversion). The powered electrode was an aluminum ring mounted on a fused silica tube with inner and outer diameters of 7 and 9.5 mm, respectively. An identical aluminum ring electrode was connected to ground and mounted at a lower position on the tube. The spacing between the electrodes was 9.5 mm. The plasma was generated using helium as the operating gas, flowing through the tube at a rate of 30.5 standard liters per minute. The flow rate was controlled by means of a critical flow orifice that was 300 μm in diameter. The APPJ apparatus was housed in a cylindrical aluminum enclosure with an outer diameter of 85 mm and a length of 140 mm to provide shielding against electromagnetic interference emitted from the plasma jet. All plasma

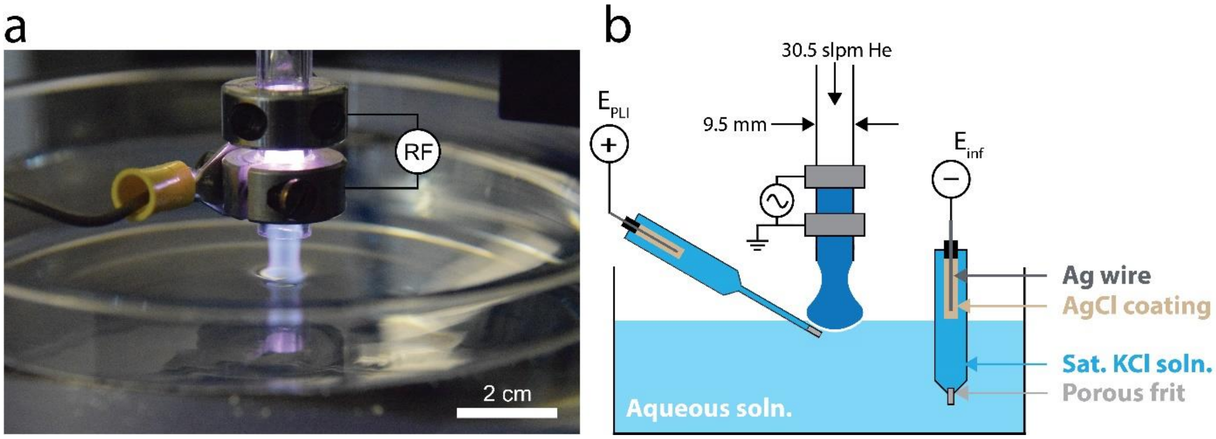

Figure 3.1. Experimental Apparatus. (a) Image of the APPJ in contact with an aqueous solution and (b) schematic representation of the experimental setup used to conduct the electrochemical measurements.

treatments were conducted under ambient conditions in air with a relative humidity in the range of 50-55%.

3.2.2 Electrochemical Characterization of Plasma-Liquid Interface

Electrochemical characterization of solutions was conducted using silver/silver chloride/saturated potassium chloride (Ag/AgCl/saturated KCl) reference electrodes (Ø = 3 mm) connected to a digital multimeter (DMM6500, Keithley) and an in-line low pass RF filter (Crystek Corporation). Note that the diameter was selected to avoid interruptions in the measurement due to the presence of ripples on the liquid surface. The perturbing effects can be suppressed by lowering the gas flow rate, if higher spatial resolution using smaller refence electrodes is desired. The reference electrodes were submerged in crystallization dishes containing 250 mL of freshly prepared redox indicator solution. The preparation of the redox indicator solutions is described below. The relative height of the crystallization dish was adjusted such that the liquid level was at a fixed distance of 15 mm from the ground electrode of the APPJ. The reference electrode measuring the potential of the bulk solution, E_{inf}, was positioned in the solution at a distance far away from the plasma jet. The reference electrode measuring the potential of the plasma-liquid interface, E_{PLI}, was placed directly underneath the plasma sheath region, as close to the surface as experimentally possible similar to the schematic in Figure 3.1b. The plasma was ignited for a duration of 30 seconds using a fixed RF power and immediately turned off for a 20 second period before re-igniting the plasma at a different applied RF power. The RF powers used in the experiments were 60, 100, 140, 180, and 220 W. The mean and standard deviation of the measured relative reduction potential at each RF power was determined using the data acquired during the duration the plasma was ignited.

3.2.3 Colorimetric Assays of Redox Indicators

Indigo carmine (IC) and methyl viologen (MV) are redox indicators, which are molecular probes that undergo color changes depending on the oxidation state of the molecule. IC exists in an oxidized keto form, IC^{2-}, and a reduced enol form, H_2IC^{2-}, with characteristic absorption peaks around 610 and 400 nm, respectively.[93] MV can exist as a dication (MV^{2+}), a radical cation (MV^{+}), and as a fully reduced molecule (MV^{0}) with each oxidation state having characteristic spectroscopic features. MV^{2+} has an absorption maximum at a wavelength of 257 nm, MV^{+} has two peaks at 400 and 600 nm, and MV^{0} has a maximum absorption at 390 nm.[94,95] IC and MV were purchased from MilliporeSigma and used as received. Fresh IC and MV stock solutions were prepared using deionized water (18.2 MΩ cm) prior to each experiment. The nominal initial concentrations of the IC and MV solutions were 25 μM and 2.5 mM, respectively. The pH of the stock solutions were adjusted to pH > 11 using sodium hydroxide purchased from Fisher Scientific. The pH was measured using pH probes (PHE-1478, Omega Engineering) before and after plasma treatments. Aliquots containing 70 mL of initially identical IC and MV were positioned such that the liquid level was at a distance of 15 mm from the ground electrode of the APPJ. The solutions were treated at different applied RF powers for 8 minute durations. The RF powers used in the experiments were 60, 100, 140, 180, and 220 W. Immediately after plasma exposure, 2 mL of the treated solution was transferred to a cuvette for ultraviolet–visible (UV-Vis) absorption spectroscopy. Treated solutions were compared to the untreated stock solution in order to determine the amount that had reacted. UV-Vis absorption spectra were measured on a Cary 50 Bio spectrophotometer (Varian) over the wavelength range of 300–700 nm.

3.2.4 Electrochemical Reduction

MV^0 standards are required to use liquid chromatography to analyze the products of reaction. Pure MV^0 standards are not commercially available. Thus, we prepared MV^0 standards using a conventional three-electrode technique. Electrochemical reduction was performed on MV^{2+} stock solutions with nominal concentrations of 2.5 mM and pH > 11 for product comparison. The electrochemical reduction was performed using a two-compartment electrochemical cell, in which the working and auxiliary electrodes were separated by a salt bridge containing 2% agar solution. The working electrode was gold foil with an area of 2 cm^2 with Ag/AgCl/saturated KCl and platinum wire acting as the reference and auxiliary electrodes, respectively. Chronoamperometry was used to apply a constant potential of −1.0 V vs SHE to the working electrode for a duration of 3 hours controlled using a potentiostat (SP-150, BioLogic). Following the electroreduction, 3 mL of solution was transferred for spectroscopic characterization.

3.2.5 Spectroscopic Characterization

MV samples were characterized spectroscopically to detect if any byproducts were formed during electrochemical reduction or plasma treatment processes. Two MV solutions were prepared for plasma treatment, each with a nominal concentration of 2.5 mM. One of the solutions was plasma-treated with an unadjusted pH of 7, while the other was treated with an adjusted pH > 11. Treatments were conducted for a duration of 8 minutes using an applied RF power of 220 W. Immediately after treatment, 3 mL of the treated solutions were transferred to cuvettes for spectroscopic characterization. The excitation wavelength to be used for the fluorescence emission spectroscopy was determined using the maximum absorbance wavelength of the MV solutions as measured by a spectrophotometer (UV-1800, Shimadzu) scanning over the range of 300–700 nm. The fluorescence emission spectra of the MV solutions for each preparation method was acquired on a spectrofluorometer (RF-6000, Shimadzu) using an excitation wavelength of 390 nm, scanning over the wavelength range of 400–750 nm.

3.2.6 Product Analysis

Products from electrochemically reduced and plasma-treated solutions were analyzed using High Performance Liquid Chromotography with UV detection (HPLC-UV, 1260 Infinity II, Agilent) which was equipped with an C18 column (3.0 mm × 150 mm, 3.5 μm, Eclipse Plus, Agilent). The aqueous phase was 10 mM boric acid (pH 9.5) and the organic phase was acetonitrile/water (95/5, v/v) with a flow rate of 0.5 mL/min and an injection volume of 50 μL. For gradient elution, the organic phase was held at 3.5% for 8 min, adjusted to 50% at 9 min and held till 12 minutes, then returned to 3.5% at 12.2 minutes. Absorbance was measured at 390 nm. Three product peaks were observed with retention times of 6.8, 8.9, and 11.0 minutes that had areas proportional to the concentration of MV^0 in solution.

3.2.7 Conductivity Measurements

Conductivity measurements were performed to determine if electrostatic shielding, by mobile ions in solution, influenced the electrochemical measurements. The conductivity of IC and MV solutions were determined with a conductivity meter (0162A1, Thermo Scientific Orion). An identical IC solution was prepared using the same procedure as in the colorimetric assays with an additional conductivity adjustment step. Sodium chloride (NaCl), purchased from MilliporeSigma, was used to adjust the conductivity of the IC solution such that it matched the conductivity of the MV solution. Electrochemical characterization and colorimetric assays of the IC + NaCl solution were performed using the same protocols outlined above.

3.2.8 Quantification of Reactive Oxygen and Nitrogen

Experiments were performed to determine the concentration of long-lived RONS were produced in indigo carmine (IC) and methyl viologen (MV) solutions after plasma-treatments. More specifically, the concentration of nitrite (NO_2^-), and nitrate (NO_3^-), and hydrogen peroxide (H_2O_2). All solutions were prepared using ultrapure (18.2 MΩ cm) water. IC and MV solutions were prepared with nominal concentrations of 25 μM and 2.5 mM, respectively. Sodium hydroxide was used to adjust the pH of the solutions to 11. Samples were plasma-treated in volumes of 70 mL at a standoff distance of 15 mm. Plasma treatments were conducted using a helium flow rate of 30.5 liters per minute at an applied RF power of 220 W for a total of 8 minutes. Standard solutions of NO_2^- and NO_3^- used for ion chromatography were prepared with nominal concentrations of 0.5, 1, 5, 10, 20, and 30 μM with sodium nitrite (>99.0%, MilliporeSigma) and sodium nitrate (>99.0%, MilliporeSigma), respectively. Standard solutions and plasma-treated redox indicator solutions were analyzed by a Dionex Integrion high performance ion chromatography (HPIC, Thermo Scientific) system with a suppressed conductivity detector. The suppressor current was set to 30 mA the temperature of the cell was held at 35 °C. A 12.0 mM solution of potassium hydroxide was used as the eluent at a constant flow rate of 1 mL min^{-1} through a Dionex IonPac AS11 anion exchange column (4 × 250 mm). The sample injection volumes were 25 μL for a total run time of 6 minutes. The linearity for the NO_2^- and NO_3^- used $r^2 = 0.9004$ and 0.9814, respectively.

Quantification of H_2O_2 in IC and MV solutions was determined via a colorimetric assay using the N,N-diethyl-p-phenylenediamine (DPD) method.[96] Briefly, a 40 mL solution of 6.10 mM DPD and 0.1 M sulfuric acid (H_2SO_4), 6.10 mM DPD was stored in an amber vial at 4 °C. Peroxidase (POD) solutions were freshly prepared and stored at 4 °C. The limit of detection of this method was 0.76 µM H_2O_2. The stock solution of H_2O_2 was diluted and standardized spectrophotometrically ($\varepsilon = 43.6\ M^{-1}\ cm^{-1}$ at 240 nm) daily and was used to establish a standard curve. To determine the concentration of H_2O_2 in untreated controls and plasma-treated solutions, 1 mL of 0.5 M phosphate buffer (pH = 6.0) was added to 9 mL of redox indicator solution, followed by 50 µL DPD and 50 µL POD in rapid succession. After 2 minutes, the solution was transferred into a cuvette and the absorbance at 551 nm was obtained using a UV-Vis spectrophotometer (Varian Cary 50 Bio UV-Visible Spectrophotometer).

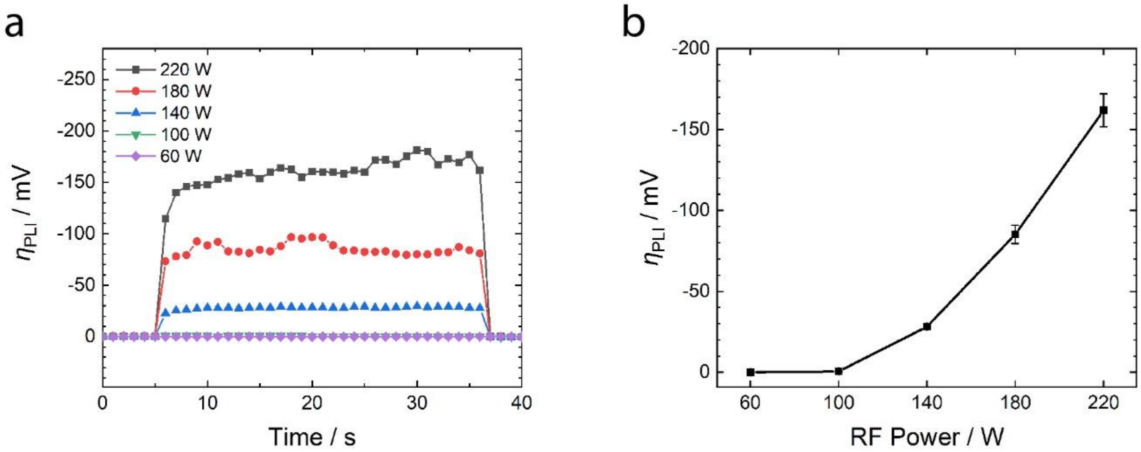

Figure 3.2. Negative Relative Reduction Potential at the Plasma-Liquid Interface. (a) Measured relative reduction potential at the plasma-liquid (η_{PLI}) in a redox indicator (indigo carmine) solution as a function of time at various applied RF powers. (b) The average relative reduction potential, $\bar{\eta}_{PLI}$, as a function of applied RF power. The averages were determined from the data in (a) and the error bars are the standard deviations. Note that the potential differences are reported using the American convention where more negative (reducing) potentials are plotted above the origin.

3.2.9 Mass Transport Effects

Experiments were performed to determine if the apparent leveling off of the reaction rate was due to mass transport limitations. Stock solutions of indigo carmine (IC) were prepared with ultrapure deionized water (18.2 MΩ cm) to have a nominal concentration of 25 µM and a pH > 11. 70 mL aliquots were transferred to glass petri dishes for treatment. The petri dishes were adjusted such that the height of the liquid level was at a distance of 15 cm from the ground electrode of the APPJ. Two sets of initially identical IC solutions were plasma treated for 8 minute durations using RF powers of 60, 100, 140, 180, and 220 W. One of the IC solution sets was stirred using a magnetic stir bar during the treatments, while the other solution remained stagnant. Immediately after treatment, 2 mL aliquots were drawn for UV–Vis absorption spectroscopy to determine the reaction rates relative to an untreated solution.

3.3 Results & Discussion

Electrochemical characterization of the plasma-liquid interface in solutions containing redox indicators revealed that the relative reduction potential, η_{PLI}, immediately become negative when the plasma was ignited and returned to the baseline value of zero as soon as the plasma was turned off (Figure 3.2a). As the applied RF power was increased, the average relative reduction potential, $\bar{\eta}_{\mathrm{PLI}}$, became increasingly negative as shown in Figure 3.2b. At lower powers, $\bar{\eta}_{\mathrm{PLI}}$ was only slightly more negative than the baseline. These results suggest that the plasma-liquid interface is a net reducing environment and that the redox indicators should undergo reduction. The model redox indicators used in all of the reported experiments were either indigo carmine (IC) or methyl viologen (MV).

The reduction of IC involves a two electron, two proton transfer and thus the standard reduction potential of IC is dependent on pH. The stability of IC solutions in contact with plasmas is unknown, therefore a method to verify no side reactions are occurring is necessary. While electrochemical characterization methods such as cyclic voltammetry can be used to verify that redox indicators are not destroyed by exposure to plasmas, simpler methods based on spectroscopic properties are more straightforward. One such method is the use of isosbestic points, which are wavelengths where the molar extinction coefficients, ε, of a reactant species X and a product species Y are equal (i.e. $\varepsilon = \varepsilon_X = \varepsilon_Y$). For an elementary reaction of the form:

$$X \rightarrow Y, \tag{3.4}$$

the system initially only contains X which has a concentration of $[X]_0$. The concentration of X at any point in the reaction can be written in terms of the extent of reaction, ξ, as:

$$[X] = [X]_0 - \xi. \tag{3.5}$$

If there are no intermediate species or degradation products, then only X and Y are involved in the reaction and the extent of reaction ξ would be equal to the concentration of species Y at any time:

$$\xi = [Y]. \tag{3.6}$$

Substituting this into the previous expression and rearranging yields:

$$[X]_0 = [X] + [Y], \tag{3.7}$$

and therefore the absorbance A at an isosbestic point can be expressed as:

$$A = \varepsilon \cdot [X]_0 \cdot \ell, \tag{3.8}$$

which is invariant of the extent of reaction for a stoichiometric reaction. Thus, the direct reduction of IC^{2-} to H_2IC^{2-} can be verified by the presence of isosbestic points in the absorption spectrum.

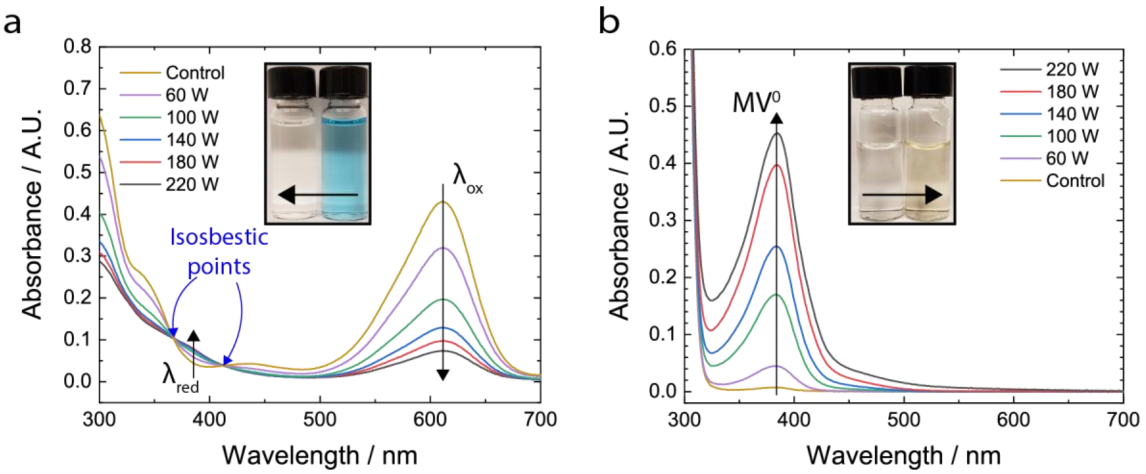

Figure 3.3. Absorption spectra of redox indicator solutions. (a) UV–Vis absorption spectra for IC solutions treated at various applied RF powers. Blue arrows indicate the isosbestic points. (b) UV–Vis absorption spectra for MV solutions treated at various applied RF powers at a pH of 11. Black arrows point from oxidized state to reduced state.

Initially identical IC solutions were blue in color, which faded after exposure to the plasma. In the most extreme case, the pH of the treated solution decreased by 0.2 but was still greater than 11. The absorption spectra of initially identical IC solutions that were plasma treated at different RF powers are shown in Figure 3.3a. Compared to the untreated control, the absorbance value at λ_{ox}, the wavelength corresponding to the oxidized form of IC, decreased with increasing power. Simultaneously, the absorbance at λ_{red}, the wavelength corresponding to the reduced form of the molecule, showed a gradual increase with increasing power. The observation of two crisp isosbestic points in the absorption spectra, as indicated by the blue arrows, suggest that both IC^{2-} and H_2IC^{2-} were stable in water after exposure to plasma.

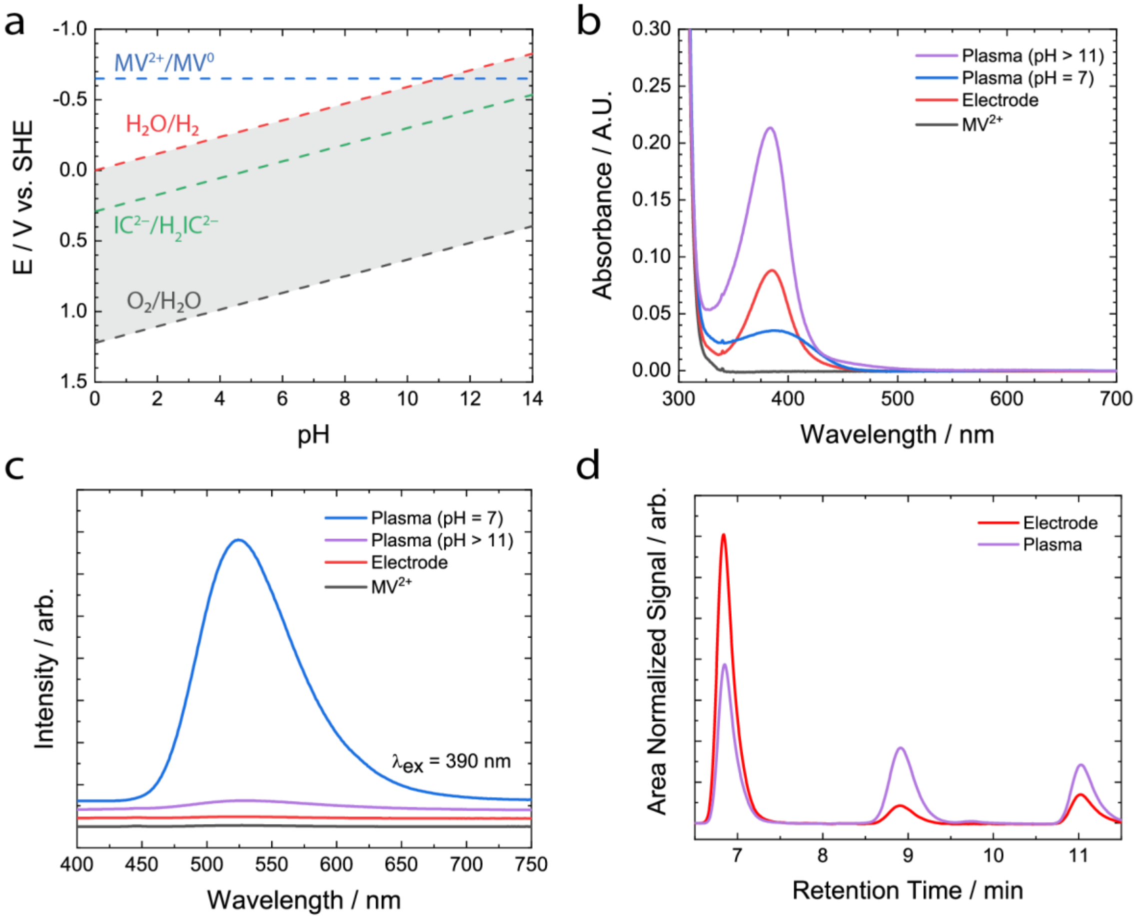

Figure 3.4. Stability of MV in water. (a) Pourbaix diagram depicting pH values at which IC and MV are stable in water (shaded area). Note that the diagram is constructed using the American convention where more negative potentials plotted above 0.0 V vs. SHE. (b) Absorption spectra for an untreated MV^{2+}, a solution electrochemically reduced at pH > 11, a solution plasma treated at pH > 11, and a solution plasma treated at pH 7. (c) Fluorescence emission spectra for the same solution preparations in panel (b) using an excitation wavelength of 390 nm. The spectra in (c) have been offset for clarity. (d) HPLC chromatograms acquired for electrochemically and plasma reduced solutions at pH > 11. The peak areas have been normalized such that the total area of the peaks the two sample preparations are equal.

MV has pH-independent standard reduction potentials of $E_{MV2+/MV+} = -0.45$ V and $E_{MV+/MV0} = -0.88$ V vs. SHE.[97,98] Unlike IC, isosbestic points cannot be applied to MV absorption spectra due to comproportionation reactions that occurs between the MV^{2+} and MV^0.[99–101] While the reduction potentials of MV redox couples are pH-independent, the amine group of MV^0 can become protonated in protic solvents, such as water.[102,103] Thus, the stability of MV^0 in water has a strong dependency on the pH of the solution particularly at low pH. Using a Pourbaix diagram to predict the stability of the MV^{2+}/MV^0 redox couple in water, it is only found to be stable under alkaline conditions, or more specifically pH values greater than or equal to 11 (Figure 3.4a). Oxidation side reactions of MV result in the addition of ketone substituents in one of the pyridine rings, resulting in 2-pyridone ('2-one') or 3-pyridone ('3-one'), both of which share similar spectroscopic features as MV^0. The net effect of the ketone substituents on the absorption spectrum is the broadening of the peak at 390 nm. The presence of the ketone-derivatives can be determined using fluorescence spectroscopy. The three oxidation states of MV do not fluoresce, whereas the '2-one' and '3-one' byproducts are strongly fluorescent.[95]

Experiments were performed to demonstrate that the plasma treatments successfully reduced MV^{2+} to MV^0 in aqueous solutions with pH > 11. Herein, solutions with a pH > 11 and pH 7 will be referred to as alkaline and neutral conditions, respectively. Spectroscopic characterization was conducted on MV solutions that were reduced using 3 different methods: (i) electrochemical reduction under alkaline conditions, (ii) plasma reduction under alkaline conditions, and (iii) plasma reduction under neutral conditions. Absorption spectroscopy revealed that all of the reduction methods exhibited the characteristic absorption peak of MV^0 centered around 390 nm (Figure 3.4b). However, the solution that was plasma treated at neutral conditions showed significant peak broadening. The untreated control and electrochemically reduced solutions exhibited no detectable fluorescence. A slight, almost negligible fluorescence was observed from the solution plasma treated under alkaline conditions. However, significant fluorescence was observed for the plasma-treated solution under neutral conditions (Figure 3.4c), suggesting the presence of ketone substituents amongst the products formed from the reaction at pH 7. The observation of green fluorescence suggests that 3-one is the predominant ketone formed in these reactions.[95] HPLC-UV revealed that the electrochemical and plasma reduction of solutions under alkaline conditions produced chemical species with the same retention times, as shown in the chromatograms in Figure 3.4d. The observation of multiple peaks is presumed to be due to the formation of MV^0 dimers and trimers, due to the reduction of comproportionation products or association reactions between MV^0 molecules.[100,104] The key finding is that the reduction of MV^{2+} solutions using plasma treatment and conventionally used solid electrodes produce the same products with a different distribution in the relative amounts. In addition to determining the stability of both IC and MV after plasma exposure, their interaction with reactive species present in solution was also considered.

Nonthermal plasmas in contact with aqueous solutions are known to generate long-lived reactive oxygen and nitrogen species (RONS),[67] for example hydrogen peroxide (H_2O_2), nitrite (NO_2^-), and nitrate (NO_3^-), which are all oxidants. The concentrations of these RONS were determined via a colorimetric assay[96] and ion chromatography and are summarized in Table 3.1. The concentration of NO^{3-} was less than 0.5 μM in both the plasma-treated IC and MV solutions. The only long-lived species detected in the case of IC was NO_2^-, which had a concentration that was slightly greater than the redox indicator itself. Despite the presence of excess NO_2^-, the observed net reduction of IC^{2-} caused by the plasma-liquid interface demonstrates that NO_2^- does not result in complete re-oxidation of H_2IC^{2-} at these concentrations. While the concentration of NO_2^- was not able to be determined in the case of MV, NO_2^- is known to react with MV^0 to form MV^+.[105] However, in our experiments, we observed no spectroscopic evidence of the characteristic ~600 nm absorption peak of MV^+.[95] Thus, we do not expect oxidation of MV^0 by NO_2^- after plasma-treatment to be important in these experiments. The reaction of MV^{2+} and H_2O_2 is known to irreversibly form the fluorescent ‘2-one’ byproduct,[106] which may have been responsible for the slight observed fluorescence in Figure 3.4c for samples that were plasma-treated. Knowing the conditions that IC and MV remain stable in solution, and having considered their net reactivity with RONS, the kinetics of the redox indicator solutions reduced by plasma exposure were studied.

Table 3.1: Summary of Reactive Oxygen and Nitrogen Species (RONS) Quantification. The concentrations of nitrite (NO_2^-), nitrate (NO_3^-), and hydrogen peroxide (H_2O_2) measured in IC and MV solutions immediately after plasma-treatment at an RF power of 220 W.

Sample	$[NO_2^-]$ / μM	$[NO_3^-]$ / μM	$[H_2O_2]$ / μM
IC	27.93	< 0.5	< 0.76
MV	---	< 0.5	~ 10

Colorimetric assays were performed on MV solutions to determine the effect that plasma power had on reduction kinetics. Initially identical solutions were clear and gradually developed color as they became reduced by the plasma. The pH changed by a negligible amount as a result of the reaction, decreasing by only 0.3 in the most extreme case. As shown in Figure 3.3b, the measured absorbance of the reduction peak corresponding to MV^0 increased with increasing applied RF power. It is noted that although the HPLC chromatograms revealed that additional species were present, which were presumed to be MV^0 dimers and trimers, the measured absorbance was taken to be only from the MV^0 monomer. Given that the kinetics of electrochemical reactions are typically described in terms of the overpotential, we will now compare the reaction rates determined by colorimetric assays to the electrochemical measurements of η_{PLI} at the same conditions, treating it as an effective overpotential.

The sign of η_{PLI} determines the nature of the electron transfer reaction at the plasma-liquid interface (i.e. oxidization or reduction). When the interface is a reducing environment, $\eta_{\text{plasma}} < 0$, and the concentration ratio of the reduced and oxidized forms, C_R/C_O, will be largest immediately underneath the plasma, even as the concentration of the reduced species in the bulk, C_R^*, increases with time. Conversely, when the interface is an oxidizing environment, $\eta_{\text{PLI}} > 0$, and C_R/C_O will be smallest in the vicinity of the plasma, regardless of how concentration of oxidized species in the bulk, C_O^*, changes with time. Classical electrochemical theories for electrode kinetics, such as the Butler-Volmer model, predict a reduction reaction rate, r_R, of the form:

$$r_R \propto \exp\left(-\frac{\alpha F}{RT}\eta\right), \tag{3.9}$$

where α is the transfer coefficient, which ranges from $0 \le \alpha \le 1$.[13] The transfer coefficient describes the fraction of the applied overpotential that enhances the rate of reaction. When $\alpha = 0$, the reaction rate is independent of the overpotential and thus the electrode is poorly suited for the electroreduction of that redox couple.

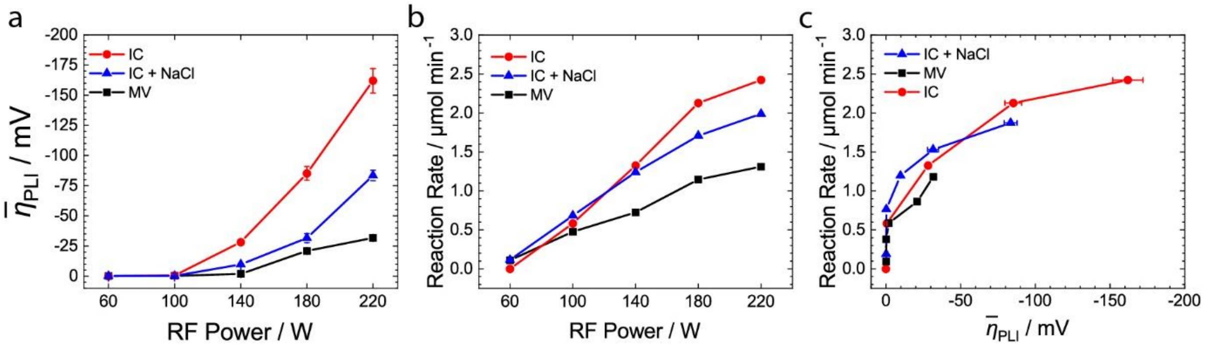

Figure 3.5. **Effect of Applied RF Power on Electrochemical Parameters.** (a) Average relative reduction potential ($\bar{\eta}_{\text{PLI}}$) as a function of applied RF power, (b) reaction rate as a function of applied RF power, and (c) reaction rate as a function of $\bar{\eta}_{\text{PLI}}$ for IC, IC + NaCl, and MV solutions. Note that the relative reduction potential are plotted using the American convention with more negative (reducing) potentials plotted above 0 mV.

The average relative reduction potential of the plasma-liquid interface was determined as a function of applied RF power using electrochemical measurements made in the redox indicator solutions (Figure 3.5a). The average relative reduction potential became more negative as the RF power was increased. With no apparent asymptote, the magnitude of $\bar{\eta}_{\text{PLI}}$ for a given solution appears to be limited by the RF power that can be supplied to the plasma. Given the disparity in the measured $\bar{\eta}_{\mathrm{PLI}}$ values between IC and MV, the effects of electrostatic screening were investigated. Ionic concentration, and conductivity by extension, determine the Debye length of the solution. A difference in ionic conductivity will result in different electrostatic screening lengths experienced by the reference electrode in a given solution. The measured conductivity of MV solutions had nominal values of 790 μS cm^{-1}, while IC solutions had nominal conductivities of 310 μS cm^{-1}. An additional IC + NaCl solution with a nominal conductivity of 790 μS cm^{-1} was prepared for comparison. The IC + NaCl was characterized electrochemically and a colorimetric assay was performed to determine the reduction kinetics. Interestingly, $\bar{\eta}_{\mathrm{PLI}}$ of the IC + NaCl solution was between IC and MV for each RF power, suggesting that the disparity between MV and IC arises due to a combination of electrostatics and chemical composition. The reaction rates, determined from the UV-Vis absorption spectra, are plotted as a function of applied RF power for the three solutions as shown in Figure 3.5b. An increase in reaction rate with increased RF power was observed for all three solutions. To determine if there was a correlation between the reaction rate and $\bar{\eta}_{\mathrm{PLI}}$, the two data sets were combined and presented in Figure 3.5c. For the three solutions, the reduction reaction rate increased as $\bar{\eta}_{\mathrm{PLI}}$ become more negative. While $\bar{\eta}_{\mathrm{PLI}}$ clearly had an effect on the reaction rate in the solutions (i.e. $\alpha \neq 0$), the reaction rate did not appear to follow the same exponential relationship as in the case of metal electrodes.

Interestingly, reduction occurred for all of redox indicator solutions, even in the cases where $\bar{\eta}_{\mathrm{PLI}}$ was approximately zero. This result suggests that the barrier to the reaction is extremely small and that plasmas are excellent electrocatalysts for these reactions. The apparent leveling off of the IC reduction rates at more negative $\bar{\eta}_{\mathrm{PLI}}$ are indicative of mass transport limitations. An additional experiment was conducted to determine if the reactions were limited by bulk transport.

As shown in Figure 3.6, the reduction rate at more negative $\bar{\eta}_{\mathrm{PLI}}$ does not appear to be limited by bulk transport. Another possible explanation for this behavior is that transport limitations are localized at the interfacial region rather than the bulk. The underlying reason for the observed phenomena requires further study.

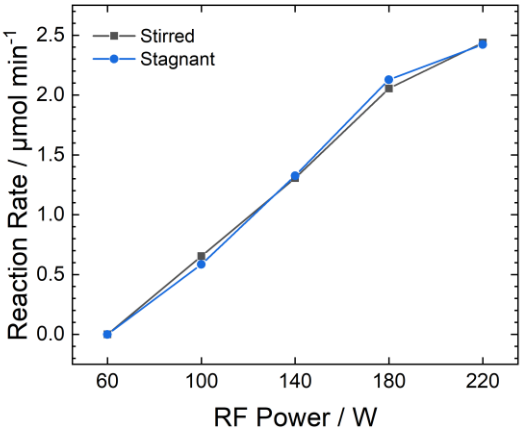

Figure 3.6 Effect of Stirring on Reaction Rate. Reaction rate as a function of applied RF power for IC solutions that were stirred (black) and solutions that were not mixed (blue) during plasma treatment.

3.4 Conclusions

Electrochemical measurements of the relative reduction potential in redox indicator solutions revealed that inert atmospheric plasmas have the capability to make a net reducing environment in solutions with reduction potentials more negative than the hydrogen evolution reaction. As the applied RF power of the plasma was increased, an increase in reaction rate was observed. Similarly, the measured reduction potential became more negative with increasing RF power. The observed reaction of the redox indicators at extremely small values η_{PLI} suggest that the electrostatic potential is dropped in both the plasma and the liquid, indicating that the η_{PLI} could be a lower estimate of the true reduction potential at these RF powers.

Chapter 4

Electrochemical Structure of a Plasma-Liquid Interface

4.1 Introduction

Interactions between atmospheric plasma and liquid media have attracted attention due to their great potential in the fields of medicine,[107–109] nanomaterial synthesis,[110–112] and wastewater treatment.[113–115] These applications utilize nonthermal plasma as a source of highly reactive species including radicals, photons, atomic and molecular ions, and electrons which can be transported into the plasma-liquid interface (PLI). The injection of energetic species at the PLI has been used to drive electrochemical reactions, such as carbon dioxide reduction,[59] ammonia synthesis,[116,117] and the hydrogen evolution reaction.[118,119] Reduction-oxidation (redox) chemistry in plasma-liquid systems has also been demonstrated in the context of plasma-activated water, which specifically studies the aqueous chemistry induced by reactive oxygen and nitrogen species (RONS).[120,121] However, to date, a comprehensive framework for understanding how to control the reactions occurring on the liquid side of the PLI has not been clearly elucidated, which frustrates efforts to achieve desired chemical transformations. We have recently proposed that the framework of electrochemistry can be used to conceptualize the liquid side of the plasma-liquid system,[122] wherein solid electrodes are now electrodeless near the PLI. However, the spatial locations of the electrodeless cathode and anode within the liquid have not been previously reported, thus the idea itself must be tested, which is the purpose of this work.

Electrochemical reactions are understood in terms of intrinsically coupled reduction and oxidation half-reactions, which describe the overall charge-transfer processes of the redox reaction in the liquid. The basic idea is that reduction half-reactions are coupled to oxidation half-reactions to preserve both the charge and atom balance in solution. In conventional electrochemical systems, the half-reactions simultaneously occur at interfaces of the working and counter-electrodes. In plasma-assisted electrochemistry configurations, which are systems wherein the working electrode is replaced by a DC microplasma, the half-reactions take place at the counter-electrode and the PLI.[123] Electrolytic systems capable of initiating redox reactions using reactive species without requiring electrical contact with a counter-electrode have been described as a form of electrodeless electrochemical systems.[124–126] One such example of an electrodeless system is a free atmospheric pressure plasma jets (APPJs) impinging upon liquid solutions (Figure 4.1), the absence of solid electrodes obfuscates the locations of the half-reactions (i.e. the locations of the electrodeless cathode and anode). Consequently, there is a lack in understanding of where the half-reactions occur in electrodeless plasma-liquid electrochemical systems. In the previous chapter, we developed a framework for electrochemically characterizing a free APPJ in contact with an electrolyte solution. The technique was based on using a reference electrode to measure the local potential within the liquid directly underneath the electrochemically active PLI, E_{rz}, and referencing that measurement to the potential of a nominally identical reference electrode positioned far away in the bulk solution, E_{inf}. The relative reduction potential measured between the reference electrodes within the solution is given by

$$\eta_{\text{rz}} = E_{\text{rz}} - E_{\text{inf}} \tag{4.1}$$

A negative potential was observed, suggesting that the reduction-half reaction (i.e. electrodeless cathode) was taking place directly underneath the PLI. Thus, the complementary oxidation half-reaction (i.e. electrodeless anode) is expected to be occurring elsewhere in solution.

In this chapter, we investigate the spatial electrochemical behavior of aqueous solutions exposed to a nonthermal radiofrequency (RF) helium APPJ to elucidate the locations of the redox half-reactions. Electrochemical characterization was based on a previously developed technique, which was adapted to perform measurements as a function of radial distance from the APPJ centerline and depth below the PLI.[122] Based on the signs of the potentials measured by the spatial electrochemical profiles, two distinct regions were observed: a negative region directly underneath the PLI with a positive region in the immediately surrounding solution. *In situ* multispectral imaging experiments were conducted using colorimetric probe molecules to independently determine where the electrochemical half-reactions taking place. Visualization of the spatial distribution of redox products was achieved by using white light illumination in conjunction with a scientific camera equipped with a bandpass filter. Reduction of the molecular indicator was only detected underneath the APPJ centerline, while the formation of oxidation products was found to occur at larger lateral distances. A surprising finding of our work, which has not previously been discussed in the existing plasma-liquid literature, is that the plasma-liquid interface simultaneously acts as both the cathode and anode which occur in spatially distinct locations within the solution.

4.2 Experimental

4.2.1 Materials

Indigo carmine (IC, 85%), titanium (IV) oxysulfate ($TiOSO_4$) solution (1.9-2.1%), potassium ferricyanide (~99%), and potassium ferrocyanide (≥98.5%) were purchased from MilliporeSigma. Sodium hydroxide (NaOH, 85%) was purchased from Fisher Scientific. Hydrogen peroxide (H_2O_2, 35 wt%) was purchased from Acros Organics. All chemicals were used as received without further purification. All solutions were prepared using Type III ultrapure (18.2 MΩ cm) water from a Direct-Q 3 Water Purification System (MilliporeSigma).

4.2.2 Plasma System

The plasma source used in this work was an APPJ generated using helium (He) as the operating gas, as shown in Figure 4.1. The He flow rate was maintained at a constant value of 2000 standard cubic centimeters per minute (sccm) using a mass flow controller (GE50A, MKS Instruments). The plasma was generated using a RF power supply (AG 0613, T&C Power Conversion) connected to an impedance matching network (AIT-600 RF Auto Tuner, T&C Power Conversion). An RF setpoint power of 40 W was used in all experiments. The APPJ was comprised of a powered nickel needle electrode with an outer diameter of 2.34 mm housed within a fused silica tube with inner and outer diameters of 7 and 9.5 mm, respectively. The ground electrode was an aluminum ring with an inner diameter of 9.5 mm, which was mounted to the exterior of the silica tube 5 mm from the tube outlet. The APPJ was attached to a micrometer positioning stage in order to maintain a gap height of 5 mm between the end of the silica tube and the surface of the solution undergoing treatment.

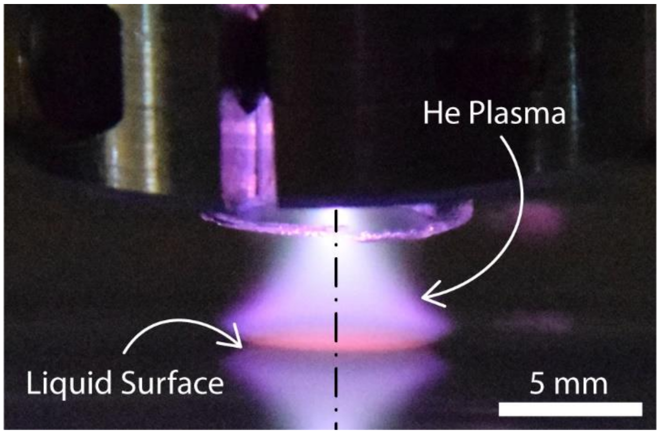

Figure 4.1. Atmospheric Pressure Plasma Jet. Image of helium atmospheric pressure plasma jet (APPJ) in contact with solution used in this work. Dotted dash line added to indicate the APPJ centerline.

4.2.3 Spatial Electrochemical Measurements

Spatial electrochemical measurements were performed within the liquid using the experimental apparatus shown in Figures 4.2a-b, which is an adaptation from the configuration used in Chapter 3. Here, the reference electrode used to measure the local potential in solution near the PLI (E_{rz}) was sealed in a Luggin capillary (Adams & Chittenden) which was mounted on a motorized two-axis stage (X-XY-LSM100A, Zaber Technologies) and controlled using LabView (National Instruments). The glass frit at the end of the Luggin capillary had an outer diameter (OD) of 3.0 mm. The reference electrode measuring the potential in the bulk solution (E_{inf}) remained fixed at a position far from the PLI. The reference electrodes were connected to a digital multimeter (DMM6500, Keithley) and the relative potential differences, η_{rz}, were recorded via LabView. Axial symmetry was assumed for the electrochemical measurements, which were conducted in a 740 mL crystallizing dish containing freshly prepared IC solution with a nominal concentration of 25 μM. The pH of the IC solution was adjusted to 11 using NaOH and verified using a pH probe (PHE-1478, Omega Engineering). For a fixed depth below the PLI, radial electrochemical measurements were performed by positioning the Luggin capillary directly underneath the centerline of the APPJ and using the motorized stage to move radially outward in 0.5 mm increments. In order to obtain a depth profile, the radial measurements were acquired at various depths below the PLI in increments of 0.25 mm. The potential difference near the PLI and bulk solution was measured for a duration of 45 seconds for each radial distance from the APPJ centerline and depth below the PLI. The potential differences at each position are reported as time-averaged values, $\bar{\eta}_{\mathrm{rz}}$.

4.2.4 Ultraviolet-Visible Absorption Spectroscopy

Ultraviolet-Visible (UV-Vis) absorption spectroscopy was used to verify the characteristic wavelengths of the molecular probes, which were used as the central wavelengths for the bandpass filters in the *in situ* multispectral imaging experiments. All UV-Vis absorption spectroscopy was conducted on a Cary 5000 (Varian) using a scan rate of 150 nm/min over the range of 350 to 700 nm. Solutions containing molecular probes were treated in glass petri dishes with an OD = 50 mm and height (*h*) of 15 mm. A freshly prepared IC solution with a nominal concentration of 50 µM and an adjusted pH of 11 was used to verify the characteristic wavelengths for both the reduction of IC^{2-} and formation of H_2O_2. For the reduction of IC^{2-}, sample volumes of 20 mL were taken from the same 50 µM IC stock solution and plasma treated for durations of 2, 4, and 6 minutes. Changes in pH measured before and after treatment were found to decrease only by 0.2 pH units. A separate untreated control (i.e. 0 minute plasma treatment) was set aside for comparison. Aliquots of 2 mL were taken from each petri dish immediately after plasma treatment and characterized using UV-Vis absorption spectroscopy. The titanium sulfate method was used to monitor the formation of H_2O_2 via the complex that forms between titanium sulfate, which has a strong absorbance centered around 408 nm.[127] Sample volumes of 20 mL from the same 50 µM IC stock solution were plasma treated for 2, 4, 6, 8, and 10 minutes. To verify the observed change in absorbance at 408 nm was due to H_2O_2 formation rather than interference from reduced H_2IC^{2-}, differences in the 408 nm absorbance between plasma treated IC solutions with and without the addition of $TiOSO_4$ were compared. Two aliquots were drawn for a given treatment time: 200 µL of $TiOSO_4$ was added to the first aliquot to quantify the amount of H_2O_2 formed, while 200 µL of ultrapure water was added to the second aliquot to maintain the same dilution factor. Standards with concentrations of 0 and 50 µM H_2O_2 were also prepared using the same 50 µM IC stock solution for comparison. Additionally, standards of the oxidized form IC^{2-} were prepared with a nominal pH of 11 to determine the concentration of IC after plasma-treatment. UV-Vis absorption spectroscopy was used to obtain the absorbance values of the characteristic 610 nm peak as a function of IC^{2-} concentration over the range of 5 to 100 µM and used to generate a calibration curve.

4.2.5 Multispectral Imaging

In situ multispectral imaging was used to visualize the spatial distribution of redox products in solution as a result of plasma treatment. The multispectral imaging experiments were performed using an LED light source as a white light illumination source, which was passed through a rectangular macro quartz cuvette (102.5 mm × 12.5 mm × 45 mm, FireflySci., Inc.). The macro cuvette was filled with a total volume of 45 mL of solution prior to each experiment and positioned underneath the APPJ centerline. A freshly prepared 50 µM IC solution for visualizing both IC^{2-} reduction and H_2O_2 formation. The cuvette was filled with 45 mL of the stock solution for the monitoring the reduction of IC^{2-}, while a mixture of 1 mL $TiOSO_4$ and 44 mL of the stock solution was used to detect the formation of H_2O_2. Images were acquired with a CMOS camera (Atlas 5.0 MP Mono, Sony Pregius IMX250 CMOS, LUCID Vision Labs) which was controlled using the ArenaView (LUCID Vision Labs) software package. All images were acquired using a frame rate of 10 frames per second, a pixel format of 16 bits per pixel, and a pixel resolution of 2448 × 2048. The reduction of IC^{2-} was imaged using a 600 nm bandpass filter (65-163, Edmund Optics) with a full width-half max (FWHM) of 10 nm with an exposure time of 8000 μs. The formation of H_2O_2 was imaged using a 400 nm bandpass filter (65-132, Edmund Optics) with a FHWM of 10 nm using an exposure time of 6000 μs.

4.2.6 Multispectral Imaging Processing

The raw images acquired in the multispectral imaging experiments were imported into MATLAB for post-processing. Each image frame was converted into a two-dimensional (2D) matrix containing the spatial pixel intensity, $I_t(x,z)$, at time t after plasma ignition. More specifically, the 2D matrices stored the pixel intensities, $I_{t0}(x,z)$, as function of spatial position (i.e. lateral distance from the APPJ centerline, x, and depth below PLI, z, for a particular time t after igniting the plasma. An initial frame acquired prior to igniting the plasma was used as a reference to track changes in the spatial pixel intensity resulting from plasma treatment. The change in absorbance for a given spatial position (x,z) was calculated using:

$$A_t\left(x,z\right)-A_{t_0}\left(x,z\right)=\log_{10}\left[\left(\frac{I_0}{I_t\left(x,z\right)}\right)\right]-\log_{10}\left[\left(\frac{I_0}{I_{t_0}\left(x,z\right)}\right)\right]=\log_{10}\left[\frac{I_{t_0}\left(x,z\right)}{I_t\left(x,z\right)}\right] \quad (4.2)$$

where $A_t(x,z)$ is the absorbance at time t after igniting the plasma, and $A_{t0}(x,z)$ is the absorbance of the reference frame, $I_t(x,z)$ is the pixel intensity at time t after igniting the plasma, and $I_{t0}(x,z)$ is the pixel intensity of the reference frame. Since all calculations were based on the pixel intensity for the same (x,z) coordinates between frames, the notation for the change in absorbance was simplified to $A_t - A_{t0}$. Images were cropped to show the region of interest and false-colored to generate the still images depicting $A_t - A_{t0}$. To account for the dispersion of the products in the vertical direction, the change in absorbance at a given lateral position was averaged over the depth, z. More specifically, changes in absorbance at a given lateral position were summed over a total depth of 2.0 mm and divided by the total number of pixels, n, used to perform the summation. The average change in absorbance is given by

$$\bar{A}_t - \bar{A}_{t=0} = \frac{\sum \left(A_t - A_{t0} \right)_z}{n} \tag{4.3}$$

where $\bar{A}_\mathrm{t} - \bar{A}_\mathrm{t=0}$ is the average change in absorbance at time t after igniting the plasma and $\Sigma(A_\mathrm{t} - A_\mathrm{t0})_z$ is the summation of $A_\mathrm{t} - A_\mathrm{t0}$ along the depth. Radial profiles of $\bar{A}_\mathrm{t} - \bar{A}_\mathrm{t=0}$ for both IC and H_2O_2 were generated using the t = 1 s time points. In order to increase the signal-to-noise, pixels were binned along the radial direction using bin sizes of 10 pixels and used to generate radial profiles of the average changes in absorbance for both IC and H_2O_2.

4.2.7 pH Effects

Since IC is a pH-dependent redox indicator, multispectral imaging was also performed on a pH-independent indicator to verify that the observed behavior was due to redox chemistry rather than a possible localized instantaneous pH effect. The pH-independent redox couple selected was ferricyanide ($Fe(CN)_6^{3-}$) and ferrocyanide ($Fe(CN)_6^{4-}$). Ultraviolet-Visible (UV-Vis) absorption spectroscopy was used to verify the characteristic wavelengths for the oxidized and reduced forms of the redox couple in order to assess an appropriate bandpass filter wavelength for the multispectral imaging experiments. All UV-Vis absorption spectra were acquired on a Cary 5000 (Varian) using a scan rate of 150 nm min^{-1} over the range of 350 to 600 nm. Two separate solutions were prepared with nominal concentrations of 100 µM $Fe(CN)_6^{3-}$ and 100 µM $Fe(CN)_6^{4-}$ to show the characteristic absorption features of the two oxidation states. The reduced form, $Fe(CN)_6^{4-}$, shows no absorption features above 400 nm, while the oxidized form, $Fe(CN)_6^{3-}$, exhibits a characteristic broad absorption peak between 400 and 450 nm. The effect of plasma treatment of the redox couple was investigated using a 20 mL mixture solution containing 25 μM $Fe(CN)_6^{3-}$ and 25 μM $Fe(CN)_6^{4-}$. The plasma treatment was performed for a duration of 4 minutes using a helium flow rate of 2000 sccm, an applied RF power of 40 W, and a gap height of 5.0 mm.

Multispectral imaging was only performed for visualizing the oxidation of $Fe(CN)_6^{3-}$ due to the fact that the complementary half-reaction was not known. Imaging experiments were performed using a macro quartz cuvette was filled with 45 mL of a freshly prepared mixture of 50 μM $Fe(CN)_6^{3-}$ and 50 μM $Fe(CN)_6^{4-}$. Images showing the oxidation of $Fe(CN)_6^{4-}$ were captured using a 400 nm bandpass filter (65-132, Edmund Optics) with a FWHM of 10 nm and an exposure time of 6000 μs.

4.3 Results & Discussion

4.3.1 Electrochemical Mapping

Spatial electrochemical mapping of the time-averaged potential ($\bar{\eta}_{\mathrm{rz}}$) in solution near the electrochemically active PLI revealed regions with more negative and positive potentials with respect to the bulk solution as shown in Figure 4.2c-d. The time-averaged values were determined by averaging the η_{rz} values acquired over the 45 second duration at each spatial location using

$$\bar{\eta}_{\mathrm{rz}} = \frac{1}{N}\sum_{i=1}^{N}\eta_{\mathrm{rz}}(i) \tag{4.4}$$

where N is the total number of measurements made over the acquisition period and $\eta_{\mathrm{rz}}(i)$ is relative reduction potential value of the ith measement. Qualitatively, the radial profiles of $\bar{\eta}_{\mathrm{rz}}$ showed similar trends at each depth below the PLI (Figure 4.2c). The main influence of varying the depth below the PLI had on the electrochemical measurements was on the observed magnitude of $\bar{\eta}_{\mathrm{rz}}$. The magnitude of $\bar{\eta}_{\mathrm{rz}}$ was greatest immediately underneath the PLI, suggesting that the electrochemical half-reactions occur at higher rates closer to the surface. As the E_{rz} reference electrode moved away from the surface, the magnitude of $\bar{\eta}_{\mathrm{rz}}$ decreased with increasing depth, suggesting that the measured potential approaches that of the bulk solution. Given that varying the depth had no observable influence on the sign of $\bar{\eta}_{\mathrm{rz}}$, the radial distribution of $\bar{\eta}_{\mathrm{rz}}$ was explored in order to understand where the half-reactions were taking place.

For a fixed depth, the electrochemical profiles revealed that the sign of $\bar{\eta}_{\mathrm{rz}}$ had undergone a sign inversion as the radial distance from the APPJ centerline was increased, as shown in Figure 4.2c. A similar measurement technique has been utilized in corrosion research, termed the scanning reference electrode technique (SRET), wherein potential variations between reference electrodes in a solution are used to identify the locations of cathodic and anodic reactions in systems without an external circuit (e.g. a piece of metal corroding in saline water).[74] In the field of corrosion, cathodic and anodic sites on electrochemically active surfaces are identified by regions with potential differences that are more negative and positive, respectively.[74,76] Figure 4.2c shows that the sign of $\bar{\eta}_{\mathrm{rz}}$ was negative for all $r \leq 2.5$ mm from the APPJ centerline. Following the same convention as the SRET, the negative sign of $\bar{\eta}_{\mathrm{rz}}$ (i.e. more negative value) would suggest that the reduction half-reaction is favored at radial distances closest to the PLI, which is consistent with the observed behavior from our previous work.[122] In fact, $\bar{\eta}_{\mathrm{rz}}$ was found to be most negative at radial distances of $r \leq 0.5$ mm from the APPJ centerline regardless of depth below the PLI. As the radial distance from the APPJ increased, the sign of $\bar{\eta}_{\mathrm{rz}}$ became less negative and experienced an inversion from negative to positive at $r \approx 3.0$ mm (Figures 4.2c-d). Positive values of $\bar{\eta}_{\mathrm{rz}}$ indicate that the complementary oxidation half-reaction occurs in this region immediately surrounding the reduction half-reaction. The value of $\bar{\eta}_{\mathrm{rz}}$ became increasingly positive and reached a maximum at a radial distance of $r \approx 4.0$ mm. Further than 4.0 mm from the jet centerline, the value of $\bar{\eta}_{\mathrm{rz}}$

decreased to approximately zero for $r \geq 8.0$ mm, meaning the electrochemical activity was indistinguishable from that of the bulk solution.

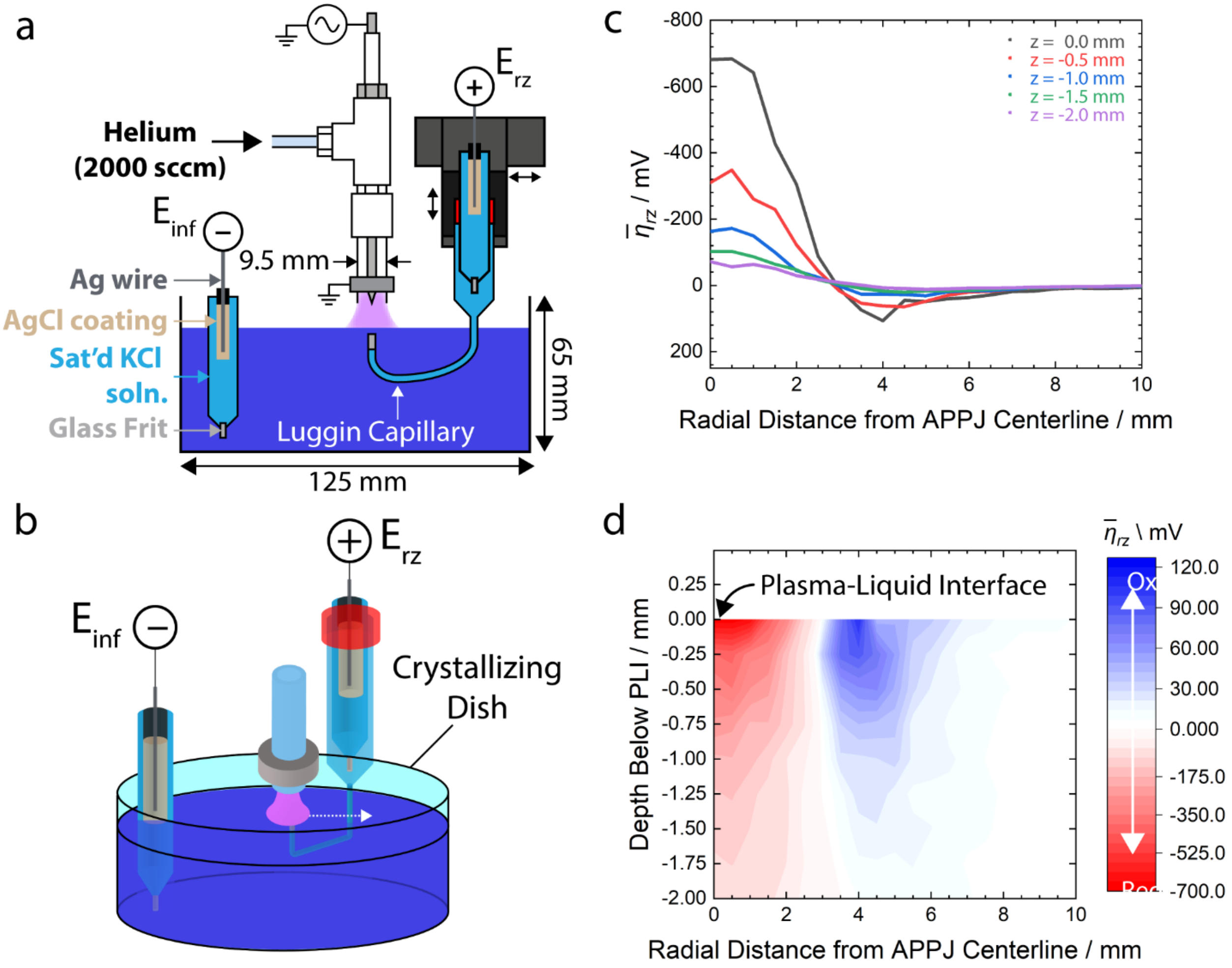

Figure 4.2. Spatial Reduction Potential Distribution Near Plasma-Liquid Interface (PLI). (a) Schematic representation of plasma jet and scanning reference electrode, E_{rz}, housed in a Luggin capillary used to measure the local potential in the liquid near the plasma liquid interface with respect to an identical reference electrode fixed in the bulk solution, E_{inf}. (b) Schematic illustrating the experimental apparatus used to measure the relative reduction potential profiles near the atmospheric pressure plasma jet (APPJ) centerline showing axial symmetry. (c) Examples of time-averaged relative reduction potential profiles, $\overline{\eta}_{rz}$, as a function of radial distance, r, from the APPJ centerline at various depths, z, below the PLI. (d) Contour map generated from the data in (c). Negative potentials (red) are regions where reduction is favored, and positive potentials (blue) are regions where oxidation is favored.

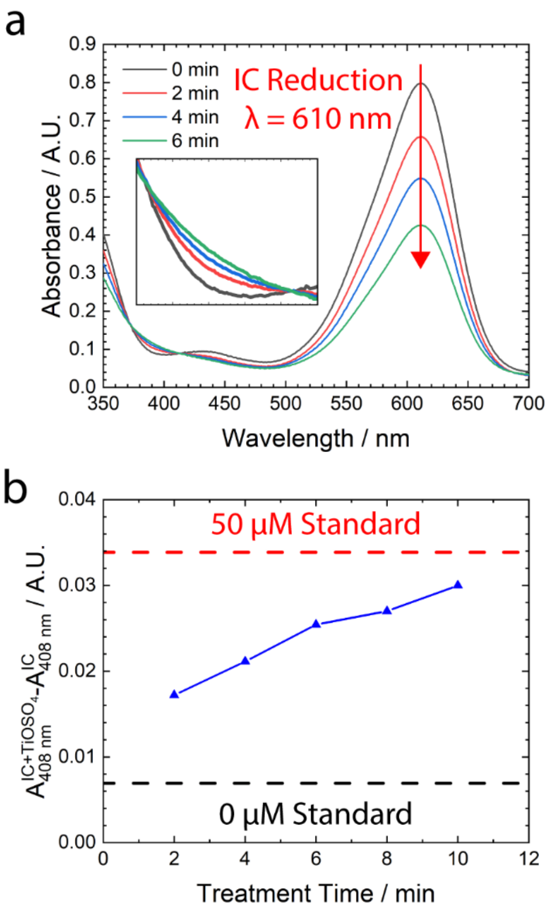

Figure 4.3. UV-Vis Absorption Spectra of Redox Products. (a) Absorption spectrum of 50 μM indigo carmine (IC) solutions treated with helium plasma for various treatment times. Red arrow indicates the peak used to observe reduction of IC^{2-} in multispectral imaging experiments. Inset illustrating the changing baseline at 408 nm. (b) Change in absorbance at 408 nm of 50 μM IC solutions after plasma treatments for various durations. The plotted value is the difference in absorbance between with and without titanium oxysulfide ($TiOSO_4$) in solution. Dashed lines indicate the absorbance at 408 nm of standards with the specified concentration of H_2O_2 and $TiOSO_4$.

Table 4.1. Indigo carmine concentration after plasma treatment. A summary of the oxidized form of IC^{2-} for various plasma treatment times.

Treatment Time / min	Absorbance / A.U.	IC^{2-} Concentration / μM
0	0.798	42.2
2	0.657	34.7
4	0.549	28.9
6	0.425	22.3

4.3.2 UV-Vis Absorption Spectroscopy

In addition to spatial electrochemical mapping, spectrophotometric methods were used to identify products of reactions between the plasma and electrolytic solution. The redox indicator IC is commercially available in its oxidized state (IC^{2-}) with a characteristic absorption peak at 610 nm (Figure 4.3a). When IC^{2-} is reduced to H_2IC^{2-}, this characteristic peak decreases, as demonstrated in the UV-Vis absorption spectra of plasma treated IC solutions shown in Figure 4.3a. The reduction of IC^{2-} occurs through a two proton, two electron transfer process. The change in concentration for IC^{2-} after plasma treatment can be determined based on the changes in absorbance at 610 nm. The absorbance peak decreases from 0.798 to 0.425 for treatment times of 0 and 6 min, respectively. A plot of the calibration curve of the IC^{2-} standards is shown in Figure 4.4, and the concentrations of IC^{2-} as a function of plasma treatment time are listed in Table 4.1. The change in absorbance after 6 minutes of plasma treatment was found to correspond to a reduction of 19.9 μM, which would require a stoichiometric equivalence of 39.8 μM of protons. Given the proton concentration in solution before plasma treatment was on the order of 10^{-5} μM, to protons used in the reduction of IC^{2-} must have been produced by a reaction promoted by the plasma-liquid interface A likely proton generating reaction is water oxidation, which produces both protons and hydrogen peroxide.[128–130] Hydrogen peroxide (H_2O_2) is an oxidant and a long-lived species that is well-known to be produced in atmospheric plasma systems that are in contact with aqueous solution, and in addition to water oxidation, it can also form as a result of recombination of gas phase hydroxyl radicals in the liquid.[67,119] Detection of H_2O_2 can be achieved using colorimetric methods, such as the titanium sulfate method.[127] The titanium sulfate method involves the formation of a complex between H_2O_2 and titanium sulfate that has a deep yellow color with an absorbance at 408 nm; a wavelength at which interference from reduced H_2IC^{2-} is minimized (Figure 4.3a). Thus, differences in the absorbance between plasma treated IC solutions with and without the addition of titanium (IV) oxysulfate ($TiOSO_4$) were compared to characterize the formation of H_2O_2 (Figure 4.3b). Using these molecular probes and their characteristic absorption features, *in situ* multispectral imaging was used to spatially visualize where molecular products of reduction and oxidation formed as a result of plasma treatment

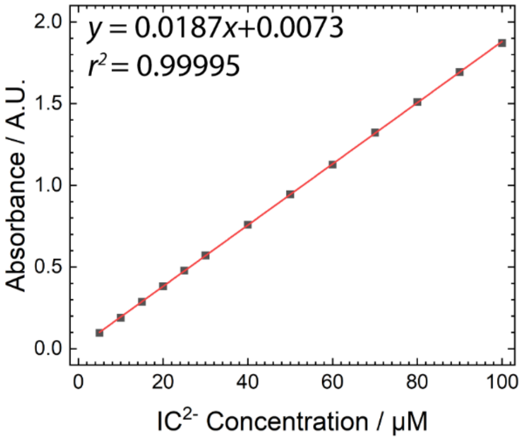

Figure 4.4. Calibration Curve of Indigo Carmine. The calibration curve generated for the indigo carmine (IC^{2-}) over the concentration range of 5–100 μM. Data points are indicated by black squares while the fitted line is displayed in red. Equation for regression line displayed in the plot.

4.3.3 Multispectral Imaging

Multispectral imaging was performed using a CMOS camera equipped with a bandpass filter corresponding to the characteristic wavelength of the species of interest, determined via UV-Vis absorption spectroscopy. Only images acquired at short times after plasma ignition were considered, whereat convolution by transport effects was minimized. The full details of the imaging processing are given in the experimental section. Briefly, an initial image was acquired prior to igniting the plasma and used as the reference frame. The spatially resolved pixel intensities for frames acquired after plasma ignition were processed with respect to that reference frame to produce still images of the spatiotemporal changes in absorbance, shown in Figure 4.5. Thus, negative values (red) correspond to a decreasing absorbance while positive values (blue) correspond to an increasing absorbance at a particular position and wavelength. Multispectral imaging experiments revealed that both H_2IC^{2-} and H_2O_2 were formed in spatially distinct regions within the solution (Figure 4.5). Within 10 seconds of plasma ignition, transport effects were observed to result in mixing and recirculation of products and the bulk

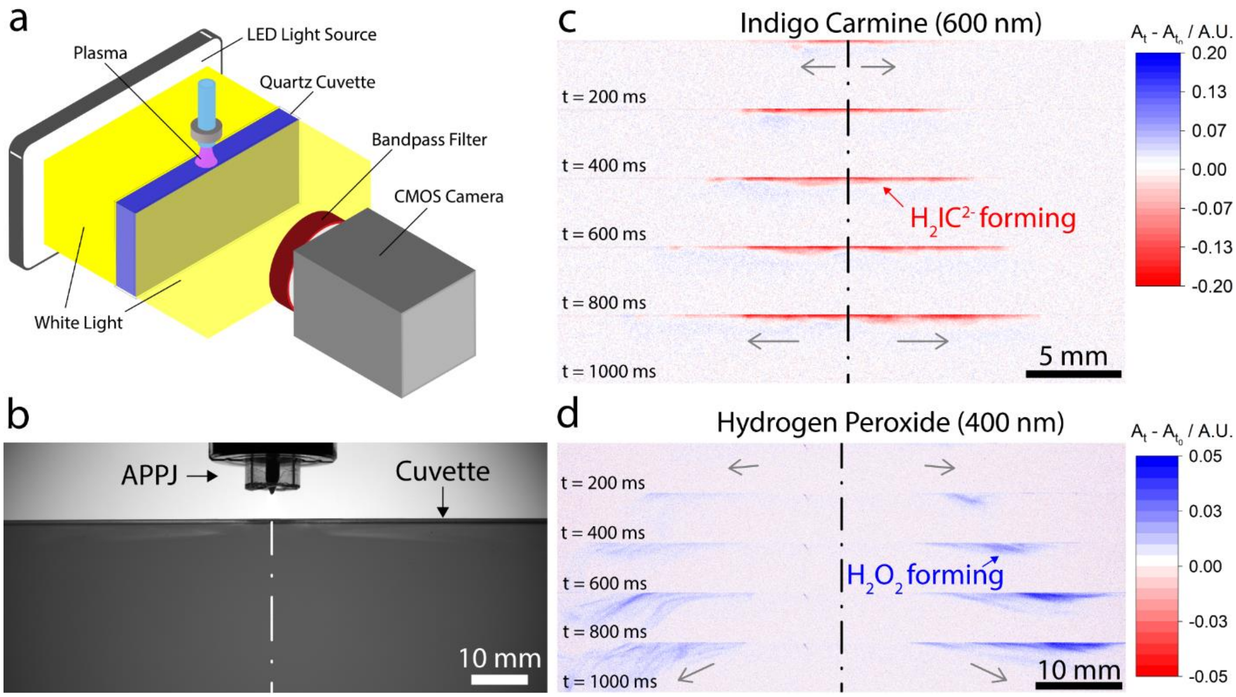

Figure 4.5. Multispectral Imaging. (a) Schematic illustrating the multispectral imaging apparatus to visualize redox reactions in plasma treated solutions. (b) A representative raw image of a 50 µM IC solution undergoing plasma treatment taken with the CMOS camera acquired using an exposure time of 8000 µs with a 600 nm bandpass filter. (c) Images of 50 µM IC solution acquired with a 600 nm bandpass filter at various times after plasma ignition. (d) Images of 50 µM IC solutions with excess $TiOSO_4$ acquired with a 400 nm bandpass filter at various times after plasma ignition. Dotted-dashed lines indicate the atmospheric pressure plasma jet (APPJ) centerline and gray arrows indicate the flow direction of the species in the liquid.

Multispectral imaging experiments revealed that both H_2IC^{2-} and H_2O_2 were formed in spatially distinct regions within the solution (Figure 4.5). Within 10 seconds of plasma ignition, transport effects were observed to result in mixing and recirculation of products and the bulk solution, thus only short time scales were considered to determine where redox products were forming. The processed multispectral still images in Figure 4.5 show the changes in absorbance at various times after plasma ignition with respect to an initial frame acquired prior to turning the plasma on. Multispectral imaging of IC using a 600 nm filter revealed that the reduction of IC^{2-}

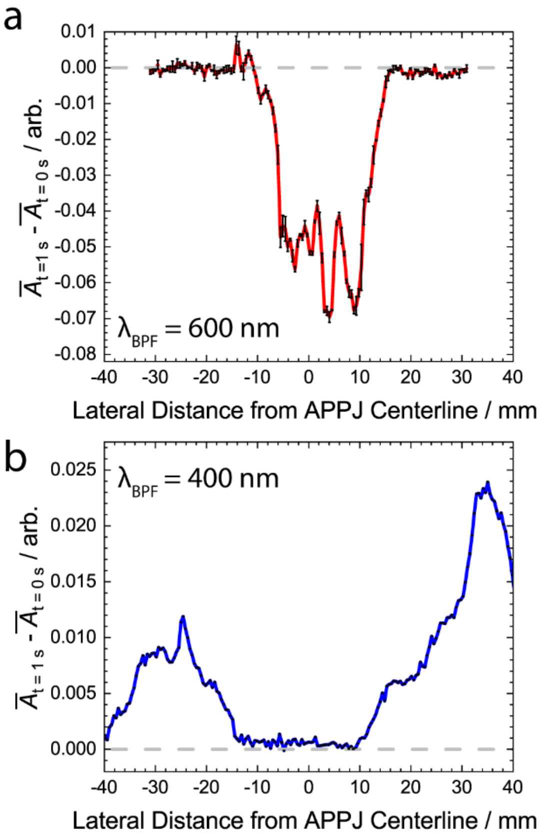

Figure 4.6. Lateral Profiles of Average Absorbance Change. (a) Profile of the change in absorbance at 600 nm generated using the multispectral image of IC^{2-} reduction from Figure 4.5c, 1 second after plasma ignition. (b) Profile of the change in absorbance at 400 nm generated using the multispectral image of H_2O_2 formation from Figure 4.5d, 1 second after plasma ignition. Data were binned to increase signal-to-noise and black error bars are the standard deviation of absorbance due to shot-to-shot variations on a time scale of 20 ms (images not shown). Dashed gray line is the baseline.

was confined near the PLI, aligned directly underneath the APPJ centerline (Figure 4.5c). Shortly after the plasma was ignited, the reduced product was transported laterally outward. Multispectral imaging of H_2O_2 was performed by adding $TiOSO_4$ to an IC solution with a 400 nm bandpass filter. The formation of H_2O_2 was only observed at lateral distances of approximately 10 mm or greater from the APPJ centerline, as shown in Figure 4.5d. As time after igniting the plasma elapsed, H_2O_2 began to move laterally outward. The results were both consistent with other reports of plasma-induced chemistry using colorimetric probes, where the reaction emanates from the plasma-liquid interface and transports to the bulk with increasing time.[69] The spatial distributions of both IC and H_2O_2 were found to be slightly asymmetric about the APPJ centerline, but more pronounced in the case of H_2O_2. Relative to the APPJ centerline, H_2O_2 appears to move downward within the solution on the left-hand side, while accumulating near the surface on the right-hand side (Figure 4.5d).

To account for the dispersion of the products, still images were used to generate lateral profiles of the changes in absorbance. These profiles were generated by averaging over a depth of 2.0 mm at a given lateral position. The lateral profiles of the change in absorbance at 1 second after plasma ignition are shown in Figure 4.6 for both IC and H_2O_2. In the case of IC, the average change in absorbance was found to be negative for lateral distances of approximately $|x| \leq 14$ mm with respect to the APPJ centerline as shown in Figure 4.6a, which is consistent with the reduction reaction occurring near the plasma jet centerline. For $|x| > 14$ mm, the average change in absorbance goes to zero, indicating that the IC solution in this region remained unchanged relative to the initial solution. Conversely, the average change in absorbance for H_2O_2 was found to be zero for lateral distances $|x| \leq 13$ mm, suggesting that H_2O_2 was not forming close to the APPJ centerline as shown in Figure 4.6b. At greater lateral distances from the APPJ centerline, the average change in absorbance became increasingly positive reaching a maximum at approximately $|x| = 30$ mm, suggesting that H_2O_2 is most favorably formed in the region surrounding the PLI. Even further away from the jet centerline beyond $|x| \geq 30$ mm, the value of the average absorbance decreased towards the baseline value of zero. The pH change for the IC solution used in the multispectral imaging experiments was found to be negligible, changing from 11.2 to 11.0 after treatment.

While the spatial electrochemical measurements and multispectral imaging experiments revealed the same qualitative trend, namely reduction reactions occurring near the PLI with the complementary oxidation half-reactions taking place in the surrounding solution, there is a discrepancy in the characteristic lengths between the two methods. More specifically, the boundary between the half-reactions was found to occur at a radial distance of $r \approx 3.0$ mm in the spatial electrochemical measurements and at a lateral distance of $|x| < 13$-14 mm for the multispectral imaging experiments. One plausible reason for this discrepancy is the size of the Luggin capillary used to make the measurements near the PLI. While the radial measurements were performed in increments of 0.5 mm, the diameter of the probe was 3.0 mm. Thus, the actual distances between the reduction and oxidation zones may be distorted. A key difference between the two data sets was the vessel geometry and size used in the experiments for each method (Figures 4.2b and 4.6a), which would likely influence the transport and recirculation of species between the two characterization techniques. For multispectral imaging experiments, solutions were plasma treated in a rectangular quartz cuvette with dimensions of 102.5 mm × 12.5 mm × 45 mm (l × w × h). Unfortunately, the reference electrodes used for electrochemical measurements had outer diameters of 16 mm, and thus, the spatial electrochemical characterization could not be performed simultaneously in the vessel used for imaging. Instead, electrochemical characterization was performed in cylindrical vessels with a diameter of 125 mm and a height of 65 mm (Figure 4.2a). Furthermore, transport effects likely broaden the data in Figure 4.6 when compared to Figure 4.2.

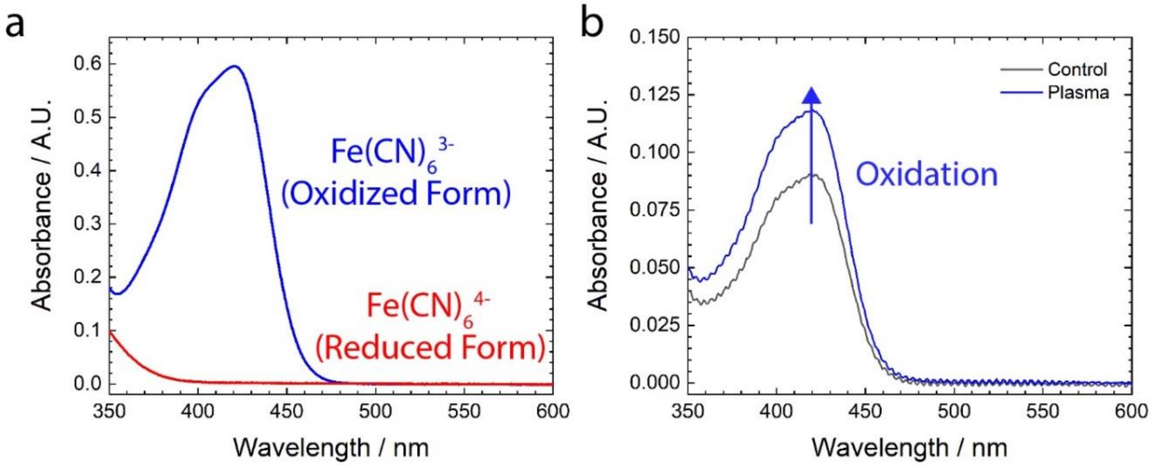

Figure 4.7. UV-Vis Absorption Spectrum of $Fe(CN)_6^{3-}$/$Fe(CN)_6^{4-}$. (a) UV-Vis absorption spectrum showing characteristics of the 100 μM of the reduced ($Fe(CN)_6^{4-}$) and 100 μM of the oxidized ($Fe(CN)_6^{3-}$) forms of the redox couple. (b) UV-vis absorption spectrum of an untreated control and a plasma treated $Fe(CN)_6^{3-}$/$Fe(CN)_6^{4-}$ (25 μM/25 μM) mixture.

4.3.4 pH Independent Redox Indicator

Given the fact that IC is a pH-dependent redox indicator, multispectral imaging was also performed on a pH-independent indicator, $Fe(CN)_6^{3-}$/$Fe(CN)_6^{4-}$, to verify that the observed behavior was due to redox chemistry rather than a possible localized instantaneous pH effect. The reduced form, $Fe(CN)_6^{4-}$, shows no UV-Vis absorption features above 400 nm, while the oxidized form, $Fe(CN)_6^{3-}$, exhibits a characteristic broad absorption peak between 400 and 450 nm (Figure 4.7a). The UV-Vis absorption spectrum of the plasma treated solution was compared to an untreated control (i.e. 0 minute treatment time), as shown in Figure 4.7b. The plasma treated solution revealed that $Fe(CN)_6^{4-}$ was becoming oxidized as a result of plasma treatment, as indicated by the increased absorbance between 400 and 450 nm relative to the untreated control (Figure 4.7b). Multispectral imaging was only performed for visualizing the oxidation of

$Fe(CN)_6^{3-}$ due to the fact that the complementary half-reaction was not known. While the reduction of $Fe(CN)_6^{4-}$ is a possibility, the multispectral imaging apparatus used in this work is incapable of detecting the reaction. Other possible reduction products, such as hydrogen gas, would be difficult to characterize as well.

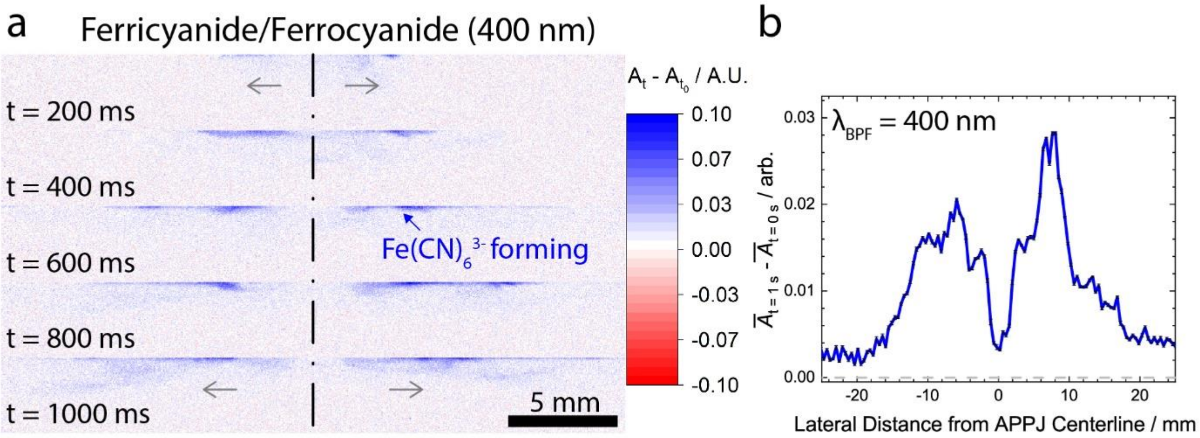

Figure 4.8. Multispectral Imaging and Lateral Profile of Average Absorbance Change of $Fe(CN)_6^{3-}$/$Fe(CN)_6^{4-}$. (a) Images of a mixed 50 μM $Fe(CN)_6^{3-}$/50 μM $Fe(CN)_6^{4-}$ solution acquired with a 400 nm bandpass filter at various times after plasma ignition. Black dotted-dashed line represents the APPJ centerline and gray arrows indicate flow direction of $Fe(CN)_6^{3-}$ in the liquid. (b) Profile of the change in absorbance at 400 nm generated using the multispectral image of $Fe(CN)_6^{3-}$ formation from (a), 1 s after plasma ignition. Data were binned to increase signal-to-noise and black error bars are the standard deviation of each bin. Dashed gray line is the baseline.

The processed multispectral still images in Figure 4.8a show the changes in absorbance at various times after plasma ignition with respect to an initial frame acquired before turning the plasma on. Multispectral imaging of the $Fe(CN)_6^{3-}$/$Fe(CN)_6^{4-}$ mixture revealed that oxidation of $Fe(CN)_6^{4-}$ was occurring near the APPJ centerline, with the $Fe(CN)_6^{3-}$ product transporting laterally outward with time. Interestingly, a node with no change in absorbance formed directly underneath the APPJ centerline, suggesting that oxidation of $Fe(CN)_6^{4-}$ was not occurring in this region. The value of the average change in absorbance (Figue 4.8b) was found to be close to the baseline value at a lateral distance of approximately $|x| \leq 0.5$ mm. At greater lateral distances, the average absorbance value becomes increasingly positive before reaching a maximum at $|x| = 7$ mm, suggesting that the oxidation of $Fe(CN)_6^{4-}$ is most favorably occurring in this region. Even further away from the centerline, the average change in absorbance decreases and eventually returns to the baseline value at an approximate lateral distance of $|x| = 18$ mm from the centerline. While the length scale of oxidation product formation differed from the hydrogen peroxide (H_2O_2) multispectral imaging experiments discussed earlier, both data sets revealed the same qualitative trend in the average absorbance profile. Despite the fact that the oxidation of $Fe(CN)_6^{4-}$ to $Fe(CN)_6^{3-}$ was observed to occur in close proximity to the APPJ centerline, the apparent node clearly demonstrated that oxidation products were not forming directly underneath the PLI. In fact, the multispectral still images and average change in absorbance revealed that oxidation half-reaction was actually favored in the region surrounding the PLI rather than directly underneath the PLI itself. The results from the multispectral imaging experiments show a consistent trend for both pH-dependent and pH-independent redox indicators, suggesting that the observed behavior is due to redox chemistry rather than an artifact due to localized pH effects.

4.4 Conclusions

In summary, a helium RF plasma jet impinging on an aqueous solution containing the redox indicator indigo carmine was used as a model system to identify where redox half-reactions occur in electrodeless plasma-liquid configurations. The conclusions of this work are supported by two independent experimental methods of *in situ* electrochemical measurements and multispectral imaging using colorimetric molecular indicators. Reduction reactions take place near the plasma jet centerline, and oxidation reactions take place in the adjacent solution. Spatial electrochemical measurements revealed values of $\overline{\eta}_{rz}$ that were negative for $0 < r < 2.5$ mm, and positive for $3.0 \leq r < 8.0$ mm; indicative of reduction and oxidation half-reactions, respectively. The multispectral imaging results revealed a decreased absorbance for IC at 600 nm for $|x| \leq 14$ mm, suggesting that IC^{2-} was reduced to H_2IC^{2-} in that region. The addition of $TiOSO_4$ to the IC solution showed an increased absorbance at 400 nm for $|x| \geq 13$ mm, indicative of the formation of a product of water oxidation H_2O_2. The results of both data sets suggest that the electrodeless cathode is located directly underneath the PLI, while the electrodeless anode is surrounding in the adjacent solution. Despite the apparent disparity in the characteristic lengths of electrodeless anode and cathode between the two experimental methods, the data sets show the same qualitative behavior. More specifically, the electrodeless cathode is located directly underneath the PLI, while the electrodeless anode is in the surrounding solution.

Chapter 5

Plasma Parameters and the Reduction Potential at a Plasma-Liquid Interface

5.1 Introduction

The increasing availability and decreasing cost of renewable electricity has prompted research into electrified chemical processing whereby electrical energy is used to drive chemical transformations.[1,131] Electricity-intensive processing techniques such as electrochemistry using solid electrodes has attracted attention in this context for the synthesis of organic compounds, such as high-value pharmaceuticals[9] and renewable chemical production.[132] Chemical transformations are achieved in conventional electrochemical systems by applying an external bias to a solid electrode allowing for the preferential transfer of electrons between the electrode-liquid interface. The ability to perform controlled reduction-oxidation (redox) reactions in electrochemical systems is realized by adjusting the electrode potential at the electrode-liquid interface via external circuitry. However, conventional electrochemical configurations have been shown to suffer from complications including fouling of the electrode surfaces by carbonaceous coatings[12,133,134] and conversions being influenced by the choice of a supporting electrolyte.[14] Another way to utilize electricity to drive chemical reactions is by employing nonthermal plasma in contact with liquids. Nonthermal atmospheric plasma interacting with liquids have been utilized for a variety of applications including wastewater treatment,[114,135] chemical conversion,[58,136] and nanomaterial synthesis.[111,137] These applications are based on electrochemical reactions induced by charge-transfer processes taking place across the interface formed between the plasma and electrolyte solution (i.e. plasma-liquid interface). Nonthermal plasma in contact with liquids can act as a source of reactive species such as solvated electrons and atomic hydrogen,[63,49] which can facilitate redox reactions within solution. Nonthermal plasma-liquid interactions have been described as a means of performing electrodeless electrochemistry.[138] As demonstrated in the previous chapter, nonthermal free APPJs in contact with liquids are able to form an electrodeless cathode and anode in the liquid capable of promoting selective organic transformations.[122] An electrodeless approach is hypothesized to ameliorate issues of electrode fouling experienced using solid electrodes.[12,133,134] Moreover, plasma electrochemical systems do not require the addition of a supporting electrolyte. Despite these features compared to conventional electrochemical systems, a means of performing controlled chemical transformations on the liquid side of the plasma-liquid interface has not been clearly identified. More specifically, a framework for understanding how the reduction potential in plasma-liquid systems can be tuned for controlled electrochemistry has not been established.

Electrochemical reactions are driven by differences in the electrochemical potential of electrons between dissimilar phases, resulting in the transfer of electrons across the interface formed between the phases until equilibrium is reached. In the case of conventional electrochemical systems, the external bias applied to the solid electrode constrains the local electrode potential at the electrode-liquid interface to a particular value, driving the redox reaction in the direction to reach local equilibrium with that reduction potential. We hypothesize an analogous constraint to occur in plasma-liquid systems, wherein the local reduction potential in the liquid immediately underneath the plasma-liquid interface is controlled by the state variables of the plasma (i.e. electron density and electron temperature) above the interface.

In this chapter, we investigate the effect that the electron density and electron temperature have on the observed reduction potential directly underneath the plasma-liquid interface. The electron density, n_e, and electron temperature, T_e, were acquired by means of laser Thomson scattering of a radiofrequency (RF) argon (Ar) atmospheric pressure plasma jet (APPJ). Characterization of the reduction potential in solution was performed using a previously reported technique,[122] where a reference electrode is used to measure the local potential within the solution directly underneath the electrochemically active plasma-liquid interface, E_{PLI}, relative to the potential measured by a nominally identical reference electrode in the bulk solution, E_{inf}. The relative reduction potential in solution near the plasma-liquid interface, η_{PLI}, is given by

$$\eta_{\mathrm{PLI}} = E_{\mathrm{PLI}} - E_{\mathrm{inf}} \, . \tag{5.1}$$

Treating the liquid as an electrically floating surface, a negative charge would be expected to form in order to balance the flux of hot electrons and relatively slow positive ions from the plasma phase to the liquid.[79,139] Thus, the constraining potential at the plasma-liquid interface is expected to be proportional to the floating potential, which can be approximated using an analytical model if n_e and T_e are known. Interestingly, the empirical values of the relative reduction potential near the plasma-liquid interface, η_{PLI}, were found to be in good agreement with the model-predicted reduction potential determined using the plasma parameters obtained from the Thomson scattering experiments.

5.2 Experimental

5.2.1 Plasma Source

The plasma source studied in this work was a RF (13.56 MHz) Ar APPJ shown in Figure 5.1. The APPJ was comprised of a powered nickel needle electrode with an outer diameter of 2.3 mm housed within an alumina tube with inner and outer diameters of 3.2 mm and 9.5 mm, respectively. The ground electrode was an aluminum ring with an inner diameter of 9.5 mm, which was mounted to the exterior of the alumina tube at a distance of 5 mm from the tube outlet. The Ar flow rate was maintained at a constant flow rate of 1000 standard cubic centimeters per minute (sccm) using a mass flow controller (GE50A, MKS Instruments). The plasma was generated using a RF power supply (AG 0613, T&C Power Conversion) connected to an impedance matching network (AIT-600 RF Auto Tuner, T&C Power Conversion) and synchronized to the laser source using a pulse generator (Model 575 Pulse/Delay Generator, Berkeley Nucleonics Corporation). The RF excitation frequency was modulated with a 20 kHz pulse with a duty cycle of 20%.

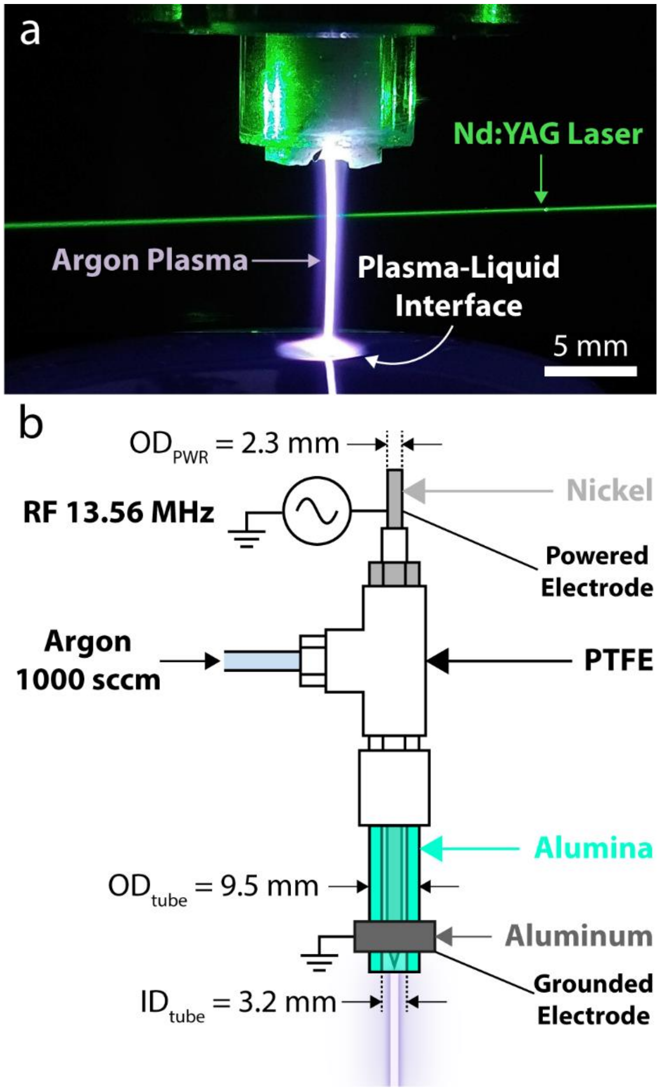

Figure 5.1. Laser Thomson scattering of a radiofrequency argon plasma jet. (a) Image of a frequency-doubled Nd:YAG laser passing through core of radiofrequency (RF, 13.56 MHz) argon plasma jet in contact with liquid. The RF excitation frequency was modulated with a 20 kHz pulse with a duty cycle of 20%. (b) Schematic representation of RF argon plasma jet shown in (a) with important dimensions specified.

5.2.2 Light Scattering

Characterization of the Ar APPJ used in this work was accomplished by means of laser light scattering. All laser diagnostics reported in this work were performed in the Princeton Collaborative Research Facility at the Princeton Plasma Physics Laboratory. The laser source for the light scattering experiments was a frequency-doubled Nd:YAG laser (λ_0 = 532 nm, Continuum SL-III, Surelite). The laser was Q-switched at a repetition rate of 10 Hz, generating a beam with a pulse width of 8 ns (full width at half max, FWHM) and a maximum pulse energy of 550 mJ. A schematic for the experimental apparatus used for the laser scattering experiments is shown in Figure 5.2. The incident laser was focused with a lens (focal distance f = 1 m) and the laser spot size interacting with the plasma was determined to be 318 μm in diameter. The laser pulse energy used in the experiments was measured using a pyroelectric energy sensor (ES220C, ThorLabs) and found to be 60 mJ. The operating laser fluence used for Raman and Thomson scattering was 75.6 J cm^{-2}, which was found to be less than the critical fluence that would result in inverse bremsstrahlung heating of electrons (Appendix I). The orientation of the detection arm was orthogonal (ϕ = 90°) to the axis of the incident laser. Light scattered by the plasma was focused (f = 200 mm) through a 200 μm pinhole, which acted as a spatial filter. A volume Bragg notch filter was used to physically remove the Rayleigh component of the scattered light. The filter was a reflecting volume Bragg grating (VBG) and was specified to block light with an optical density of 4 with a FWHM of 5-8 cm^{-1} (0.14-0.23 nm). The transmission of the filter outside the blocking region is 80%. The reflected wavelength can be tuned by rotating the filter. Setting an angle of 6° between the filter normal and the direction of the incoming light results in the reflection of 532 nm light, which is the central wavelength (λ_0) of the laser. The main drawback of the VBG filter is the small angular acceptance of less than 0.1°, therefore, adequate collimation of the scattered light is crucial for rejecting Rayleigh scattered light. Light exiting the pinhole was collimated (f = 50 mm) before passing the volume Bragg notch filter, and focused (f = 50 mm) into the entrance slit of the monochromator (SpectraPro HRS-750, Princeton Instruments) and projected onto an intensified CCD (iCCD) camera (Pi-Max 3 Model 1024i, Princeton Instruments). Irises were placed along the detection arm in order to minimize stray light due to light scattering off of solid surfaces. The iCCD captures a two-dimensional image with the spectral dispersion (wavelength) along the horizontal axis and spatial information along vertical axis. The iCCD images of the collected scattered light were averaged over 10000 accumulations (17 minutes) for each spectrum. A digital pulse/delay generator was used to synchronize the laser, RF power supply, and iCCD camera. The synchronization of the plasma was based on detecting the time delay between the 20 kHz pulse used to modulate the RF excitation frequency and the beginning of the observable laser pulse that produced the largest Balmer-α (H_α, 656.3 nm) emission line, which was assumed to correspond to the timing with the largest electron density. Using optical emission spectroscopy (OES), a time delay of 9.981 μs was found to have the highest H_α intensity for each RF power evaluated.

Laser light scattering was performed on an Ar APPJ treating a 75 μM indigo carmine (IC) solution with an adjusted pH of 10. The solution was contained in a PTFE crystallizing dish (325 mL), which produced a positive meniscus. The PTFE dish was connected to a large reservoir (14 L) containing freshly prepared 75 μM IC solution (pH 10) in order to maintain a constant liquid height in the PTFE dish via hydrostatic pressure while the Thomson signal was being acquired. The plasma was positioned such that the end of the tube was at a fixed height of 10 mm above the surface of the solution, with the laser passing through the plasma at a height of 9 mm above the liquid surface (see inset of Figure 5.2). Thomson signal was acquired as a function of RF power

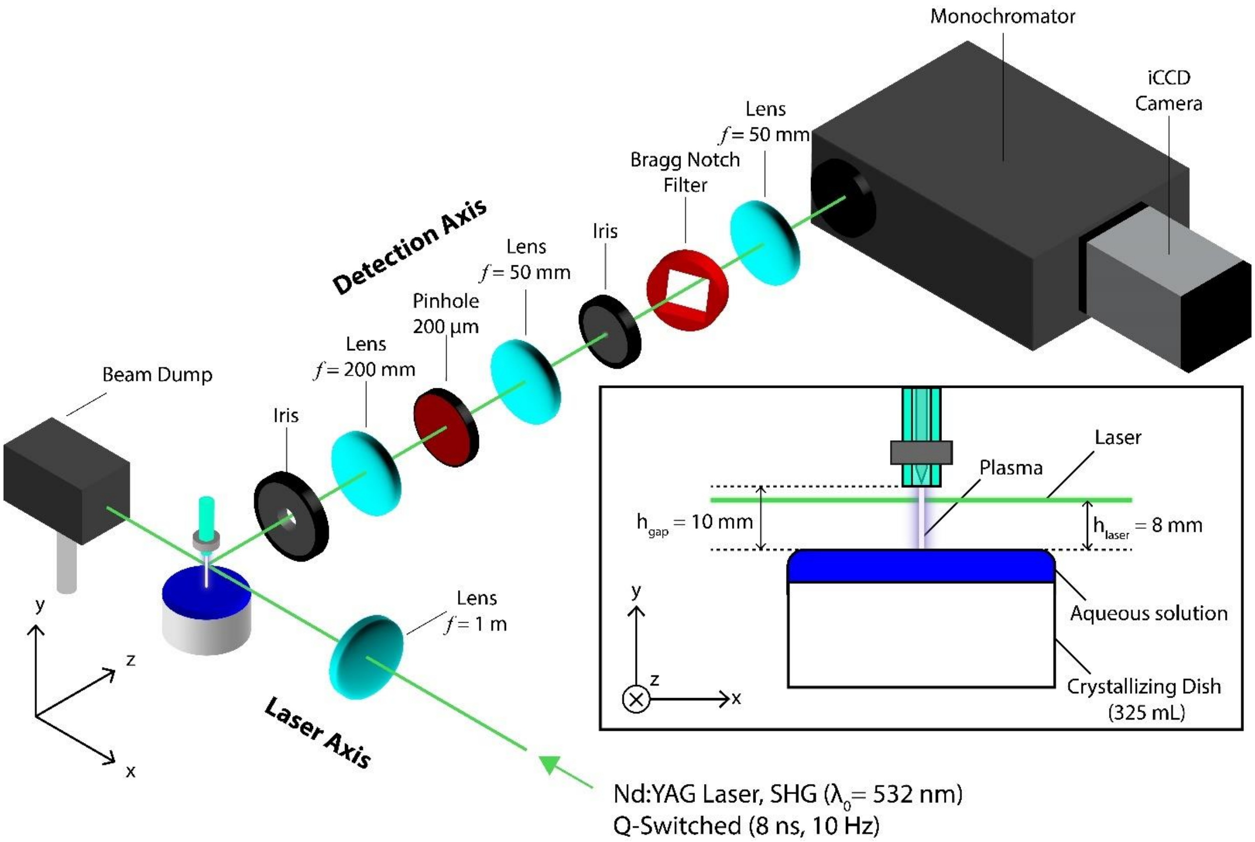

Figure 5.2. Schematic of the experimental laser light scattering setup. Laser source used in Raman and Thomson scattering experiments. A Q-switched frequency-doubled Nd:YAG laser was used to generate a beam with a central wavelength of 532 nm at a repetition rate of 10 Hz. The pulse width of the laser was 8 ns and the laser power used for acquiring Thomson signal was 60 mJ. Incident light is focused through a lens (*f* = 1m) and passed through the plasma at a distance of 2 mm below the APPJ tube ending, or 8 mm above the liquid surface (see inset). The scattered light was collected along the detection arm which was orthogonal to the incident beam. The scattered signal was focused (*f* = 200 mm) through a pinhole and collimated (*f* = 50 mm) through a Bragg notch filter to remove the Rayleigh component of the scattered light. The light was focused (*f* = 50 mm) before entering the monochromator and images were acquired using an intensified CCD (iCCD) camera.

over the range of 20-50 W, increasing the power in increments of 10 W. Prior to each Thomson experiment, the solution in the PTFE dish was replenished with fresh solution from the reservoir. An alignment procedure for centering the plasma jet along both the laser and detection axes was performed before each acquisition. The plasma jet was mounted to a two-axis micrometer positioning table, allowing for the relative position of the plasma jet to be adjusted in 25.4 μm increments along the laser and detection axes. Alignment of the plasma along the laser axis was based on locating the core of the plasma by means of Rayleigh scattering. More specifically, the position of the plasma along the laser axis was adjusted to minimize the Rayleigh signal detected by OES, which corresponds to the position with the lowest density of heavy particles due to ionization. Along the detection arm, alignment of the plasma with the entrance slit of the spectrometer was determined based on the position with the highest H_α emission via OES.

5.2.3 Electrochemical Characterization

Electrochemical characterization was carried out using a previously reported method,[122] based on measuring the potential difference between a position within the liquid near the plasma-liquid interface (E_{PLI}) and the bulk solution (E_{inf}). Briefly, the relative reduction potential was measured using identical Ag/AgCl reference electrodes connected to a digital multimeter (DMM6500, Keithley). The reference electrode measuring the relative reduction potential of the electrochemically active plasma-liquid interface was housed in a Luggin capillary (Adams & Chittenden) and positioned in the liquid directly underneath the impingement point of the plasma. The local reduction potential within the liquid underneath the plasma-liquid interface was referenced to the potential measured by an identical reference electrode positioned in the unaffected bulk solution. The relative reduction potential measurements were performed as a function of RF power in the same PTFE dish using in the Thomson scattering experiments using 75 μM IC (pH 10). The measured voltage difference between the electrodes prior to igniting the plasma was used for baseline subtraction. However, due to the stringent nature of the Thomson scattering experiments, the electrochemical measurements were performed asynchronously to avoid the introduction of additional stray light.

5.2.4 Ultraviolet-Visible Absorption Spectroscopy

In order to verify that the Ar APPJ used in this work was able to selectively reduce the model redox compound (IC), the composition of the solution was treated at the same RF powers used in the Thomson scattering experiments and evaluated using ultraviolet-visible absorption spectroscopy. Plasma treatments of IC were performed with the same Ar APPJ used in the Thomson scattering experiments to verify the selective reduction of the redox indicator. A fresh IC solution was prepared with a nominal concentration of 75 μM an adjusted pH of 10. Plasma treatments were performed using a gap height of 10 mm between the end of the APPJ tube and the solution surface. Treatments were performed on 20 mL volumes for a duration of 60 s using the same applied RF powers used in the Thomson scattering experiments. Immediately following treatment, 2 mL aliquots were drawn and used for ultraviolet-visible (UV-Vis) absorption spectroscopy. The UV-Vis absorption spectra were acquired on a Cary 5000 spectrophotometer (Agilent) over the wavelength range of 350-700 nm using a scan rate of 150 nm min^{-1}.

5.2.5 Electrical Characterization

The voltage applied to the electrode, V, was estimated based on measuring the peak voltage at powered electrode of the Ar APPJ. More specifically, the voltage waveforms were acquired using a high voltage probe (P6015A, Tektronix) and recorded with a digital oscilloscope (TDS 2014C, Tektronix) for each applied RF power used in the Thomson scattering experiments.

5.3 Data Analysis & Fitting

5.3.1 Laser Light Scattering

More detailed explanations regarding the theory behind light scattering of plasmas can be found elsewhere,[140–142] but a brief overview will be discussed. Light guided through a plasma can be scattered as a result of interactions between the incident electromagnetic radiation and heavy particles (Rayleigh scattering), molecules (Raman scattering), or unbound charged particles (Thomson scattering). Rayleigh scattering arises from elastic scattering of light by the electron clouds (i.e. bound electrons) of atoms and molecules.[140,143] Raman scattering describes the inelastic scattering of light with the bound electrons of molecules, which induce rotational and/or vibrational transitions.[144,145] Thomson scattering occurs as a result of elastic scattering of light from unbound charges (e.g. electrons or ions).[140,145,146] In the context of plasma laser diagnostics, analysis of the resulting light scattering spectrum for a given mechanism is key for extracting a characteristic density and/or temperature. Rayleigh scattering can be used to determine the background gas temperature (T_g), Raman scattering can provide the densities of molecular species (e.g. N_2 and O_2) and the rotational temperature (T_{rot}), and Thomson scattering can be used to extract the electron density (n_e) and electron temperature (T_e).[147]

The general form of the power of scattered light per unit wavelength, $P_\lambda(\lambda)$, for each scattering mechanism is expressed as[140,141]

$$P_\lambda(\lambda) = fLP_0\Delta\Omega \cdot n_i \cdot \frac{d\sigma_i}{d\Omega} \cdot S_i(\lambda) \tag{5.2}$$

where f is based on the efficiency of the optics and camera, L is the length of the detection arm, P_0 is the power of the incident laser, $\Delta\Omega$ is the solid angle of detection, n_i is the number density of species i, $\frac{d\sigma_i}{d\Omega}$ is the differential cross section of species i, and $S_i(\lambda)$ is function that describes the spectral distribution of scattered photons. While n_i, $\frac{d\sigma_i}{d\Omega}$, and $S_i(\lambda)$ are unique to the type of light scattering, $fLP_0\Delta\Omega$ is a system-specific geometrical factor that has a constant value for a particular apparatus and setup and does not depend on the scattering mechanism. Given that the profile of

$S_i(\lambda)$ takes on a specific form based on the type of light scattering, along with the fact that $\frac{d\sigma_i}{d\Omega}$ is typically a known quantity, the value of $fLP_0\Delta\Omega$ can be readily determined by performing light scattering under known conditions (*i.e.* species density and temperature) in a procedure known as absolute intensity calibration. More specifically, an experimental scattering spectrum, $P_{\exp}(\lambda)$, and a simulated spectrum calculated using Equation 5.2 can be used to find the intensity calibration factor by

$$fLP_0\Delta\Omega = \frac{P_{\exp}(\lambda)}{n_i \cdot \frac{d\sigma_i}{d\Omega} \cdot S_i(\lambda)} \cdot \tag{5.3}$$

For APPJs, the calibration factor is typically found by means of performing rotational Raman scattering under ambient conditions in open air. In the case of Thomson scattering, the $fLP_0\Delta\Omega$ factor is typically required to accurately determine the n_e. Thomson scattering can be categorized as being collective or non-collective depending on the relative scales of the incident laser wavelength, λ_0, and the electron Debye length, λ_D, given by

$$\lambda_D = \left(\frac{\varepsilon_0 k_B T_e}{q_e^2 n_e} \right)^{1/2} . \tag{5.4}$$

where ε_0 is the permittivity of free space, k_B is the Boltzmann constant, and q_e is the fundamental charge. More specifically, the scattering regime is determined by the value of the scattering parameter, α, expressed as

$$\alpha = \frac{1}{2\sqrt{2}\pi} \cdot \frac{\lambda_0}{\lambda_D} \tag{5.5}$$

which describes the degree of collectivity. Note that the first term on the right-hand side of Equation 5.5 only applies for systems in which the scattering angle $\phi = 90^{\circ}$ is orthogonal to the incident laser. Non-collective Thomson scattering occurs for $\lambda_0 \ll \lambda_D$ ($\alpha < 1$), where the incident light is scattered by individual electrons. Collective scattering takes place when $\lambda_0 \gg \lambda_D$ ($\alpha > 1$), where light is scattered by an ensemble (i.e. a collection) of electrons.

The spectral shape in a Thomson scattering experiment is a consequence of Doppler shifting of light due to the relative motion (velocity) of electrons with respect to both the incident laser beam and the detector. Thus, the resulting scattering spectrum is related to the velocity distribution of the electrons in the plasma. For non-collective Thomson scattering (*i.e.* $\lambda_0 \ll \lambda_D$), the randomly distributed electrons within the plasma result in the isotropic scattering of light. Assuming that the electron velocity distribution is Maxwellian, the observed Thomson spectrum would take on a Gaussian profile with a width proportional to T_e and an area proportional to n_e. It should be noted that the area is also dependent on $fLP_0\Delta\Omega$, as shown in Equation 5.2, highlighting the importance of proper calibration when determining n_e. For collective Thomson scattering (*i.e.* $\lambda_0 \gg \lambda_D$), light interactions with groups of electrons result in nonuniform scattering, introducing wave interference effects. While the underlying Maxwellian velocity distribution of electrons profile is still present, the spectral distribution function is modified to account for collective effects using the scattering parameter, α

$$S_e(x_e) = \frac{1}{\sqrt{\pi}} \cdot \frac{\exp\left(-x_e^2\right)}{\left|1+\alpha^2 W(x_e)\right|^2} \tag{5.6}$$

where x_e is a dimensionless parameter and $W(x_e)$ is the plasma dispersion function. The value of x_e is given by

$$x_e = \frac{c\lambda_0}{\sqrt{2}} \cdot \left(\frac{1}{\lambda} - \frac{1}{\lambda_0}\right) \cdot \left(\frac{2k_B T_e}{m_e}\right)^{-1/2} \tag{5.7}$$

where c is the speed of light in a vacuum. The complex plasma dispersion function is expressed as

$$W(x_e) = 1 - 2x_e e^{-x_e^2} \int_0^{x_e} e^{t^2} dt - j\sqrt{\pi} x_e e^{-x_e^2} \tag{5.8}$$

where t is a dummy variable and j is an imaginary unit. The spectral distribution function, given by Equation 5.6, takes on a unique shape based on the value of α (Appendix AII). A noticeable deviation from the Gaussian spectral shape becomes apparent for $\alpha \geq 0.2$, giving rise to a partially collective scattering regime. The distinct shape of the Thomson signal in the partially collective and collective scattering regimes allow for n_e and T_e to be determined without the absolute intensity calibration procedure. Rather, a shape calibration approach can be used, whereby α and T_e are used to adjust the shape and width of $S_e(x_e)$, respectively, to fit the unique shape of the Thomson signal (Appendix AII).

5.3.2 Fitting Procedure

In this work, the Raman signal was acquired in air with no discharge under known atmospheric conditions (i.e. pressure and temperature). The experimental Raman spectrum was fitted only considering rotational transitions N_2 and O_2, following the procedure described by Penney et al.[148], Van de Sande,[141] and van Gessel et al.[147] The rotational temperature (T_{rot}) and mole fractions of nitrogen (x_{N_2}) and oxygen (x_{O_2}) were used as the parameters to fit the Raman signal directly in order to obtain the system-specific $fLP_0\Delta\Omega$ calibration factor. The fitting procedure used for the absolute intensity and shape calibration of Thomson signal was adapted from the work of Obrusnik et al.[149] The calibration factor obtained from Raman scattering was used to rescale the simulated Thomson spectrum for the absolute calibration method, while the experimental Thomson signal was normalized for the shape calibration method. For both calibration approaches, a two-step procedure was implemented to fit the experimental Thomson signal using the MATLAB fminsearch and nlinfit functions following the procedure of van Gessel et. al.[147] While the fminsearch function shows good convergence when calculating the least square difference between the fitted and experimental curves, the algorithm does not provide error estimates for the fitted parameters. Conversely, the nlinfit function provides a covariant matrix that can be used for error analysis, but the convergence of the Levenberg-Marquardt nonlinear least squares algorithm is sensitive to the initial values of the fitting parameters. Thus, the fminsearch function was used to determine the initial fit values for α and T_e, which were used as inputs for the nlinfit function to provide error estimates.

5.3.3 Floating Potential Calculation

The floating potential of a collisional plasma can be correlated to the plasma parameters using an exponential-accuracy model under the assumption that the ion-atom collision frequency is independent of velocity and the ion mobility, μ_+, is constant.[150,151] The floating potential is given by

$$V_f = -\frac{2}{3}\frac{k_B T_e}{q_e}\ln\frac{\Delta}{\lambda_D} - 1.0082\frac{k_B T_e}{q_e} \tag{5.9}$$

where Δ is the ionization length. The ionization length can be written as

$$\Delta = \frac{n_e k_B T_e \mu_+}{j_+} \tag{5.10}$$

where j_+ is the ion current density. The ion current density can be approximated using the Child-Langmuir law given by[152]

$$j_+ = \frac{4}{9}\varepsilon_0 \left(\frac{2q_e}{M_+}\right) \frac{V^{3/2}}{d^2} \tag{5.11}$$

where M_+ is the ion mass, V is the voltage applied to the electrode, and d is the interelectrode spacing. The applied voltage, V, for each applied RF power was approximated using the root-mean-square of the measured peak voltages. Error analysis for the floating potential was carried out by propagating the error from the error estimates obtained from the Thomson fitted parameters. The error estimates were outputs along with the fitted parameters from the nlinfit function in Matlab. Specifically, Δn_e and ΔT_e were error estimates for the fitted parameters n_e and T_e, respectively. Propagation of the error estimates from the fitted parameters, the error in the floating potential expression given in Equation 5.9 yields

$$\Delta V_f = \sqrt{\left(-\frac{k_B T_e}{q_e n_e}\right)^2 \Delta n_e^{\,2} + \left[-\frac{2}{3}\frac{k_B}{q_e}\ln\left(\frac{\mu_+ n_e^{3/2} q_e}{j_+}\sqrt{\frac{k_B T_e}{\varepsilon_0}}\right) - \frac{1}{3}\frac{k_B}{q_e} - 1.0082\frac{k_B}{q_e}\right]^2 \Delta T_e^{\,2}} \tag{5.12}$$

5.4 Results & Discussion

5.4.1 Laser Light Scattering of Argon Plasma Jet

To understand the relationship between the measured reduction potential in solution, η_{PLI}, and the state variables of the plasma, the plasma parameters were first extracted from the laser light scattering signal. More specifically, the values of n_e and T_e were determined by calibrating and fitting the spectra obtained in the Thomson scattering experiments. Absolute intensity calibration was performed by means of fitting a Raman spectrum acquired in open air, shown in Figure 5.3. The experimental Raman signal was acquired over 10000 laser shots (17 min) at a height of 9 mm above the liquid surface. The fitted Raman spectrum (Figure 5.3) showed that T_{rot} = 295 K, which was in agreement with the measured ambient temperature. The mole fractions of nitrogen, $x_{N_2} = 0.805$, and oxygen, $x_{O_2} = 0.195$, obtained from the fit were consistent with the expected composition of ambient air under standard conditions. The experimental Raman signal was normalized in order to determine the system-specific $fLP_0\Delta\Omega$ factor required for absolute intensity calibration used in the Thomson scattering experiments.

The Thomson signal acquired for the Ar APPJ used in this work was found to fall within the partially collective scattering regime, as observed from the non-Gaussian profile shown in Fig. 5.4b. While absolute intensity calibration is not required for determining n_e and T_e in this scattering regime, it can be useful for comparing the results from shape calibration fitting. For the Thomson spectrum acquired for the Ar APPJ operating at 50 W (Fig. 5.4b), the fitted values for the electron density and temperature using the absolute intensity calibration method were found to $n_e = (7.16 \pm 0.33)\cdot10^{21}$ m^{-3} and $k_BT_e = 0.79 \pm 0.03$ eV, respectively. Similarly, the shape calibration method was applied to the same data set (Fig. 5.3c), which showed that the fitted values of $n_e = (7.16 \pm 0.28)\cdot10^{21}$ m^{-3} and $k_BT_e = 0.79 \pm 0.02$ eV. Note that Raman contribution to the Thomson signal was found to be negligible and omitted from the fit. The absence of Raman features in the Thomson signal is consistent with the idea that the amount of air entrainment into the flow would be negligible close to the tube ending of the APPJ. Given the close agreement between fitted values for the plasma parameters between both calibration methods, the reported plasma parameters reported herein were calculated based on the shape calibration method.

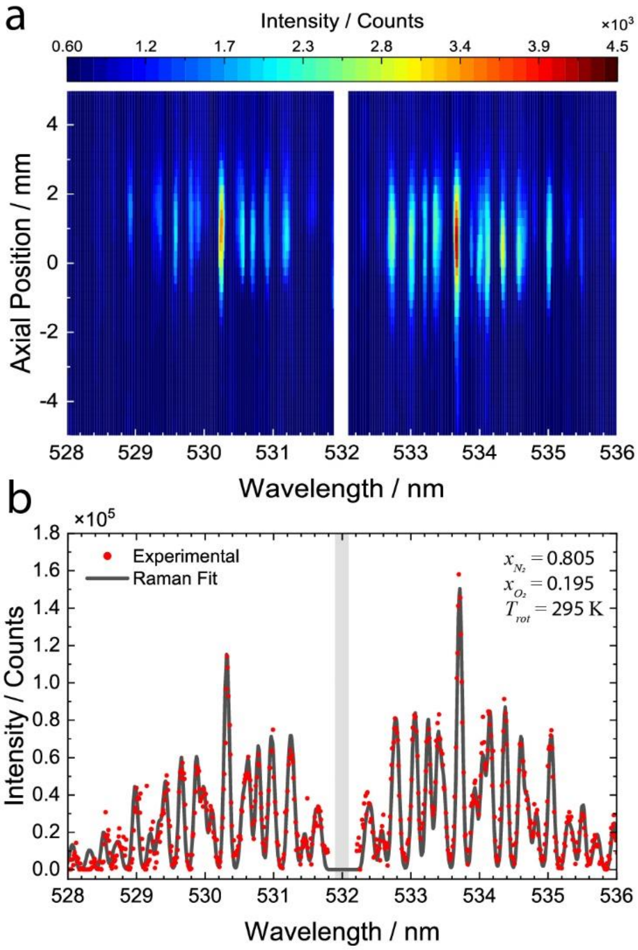

Figure 5.3. Rotational Raman Spectrum. (a) The iCCD image acquired for Raman scattering in open air under ambient conditions with no discharge present. (b) Experimental Raman spectrum generated from vertically binning data shown in (a) Fitted parameters are indicated on the top right. Grayed out areas are the Rayleigh rejection region. All spectra were acquired over an accumulation of 10000 laser shots.

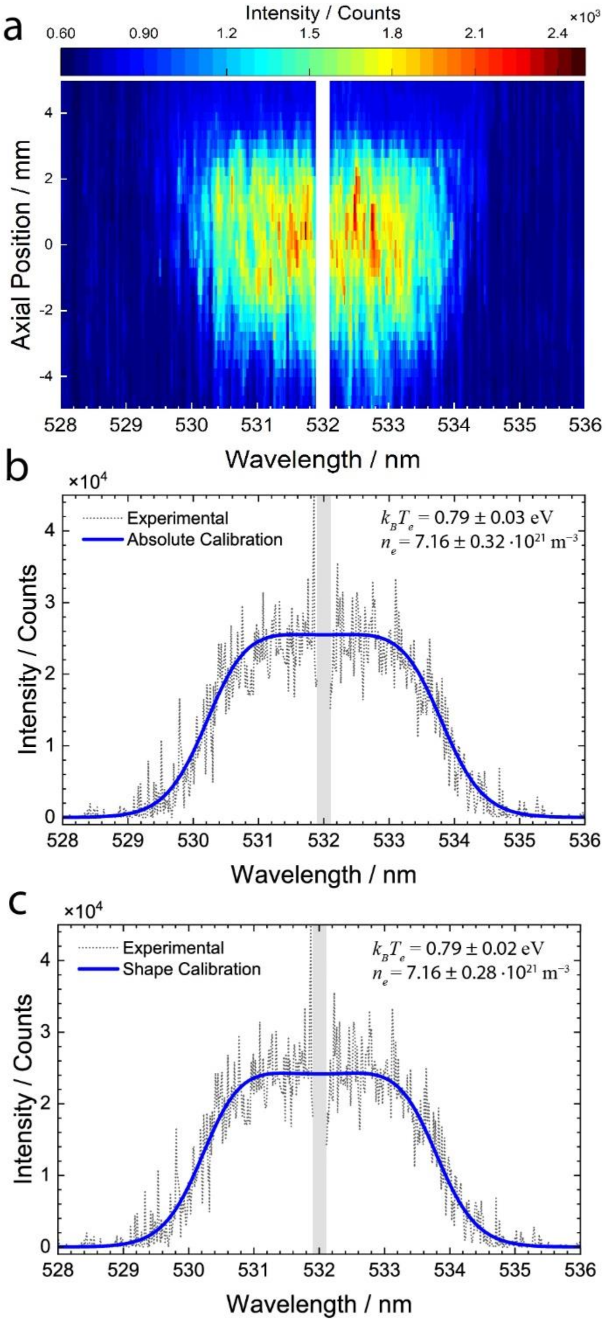

Figure 5.4. Thomson Scattering Spectrum. (a) The iCCD image acquired for Thomson scattering of Ar APPJ operating at 50 W. (b) Experimental Thomson spectrum fitted using the absolute intensity calibration method. (c) Same experimental Thomson spectrum from (b) with fitted spectrum based on shape calibration method. Both Thomson spectra in (b) and (c) were generated by vertically binning data from (a). Fitted parameters for each spectrum are indicated on the top right. Grayed out areas are the Rayleigh rejection region. All spectra were acquired over an accumulation of 10000 laser shots.

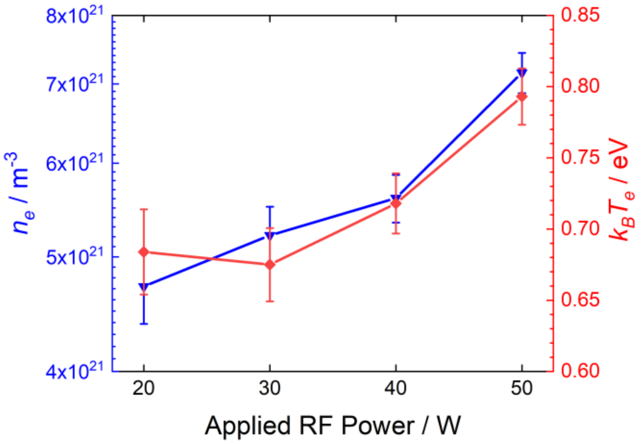

Figure 5.5. Electron density and electron temperature as a function of applied RF power. The electron density (blue triangles) and electron temperatures (red diamonds) determined from shape calibration fitting of the experimental laser Thomson signal as a function of applied RF power. Error bars are the error estimates of the Matlab nlinfit function.

The Thomson signal was acquired for the Ar APPJ as a function of applied RF power over the range of 20 to 50 W in increments of 10 W and the fitted plasma parameters are presented in graphical form in Figure. 5.5 and tabular form in Table 5.1. As shown in Figure 5.4, the error bars for the electron density and electron temperature overlap at lower RF powers. Whilet n_e and k_BT_e both appeared to increase with increasing applied power, the ability to delineate the individual effects that n_e and T_e have on the reduction potential on the liquid side of the plasma-liquid interface becomes difficult. A method is needed to describe the reduction potential in solution as a function of both of these plasma parameters. Given that electrochemical interfaces are typically described in terms of potential differences and charge densities, a more suitable framework for relating the plasma parameters to the reduction potential would be based on the potential and charge formation at the plasma-liquid interface.

Table 5.1. Summary of plasma parameters. Summarized results of the electron density and electron temperature as a function of applied RF power plotted in Figure. 5.5. The parameters were obtained using the shape calibration fitting method of the Thomson signal acquired at each RF power indicated. Error determined from the error estimates of the Matlab nlinfit function.

Applied RF Power / W	$k_B T_e$ / eV	n_e ($\cdot 10^{21}$) / m^{-3}
20	0.68 ± 0.03	4.72 ± 0.33
30	0.68 ± 0.03	5.21 ± 0.30
40	0.72 ± 0.02	5.61 ± 0.26
50	0.79 ± 0.02	7.16 ± 0.28

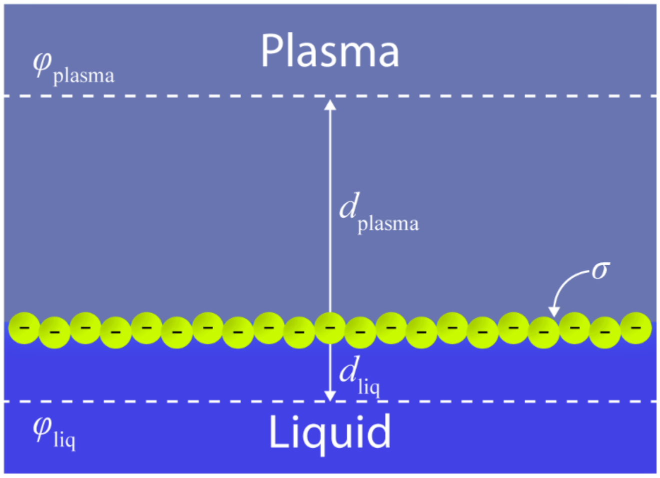

Figure 5.6. Schematic Representation of the charged plasma-liquid interface. Illustration depicting the areal charge density formed at the plasma-liquid interface and the unscreened potentials at characteristic lengths for each phase.

If the electrolyte solution is conceptualized to be a floating surface, a negative surface charge would be expected to form to balance the flux of the fast electrons and relatively slow positive ions to maintain quasi neutrality in the plasma. Approximating the plasma-liquid interface as an infinite sheet of charge with an areal charge density of σ, shown schematically in Figure 5.6, the potential in each phase can be correlated by

$$\sigma = \frac{\varphi_{\text{plasma}}}{d_{\text{plasma}}} = \frac{\varphi_{\text{liq}}}{d_{\text{liq}}} \tag{5.13}$$

where φ_i is the potential at a distance d_i from the plasma-liquid interface in phase i. As a positive charge is moved towards the plasma-liquid interface from a point infinitely far away, a potential difference between the unscreened test charge and interface arises as it approaches the surface. On the plasma side of the plasma-liquid interface, the distance in which screening occurs is the electron Debye length (i.e. $d_{\text{plasma}} = \lambda_D$) where the potential can be approximated as the floating potential ($\varphi_{\text{plasma}} = V_f$) of the plasma. A discussion of charge and potential formation of a floating surface in contact with a plasma is discussed in Appendix AIII. In the liquid, the distance in which screening occurs is given by the electrolyte Debye length ($d_{\text{liq}} = \ell_D$) which is given by

$$\ell_D = \left(\frac{\varepsilon_r \varepsilon_0 k_B T}{N_A q_e^2 \sum_i \left(c_i \cdot 10^3 \right) z_i^2} \right)^{1/2} \tag{5.14}$$

where ε_r is the relative permittivity, T is the temperature of the solution, N_A is the Avogadro constant, c_i is the molar concentration of ionic species i, and z_i is the charge number of ionic species i. Taking the unscreened potential in the liquid at a distance ℓ_D from the interface to be the relative reduction potential between the plasma-liquid interface and bulk solution, $\varphi_{\text{liq}} = \eta_{\text{PLI}}$, the potentials on both sides of the plasma-liquid interface can be equated by

$$\eta_{\text{PLI}} = V_f \cdot \frac{\ell_D}{\lambda_D}. \tag{5.15}$$

The plasma parameters determined from the Thomson scattering experiments were used as inputs for calculating the floating potential as a function of applied RF power using Equations 5.9-5.11.

The voltages used to calculate the ion current density were determined taking the root-mean-square of the peak voltages given in Figure 5.7.

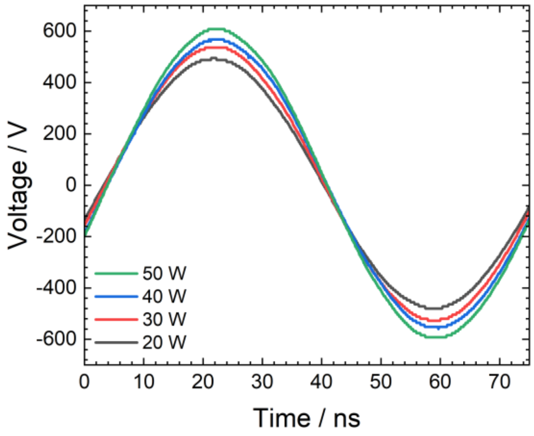

Figure 5.7. Voltage waveforms for various applied RF powers. The recorded voltage waveforms over a single RF cycle for the various RF powers used in the Thomson scattering experiments.

The ion mobility and mass used for argon were $1.54 \cdot 10^{-4}$ m^2 V^{-1} s^{-1} and $6.63 \cdot 10^{-26}$ kg, respectively.[153] The electrolyte Debye length was calculated using Equation 5.13 and found to be ℓ_D = 23.0 nm for the IC solution used in this work. Similarly, the electron Debye lengths were determined with Equation 5.3 for each electron density and electron temperature listed in Table 5.1, which ranged from λ_D = 89.5 nm to 79.3 nm as the applied RF power was increased from 20 to 50 W, respectively. The model predicted value for the relative reduction potential at the plasma-liquid interface, η, was found for each applied RF power using Equation 5.15. The results of the time-averaged electrochemical measurements and the model-predicted relative reduction potentials are plotted as a function of RF power as shown in Fig. 5.8b. The error bars for the experimentally measured relative reduction potential are the standard deviation from time-averaged electrochemical measurements, while the error bars for the modeled-predicted reduction potentials are propagated from the error estimates for the Thomson fit parameters.

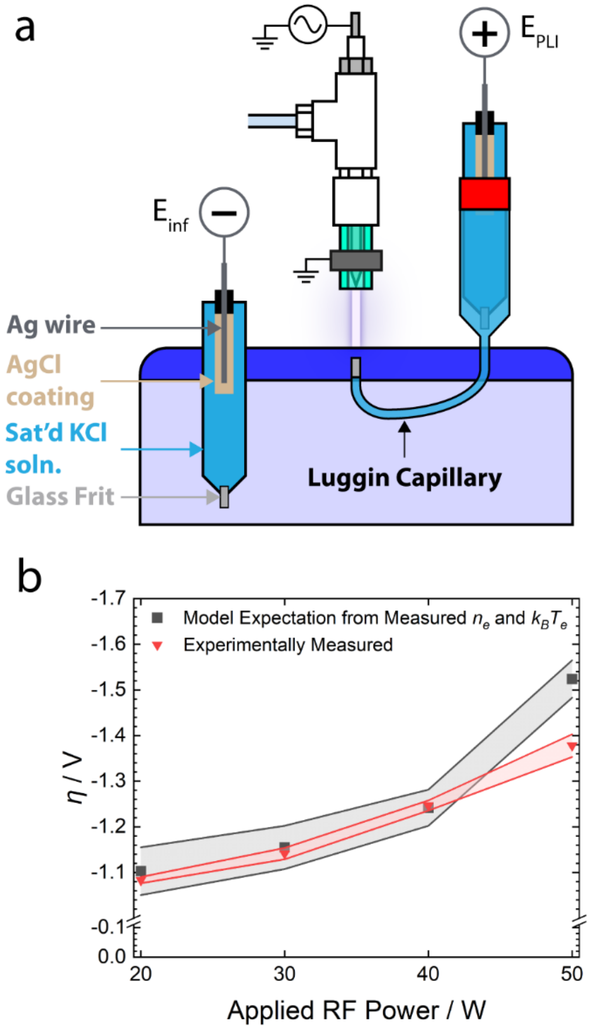

Figure 5.8. Experimentally measured reduction potential and model predicted potential as a function of RF power. (a) Schematic representation of Ar APPJ and Ag/AgCl reference electrode measuring local potential within the liquid near the plasma-liquid interface (E_{PLI}) with respect to an identical Ag/AgCl measuring potential in the bulk solution (E_{inf}). The E_{PLI} reference electrode was housed in a Luggin capillary which was positioned directly underneath the impingement point of the plasma jet. (b) Time-averaged relative reduction potential (red triangles) measured between the plasma-liquid interface and bulk solution. Error bars are the standard deviation. Model-predicted reduction potential (dark grey squares) based on floating potential calculated using experimental plasma parameters from laser Thomson scattering data in Table 5.1. Error bars are propagated error from the fitted parameters.

As shown in Fig. 5.8b, the model-predicted reduction potential was found to be in good agreement with the experimentally measured reduction potential. The error bars from the time-averaged reduction potential measurements overlap with the error bars propagated from the model-predicted reduction potential, except for the 50 W case. The disparity between the measured and model-predicted reduction potentials is likely due to simplifying assumptions of the model. In particular, the floating potential expression in Equation 5.8 is a first approximation that excludes higher order terms which could improve the accuracy.

Given that the selectivity of the Ar APPJ in contact with IC solution had not been tested, UV-Vis absorption spectroscopy was performed to verify that the Ar APPJ could perform selective reactions similar to the He APPJ. Using the same applied RF powers and duty cycle from the Thomson scattering experiments, the Ar APPJ was used to treat 20 mL volumes of IC solutions (pH 10) for 60 second durations. As shown in Figure 5.9, the selective reduction was still observed as indicated by the presence of the isosbestic points (Figure 5.9b).

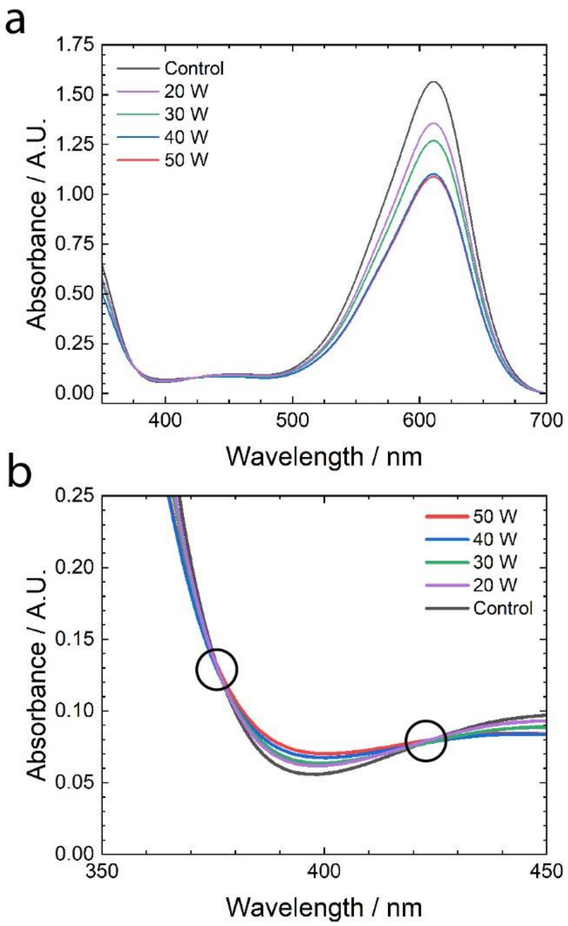

Figure 5.9. Ultraviolet-Visible Absorption Spectrum of Indigo Carmine. (a) UV-Vis absorption spectra of plasma treated IC solutions with an initial concentration of 75 μM and pH of 10 as a function of applied RF power. Plasma treatments were performed on 20 mL treatment volumes for a duration of 60 s. (b) Zoomed-in portion of absorption spectra shown in (a) to illustrate that the isosbestic points were preserved following plasma treatments using the Ar APPJ.

5.4.2 Model Verification using Helium Plasma Jet

As an independent means of validating the model, electrochemical measurements were performed in a sodium chloride (NaCl) solution as a function of NaCl concentration using an identical helium APPJ. The reduction potential was measured for different salt concentrations, and therefore different electrolyte Debye lengths ℓ_D, but the same plasma generation conditions were used (electrode geometry, applied RF power, and gas flow rate). Measurements of the relative reduction potential were measured for NaCl solutions with nominal concentrations of 0.2, 2, 20, and 200 mM. Solutions were freshly prepared using Type III ultrapure (18.2 MΩ cm) water from a Direct-Q 3 Water Purification System (MilliporeSigma). The plasma source used the same powered nickel needle electrode, but the tube used in this experiment was a fused silica tube with inner and outer diameters of 7 mm and 9.5 mm, respectively. The ground electrode was an aluminum ring with an inner diameter of 9.5 mm, which was mounted to the exterior of the silica tube at a distance of 5 mm from the tube outlet. The operating gas was helium, which was maintained at a constant flow rate of 2000 sccm. The RF power supply was run in continuous mode rather than a pulsed mode, using an applied RF power of 50 W. A schematic of the experimental apparatus used to characterize the He APPJ is shown in Figure 5.10a.

The floating potential was calculated Equations 5.9-11, where the dependence on ionic species arise from the M_+ and μ_+ terms which are $6.64 \cdot 10^{-26}$ kg and $10.7 \cdot 10^{-4}$ m^2 V^{-1} s^{-1}, respectively, in the case of helium.[153,154] Given that the helium APPJ was not characterized, the plasma parameters were set to be $n_e = 1 \cdot 10^{21}$ m^{-3} and $k_B T_e = 2.0$ eV for the floating potential calculation. In general, work comparing RF atmospheric helium and argon plasmas report lower electron densities and higher electron densities for the helium plasmas under similar operating conditions.[155] Based on the electron temperatures and electron densities obtained for the Ar APPJ from the Thomson scattering experiments, these estimates for the He APPJ plasma parameters are within reason. A plot of the model-predicted reduction values and the experimentally measured values for the reduction potential as a function of NaCl concentration are shown in Figure 5.10b.

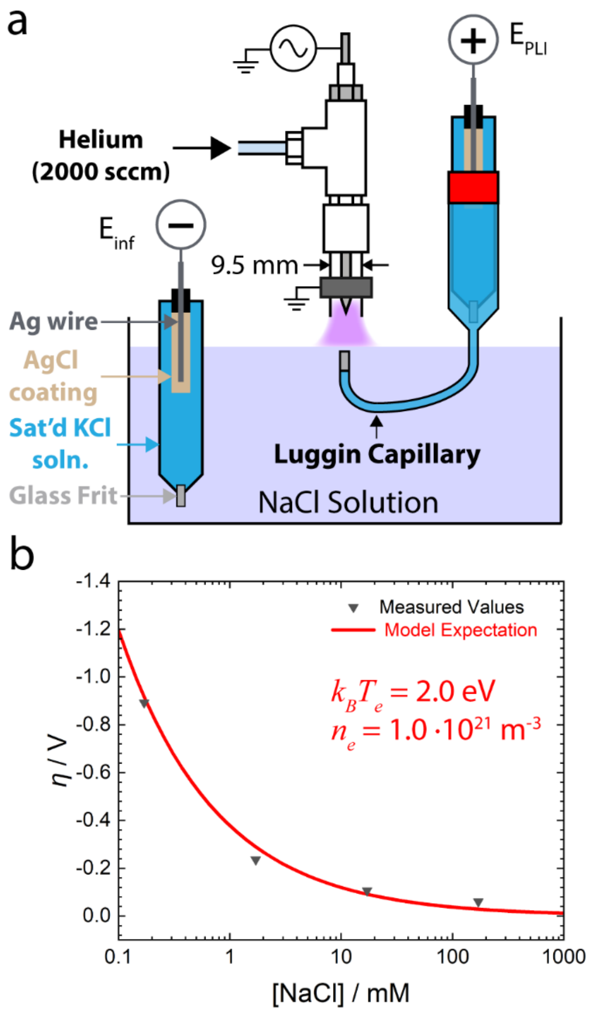

Figure 5.10. Effect of electrolyte Debye length on reduction potential. (a) Schematic representation helium APPJ and reference electrode, E_{PLI}, housed in a Luggin capillary used to measure local potential in the liquid near the plasma-liquid interface with respect to an identical reference electrode fixed in the bulk NaCl solution, E_{inf}. (b) The experimentally measured reduction potential (black triangles) for a helium APPJ in contact with a NaCl solution and the model-predicted reduction potential (red line) as a function of NaCl concentration. The plasma parameters assumed for the floating potential calculation were $k_B T_e = 2.0$ eV and $n_e = 1 \cdot 10^{21}$ m^{-3} as indicated.

5.5 Conclusions

Laser Thomson scattering was performed on an APPJ in contact with an electrolyte solution containing a model redox compound, measuring n_e and T_e as a function of RF power. Evaluation of the plasma parameters obtained from fitting the experimental Thomson signal using both absolute intensity calibration and shape calibration methods were in excellent agreement. Using a collision-dominated model for calculating the floating potential based on the experimentally measured plasma parameters, a simplistic model for predicting the reduction potential on the liquid side of the plasma-liquid interface was developed. Interestingly, the measured values of the reduction potential were found to be in close agreement with a scaled version of the plasma floating potential. In particular, the scaling factor was found to be the ratio of the electrolyte Debye length to the electron Debye length in the plasma. The ability to understand how the reduction potential at the plasma-liquid interface is related to the plasma parameters is a crucial first step in understanding how to perform controlled redox reactions. More specifically, this framework provides guidance on how to utilize plasma-liquid systems for promoting selective electrochemistry without the use of solid electrodes.

Chapter 6

Concluding Remarks

The purpose of this concluding chapter is to summarize the key findings from each chapter in this dissertation.

Chapter 2 introduced a technique for characterizing the reduction potential in solution based on the voltage difference measured between two identical, spatially separated, reference electrodes. Under the assumption that the solution is the largest resistance to current flow, the measured voltage difference will be equal to the differences in local reduction potentials between the two reference electrodes. Using electrochemical cells with known reduction potentials, the magnitude of the reference electrode measurement was consistent with the differences in reduction potentials between half-cells, while the sign was able to indicate whether reduction or oxidation was occuring.

Chapter 3 applied the reference electrode technique tested in Chapter 2 in order to characterize the reduction potential at a plasma-liquid interface. The relative reduction potential was measured by comparing the local potential directly underneath the plasma-liquid interface relative to the bulk solution. As the applied RF power used to generate the plasma increased, the relative reduction potential at the plasma-liquid interface became increasingly negative. The negative values suggested that reduction was taking place directly underneath the plasma-liquid interface. Using redox indicators to independently verify the electrical measurements, spectrophotometric methods verified that net reduction was occurring. The rate of reduction was found to increase with increasing RF power, which was consistent the observed trend in reduction potential.

Chapter 4 used spatial electrochemical measurements and multispectral imaging using colorimetric molecular indicators as two independent methods of identifying where redox half-reactions occur in electrodeless plasma-liquid configurations. Spatial electrochemical measurements revealed that the relative reduction potential was negative directly underneath the plasma and positive in the immediately surrounding solution, indicative of reduction and oxidation half-reactions, respectively. Visualization of the spatial distribution of redox indicators by multispectral imaging revealed that reduction products formed near the plasma jet centerline while oxidation byproducts concurrently formed further away in solution. The results of both experimental methods suggest that the electrodeless cathode is located directly underneath the plasma-liquid interface, while the electrodeless anode is surrounding in the adjacent solution.

Chapter 5 sought to identify a means of tuning the reduction potential in solution for an electrodeless electrochemical system. Analogous to using an external circuit used to modulate the potential at the electrode-electrolyte interface in conventional electrolytic cells, the plasma parameters (*e.g.* electron temperature and electron density) are hypothesized to control the potential at the plasma-liquid interface. Using a collision-dominated model for calculating the floating potential based on the experimentally measured plasma parameters, a simplistic model for predicting the reduction potential on the liquid side of the plasma-liquid interface was developed. Interestingly, the measured values of the reduction potential were found to be in close agreement with a scaled version of the plasma floating potential. In particular, the scaling factor was found to be the ratio of the electrolyte Debye length to the electron Debye length in the plasma.

Appendix I

Laser Heating

Laser heating of electrons in plasmas are known to occur as a result of inverse bremsstrahlung, where photons are absorbed by the plasma.[156,157] The threshold value for the laser fluence able to increase the electron temperature due to the absorption of energy from the incident laser has been worked out by Carbone et al.[158] in the case of a nonthermal argon (Ar) plasma. The critical value of the ionization degree for an argon plasma is given by

$$\alpha_{crit} = 3.4 \cdot 10^{-5} \left(k_B T_e\right)^{3/2} \left[1 + 6.4 \cdot \left(k_B T_e\right) + 14.2 \cdot \left(k_B T_e\right)^2\right] \tag{AI.1}$$

where k_B is the Boltzmann constant and T_e is the electron temperature. The rate coefficient for momentum transfer from electrons to ions is written as

$$K_{ei} = 2.54 \cdot 10^{-11} \left(\frac{1}{k_B T_e} \right)^{3/2} . \qquad \text{(AI.2)}$$

The number density of atoms, n_a, is expressed as

$$n_a = \frac{p}{k_B T_h} - n_e \qquad \text{(AI.3)}$$

where p is the pressure, T_h is the temperature of heavy particles, and n_e is the electron density. The maximum allowable relative increase in electron temperature is set by the experimentalist and can be written as

$$\xi = \frac{\Delta(k_B T_e)}{k_B T_e} . \qquad \text{(AI.4)}$$

Assuming quasi-neutrality ($n_e = n_i$), the critical laser fluence can be expressed as[158]

$$F_{crit} = 24\pi^4 \frac{m_e \varepsilon_0 c^3}{q_e^2} \cdot \frac{1}{\lambda_0} \cdot \xi \cdot \frac{k_B T_e}{n_e K_{ei}} \cdot \left[1 + \frac{n_a}{n_e} \alpha_{crit} \right]^{-1} \qquad \text{(AI.5)}$$

where m_e is the rest mass of an electron, ε_0 is the permittivity of free space, c is the speed of light in a vacuum, q_e is the fundamental charge, and λ_0 is the central laser wavelength. For $k_B T_e = 1.0$ eV, $n_e = 1.0 \cdot 10^{22}$ m^{-3}, and $\xi = 0.05$ the critical laser fluence was determined to be $F_{crit} = 135.1$ J cm^{-2}, which was greater than the operating laser fluence used in the experiments $F_{exp} = 75.6$ J cm^{-2}.

In addition to the theoretical calculation for the critical laser fluence for laser heating of electrons, the experimental values of $k_B T_e$ were obtained from Thomson scattering measurements over a range of laser fluences. Examples of the Thomson signal acquired for the radiofrequency (RF) Ar atmospheric pressure plasma jet (APPJ) operating at 50 W using a laser fluences of 44.1

J cm^{-2} (pulse energy of 35 mJ) and 226.6 J cm^{-2} (pulse energy of 180 mJ) are shown in Figures AI.1a and AI.1b, respectively. The laser spot size was 318 μm in diameter and the laser pulse energy was adjusted 35 to 180 mJ per pulse. A plot of the measured k_BT_e as function of laser fluence is shown in Figure AI.1c. The laser fluence (F_{exp}) used in the experiments is indicated by the dashed blue line. The operating laser fluence used in the Thomson and Raman scattering experiments was within the range in which the mean value of k_BT_e remained constant. Above the theoretical laser fluence (F_{crit}), the electron temperature begins to increase.

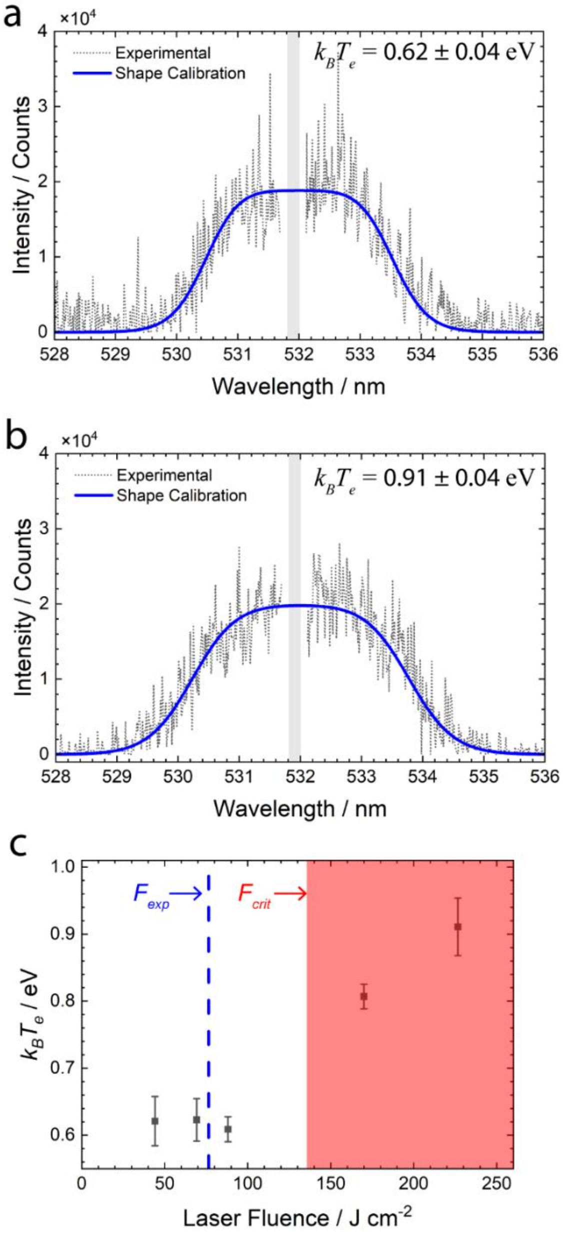

Figure AI.1. Electron temperature as a function of laser fluence. Thomson signal acquired for the Ar plasma (used in the Thomson scattering experiments in Chapter 5) generated using an applied RF power of 50 W using a laser fluence of (a) 44.1 J cm^{-2} (laser pulse energy of 35 mJ) and (b) 226.6 J cm^{-2} (laser pulse energy of 180 mJ). The grayed out region is the Rayleigh rejection region. (c) The measured values of k_BT_e as a function of laser fluence. Blue dashed line indicates the laser fluence used in the Thomson and Raman scattering experiments (F_{exp}) and shaded red area indicates the laser fluences at or above the critical value (F_{crit}) required for electron heating.

Appendix II

Effect of Scattering Parameter on Spectral Distribution Function

The degree of collectivity is determined by the scattering parameter α, given by

$$\alpha = \frac{1}{2\sqrt{2}\pi} \cdot \frac{\lambda_0}{\lambda_D} \tag{AII.1}$$

where λ_D is the electron Debye length of the plasma expressed as

$$\lambda_D = \left(\frac{\varepsilon_0 k_B T_e}{q_e^2 n_e} \right)^{1/2} . \tag{AII.2}$$

Note that the first term on the righthand side of Equation AII.1 only applies to light scattering systems in which the detection axis is orthogonal to the incident laser. In the collective Thomson scattering regime (*i.e.* $\lambda_0 \gg \lambda_D$), the incident laser light is scattered by an ensemble of electrons, resulting in anisotropic scattering of light. Due to the non-uniform scattering of light, interference effects distort the pure Gaussian profile of the spectral distribution function. The modification of the spectral distribution function can be written in terms of the scattering parameter α as

$$S_e(x_e) = \frac{1}{\sqrt{\pi}} \cdot \frac{\exp\left(-x_e^2\right)}{\left|1+\alpha^2 W(x_e)\right|^2} \tag{AII.3}$$

where x_e is a dimensionless parameter and $W(x_e)$ is the plasma dispersion function. The value of x_e is given by

$$x_e = \frac{c\lambda_0}{\sqrt{2}} \cdot \left(\frac{1}{\lambda} - \frac{1}{\lambda_0}\right) \cdot \left(\frac{2k_B T_e}{m_e}\right)^{-1/2} \tag{AII.4}$$

.

The complex plasma dispersion is expressed as

$$W(x_e) = 1 - 2x_e e^{-x_e^2} \int_0^{x_e} e^{t^2} dt - j\sqrt{\pi} x_e e^{-x_e^2} \tag{AII.5}$$

where t is a dummy variable and j is an imaginary unit. The principle of the shape calibration approach is illustrated in Figure AII.1. First, the α is used to adjust the shape of the spectral distribution function calculated using Equation AII.3 until it resembles the shape of the experimental Thomson signal. The influence of α on the shape of the spectral distribution function is shown in Figure AII.1a. Next, the width of S_e is adjusted by holding α constant and varying $k_B T_e$, until a suitable fit with the experimental Thomson spectrum is obtained. The influence of $k_B T_e$ on the width of the spectral distribution function, for constant α ($\alpha = 0.8$), is shown in Figure AII.1b. Once the unique values of α and $k_B T_e$ that accurate fit the Thomson signal are determined, the corresponding value of n_e is back-calculated by combining and rearranging Equations AII.1-2, yielding

$$n_e = \frac{\varepsilon_0 k_B T_e}{q_e^2} \left(\frac{1}{2\sqrt{2}\pi} \cdot \frac{\lambda_0}{\alpha} \right)^{-2} . \tag{AII.6}$$

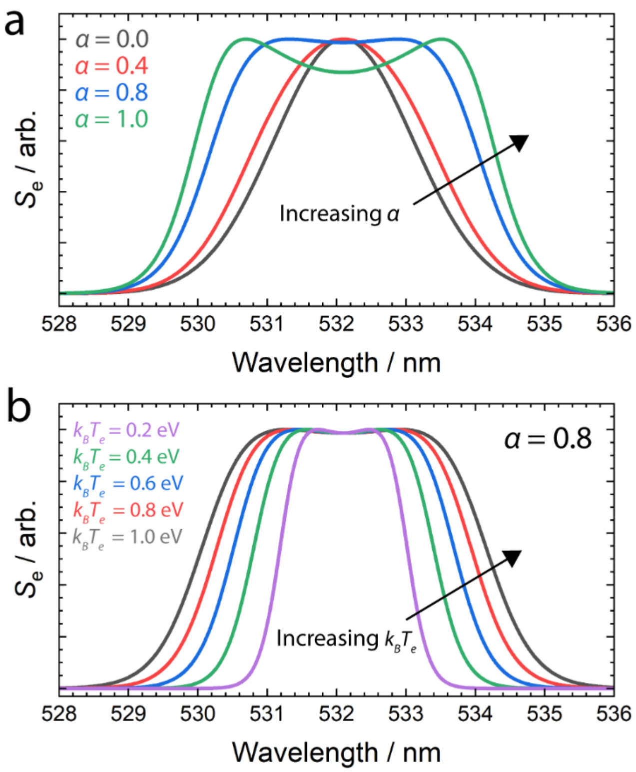

Figure AII.1. Effect of scattering parameter and electron temperature on spectral distribution function. (a) The normalized spectral distribution function, S_e, for different values of the scattering parameter, α. (b) The normalized spectral distribution function, S_e, for various electron temperatures, k_BT_e, at a constant $\alpha = 0.8$.

Appendix III

Charge and Potential Formation of Floating Surface in Contact with Nonthermal Plasma

Before describing the charging behavior of electrically isolated surfaces in contact with nonthermal plasmas, a brief outline of the simplifying assumptions regarding the plasma environment and the underlying assumptions will be covered. Consider an idealized nonthermal noble gas plasma (*e.g.* argon or helium) comprised of only free electrons, positive ions, and a background atomic gas. The mean electron temperature in a nonthermal plasma is typically on the order of $k_B T_e \geq 1.0$ eV while the ion and background gas temperatures are approximately equal to the ambient thermal energy of $k_B T_+ \approx k_B T_g \approx 0.0257$ eV, where k_B is the Boltzmann constant.[i,21] In order to simplify the discussion, the term ion will herein be used to refer to a singly charged positive ionic species from the plasma unless otherwise specified. The structure of a plasma can

---

[i] Plasma physicists tend to use energy units such as the electronvolt (eV) to describe characteristic temperatures. The equivalent values of these energies, in temperature units, correspond to $T_e \geq 11600$ K for electrons and $T_+ \approx T_g \approx 298$ K for ions and the background gas, respectively.

be divided into two distinct regions: the plasma bulk and the sheath. In the bulk region, quasi-neutrality holds, and the criterion required to maintain a macroscopically neutral plasma simplifies to

$$n_e = n_+ \tag{AIII.1}$$

where n_e and n_+ are the number densities of the electrons and ions, respectively. Within the bulk plasma, the velocities of electrons and ions are governed by their thermal motion. Assuming a Maxwellian energy distribution, the mean thermal velocity of electrons, $v_{e,\mathrm{th}}$ is

$$v_{e,\mathrm{th}} = \left(\frac{8k_B T_e}{\pi m_e}\right)^{1/2} \tag{AIII.2}$$

where m_e is the rest mass of an electron. In a similar manner, the mean thermal velocity of ions can be expressed as

$$v_{+,\mathrm{th}} = \left(\frac{8k_B T_+}{\pi M_+}\right)^{1/2} \tag{AIII.3}$$

where M_+ is the mass of the ion. It can be seen from Table AIII.1 that thermal velocities of electrons in the various bulk plasma are orders of magnitude higher than those of the ions.

Table AIII.1. Examples of various ion-to-electron mass ratios (M_+/m_e) and electron-to-ion thermal velocity ratios (v_e/v_+) for select ions. Values for mean thermal velocity based on k_BT_e = 1 eV.

Ion	M_+/m_e	v_e/v_+
H^+	1836.2	267.5
He^+	7296.2	533
Ar^+	72820.7	1684

In the case of a neutral, electrically isolated substrate that is brought into contact with a nonthermal plasma, the electrons and ions reach the uncharged substrate based on their thermal energies.[79,159,160] In general, the particle flux for electrons and ions can be expressed using[22,79,159,161]

$$\Gamma_{(e,+)} = n_{(e,+)} v_{(e,+)} \,. \tag{AIII.4}$$

where Γ is the flux of the charged particle, v is the mean velocity, and the subscripts e and + are used to denote electrons and ions, respectively. The initial flux of ions is based on the mean thermal velocity, $v_{+,\mathrm{th}}$, given by Equation AIII.3. Note that if one wants to consider the charging phenomena in terms of current, the electron and ion current densities can be expressed in terms of flux using

$$J_{(e,+)} = z_{(\mathrm{e},+)} q_e \Gamma_{(e,+)} \,. \tag{AIII.5}$$

where J is the current density of the charged particle, q_e is the fundamental charge, and z is the charge number of the species ($z_e = -1$ for an electron and $z_+ = +1$ for all ions in this discussion).[ii]

As a result of the initial imbalance of electron and ion fluxes, a region of net charge exists at the surface leaving behind a region of positive space charge in the boundary layer between the bulk plasma and substrate. The region of positive space charge is the plasma sheath, where the quasi-neutrality condition in Equation AIII.1 no longer applies and the electron density has a spatial dependence due to a potential barrier at the substrate surface. The fraction of electrons able to overcome the potential barrier can be approximated using a Boltzmann distribution as[22,161]

[ii] As another simplifying assumption, only currents generated by charged particles from the plasma are considered. Current generated by secondary electron emission and photoemission processes will be considered negligible.

$$n_e = n_0 \exp\left[-\frac{q_e \varphi(x)}{k_B T_e}\right] \qquad \text{(AIII.6)}$$

where n_0 is the bulk plasma density and φ is the electric potential at distance x from the substrate surface with respect to the plasma potential. Note that Equation AIII .6 simplifies to $n_e = n_0$ in the case where $\varphi(x)$ is equal to the plasma potential (*i.e.* as x approaches the plasma bulk). The velocity of the ions entering the sheath is given by the Bohm velocity as[22,161]

$$v_{+,\mathrm{B}} = \left(\frac{k_B T_e}{M_+}\right)^{1/2}. \qquad (1) \qquad \text{(AIII.7)}$$

A qualitative plot showing the profiles of the electric potential, electron and ion densities is shown in Figure AIII.1.

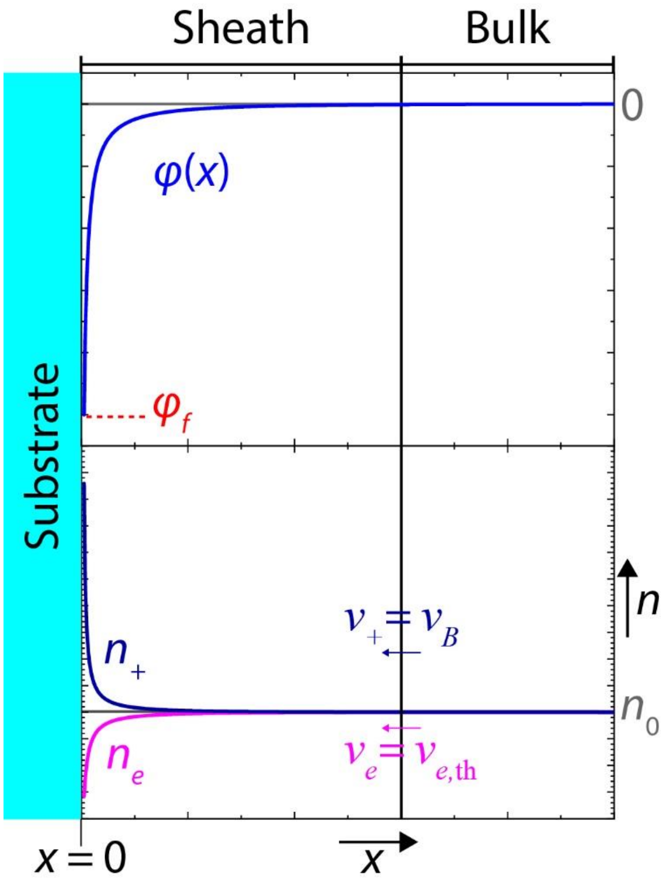

Figure AIII.1. Qualitative profiles of electric potential, electron density, and ion density. A qualitative sketch illustrating the potential profile on the top plot, with the electron (magenta) and ion (navy) densities profiles shown in the bottom plot for the sheath and bulk regions. Velocities of electrons (magenta) and ions (navy) entering the sheath shown at bulk/sheath boundary.

Due to the significantly lighter mass and higher thermal velocity of electrons, the thermal flux of electrons to the substrate is initially much greater than the thermal flux of ions ($\Gamma_e \gg \Gamma_+$) shown schematically in Figure AIII.2a. In the case of an initially uncharged substrate, the fluxes of electrons and ions are based on the bulk densities and thermal velocities. For electrons, the flux is given by

$$\Gamma_e = \frac{1}{4} n_0 \left(\frac{8 k_B T_e}{\pi m_e} \right)^{1/2} \tag{AIII.8}$$

while the thermal flux of ions is given by

$$\Gamma_{+} = \frac{1}{4} n_{0} \left(\frac{8 k_{B} T_{+}}{\pi M_{+}} \right)^{1/2} \tag{AIII.9}$$

where the first term accounts for directionality (*i.e.* flux normal to the direction of a plane).

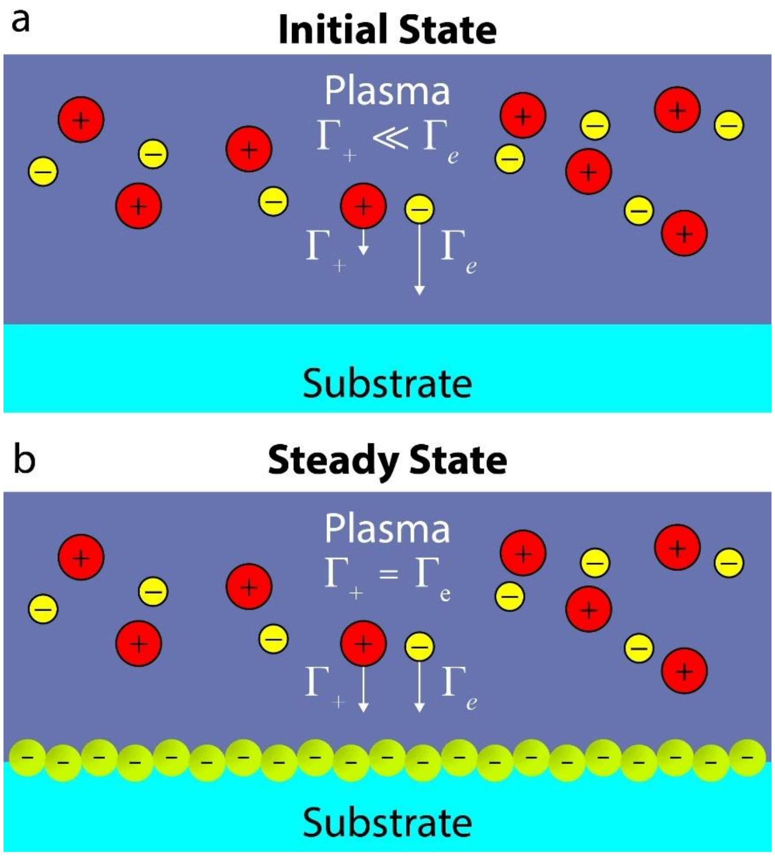

Figure AIII.2. Schematic of Electrically Isolated Substrate Exposed to Nonthermal Plasma. (a) Initial state of substrate exposed to plasma. The thermal flux of electrons is much greater than that of the ions. (b) Negatively charged substrate surface at steady state. Γ_e and Γ_+ are the fluxes of electrons and ions, respectively. The relative magnitudes of the fluxes are given by magnitudes of the white arrows (not to scale). Red circles represent positive ions, yellow circles represent electrons.

As a result, the electrons reach the substrate before the ions and create a negative charge on the substrate surface. A steady state is quickly reached as the negatively charged substrate surface creates a potential barrier that repels electrons with insufficient kinetic energies to reach the substrate while simultaneously attracting slow ions. For a dielectric substrate, the net current at the surface is zero at steady state, or equivalently, the fluxes of electrons and ions are equal ($\Gamma_e = \Gamma_+$) as shown schematically in Figure AIII.2b.[162] The flux of electrons to the surface is now modified by the number of electrons with sufficient kinetic energy to reach the surface and expressed by[22,79]

$$\Gamma_e = \frac{1}{4} n_0 \left(\frac{8 k_B T_e}{\pi m_e} \right)^{1/2} \exp\left(-\frac{q_e \varphi}{k_B T_e} \right) \tag{AIII.10}$$

while the flux of ions that reach the surface is the product of the ion density and the ion velocity for ions entering the plasma/sheath boundary, given by the Bohm flux as

$$\Gamma_+ = n_0 \left(\frac{k_B T_e}{M_+} \right)^{1/2} . \tag{AIII.11}$$

Setting Equations AIII.10 and AIII.11 equal to one another and solving for the electric potential term yields

$$\varphi_f = -\frac{k_B T}{2} \ln\left(\frac{M_+}{2\pi m_e} \right) . \tag{AIII.12}$$

Equation AIII.12 gives the expression for the floating potential, which is the potential value that a surface in contact with a plasma adopts in order to prevent any further accumulation of negative charge while maintaining a net current of zero.[163,164] The vast majority of electrons are repelled as only electrons with kinetic energies that exceed the potential barrier ($-q_e \varphi_f$) are able to reach the surface. The electron energy distribution function (EEDF) can be used to determine the probability of electrons with a particular energy. Based on a Maxwell-Boltzmann distribution function, the EEDF can be expressed as[21]

$$f\left(\varepsilon\right)=2\sqrt{\frac{\varepsilon}{\pi\left(k_BT_e\right)^3}}\exp\left(-\frac{\varepsilon}{k_BT}\right). \qquad \text{(AIII.13)}$$

where ε is the electron energy. A plot of the EEDF over electron energy range of 0 to 30 eV is shown in Figure AIII.3 to illustrate the electrons in the high energy tail with sufficient energies to reach the substrate surface.

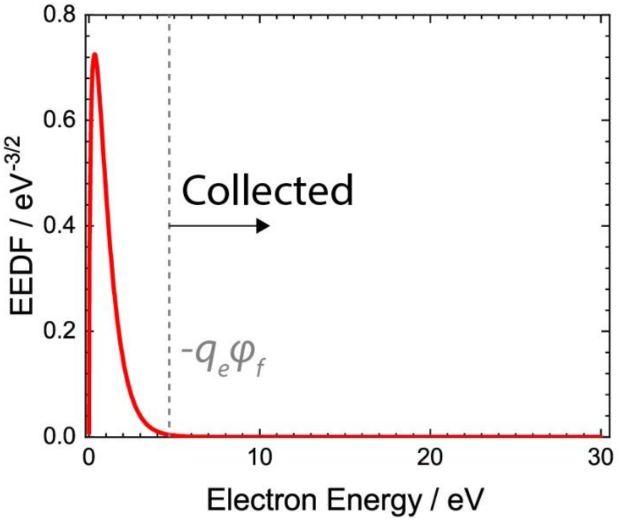

Figure AIII.3. Example of Maxwellian Electron Energy Distribution Function (EEDF) for a mean electron temperature of 1 eV. A plot of the electron energy distribution function (EEDF) for a Maxwellian distribution. Region to the left of dashed gray line to represents the electron energies that have insufficient energy to reach the substrate surface and are repelled into the plasma. Region to the right represents the electrons with enough kinetic energy to overcome potential barrier and reach substrate surface. Plot is based on a mean electron temperature of k_BT_e = 1 eV.

References

(1) Haegel, N. M.; Atwater, H.; Barnes, T.; Breyer, C.; Burrell, A.; Chiang, Y.-M.; Wolf, S. D.; Dimmler, B.; Feldman, D.; Glunz, S.; Goldschmidt, J. C.; Hochschild, D.; Inzunza, R.; Kaizuka, I.; Kroposki, B.; Kurtz, S.; Leu, S.; Margolis, R.; Matsubara, K.; Metz, A.; Metzger, W. K.; Morjaria, M.; Niki, S.; Nowak, S.; Peters, I. M.; Philipps, S.; Reindl, T.; Richter, A.; Rose, D.; Sakurai, K.; Schlatmann, R.; Shikano, M.; Sinke, W.; Sinton, R.; Stanbery, B. J.; Topic, M.; Tumas, W.; Ueda, Y.; Lagemaat, J. van de; Verlinden, P.; Vetter, M.; Warren, E.; Werner, M.; Yamaguchi, M.; Bett, A. W. Terawatt-Scale Photovoltaics: Transform Global Energy. *Science* **2019**, *364* (6443), 836–838. https://doi.org/10.1126/science.aaw1845.

(2) Solar Photovoltaic Cell/Module Shipments - Energy Information Administration https://www.eia.gov/renewable/annual/solar_photo/ (accessed 2021 -10 -01).

(3) Combellas, C.; Kanoufi, F.; Thiébault, A. Solutions of Solvated Electrons in Liquid Ammonia. *Journal of Electroanalytical Chemistry* **2001**, *499* (1), 144–151. https://doi.org/10.1016/S0022-0728(00)00504-0.

(4) Birch, A. J. Reduction by Dissolving Metals. Part I. *J. Chem. Soc.* **1944**, 430. https://doi.org/10.1039/jr9440000430.

(5) Wuts, P. G. M.; Gu, R. L.; Northuis, J. M.; Kwan, T. A.; Beck, D. M.; White, M. J. Development of a Practical Synthesis of Sumanirole. *Pure and Applied Chemistry* **2002**, *74* (8), 1359–1368. https://doi.org/10.1351/pac200274081359.

(6) Joshi, D. K.; Sutton, J. W.; Carver, S.; Blanchard, J. P. Experiences with Commercial Production Scale Operation of Dissolving Metal Reduction Using Lithium Metal and Liquid Ammonia. *Org. Process Res. Dev.* **2005**, *9* (6), 997–1002. https://doi.org/10.1021/op050155x.

(7) Nandi, P.; Redko, M. Y.; Petersen, K.; Dye, J. L.; Lefenfeld, M.; Vogt, P. F.; Jackson, J. E. Alkali Metals in Silica Gel (M-SG): A New Reagent for Desulfonation of Amines. *Org. Lett.* **2008**, *10* (23), 5441–5444. https://doi.org/10.1021/ol8021337.

(8) Costanzo, M. J.; Patel, M. N.; Petersen, K. A.; Vogt, P. F. Ammonia-Free Birch Reductions with Sodium Stabilized in Silica Gel, Na–SG(I). *Tetrahedron Letters* **2009**, *50* (39), 5463–5466. https://doi.org/10.1016/j.tetlet.2009.07.040.

(9) Peters, B. K.; Rodriguez, K. X.; Reisberg, S. H.; Beil, S. B.; Hickey, D. P.; Kawamata, Y.; Collins, M.; Starr, J.; Chen, L.; Udyavara, S.; Klunder, K.; Gorey, T. J.; Anderson, S. L.; Neurock, M.; Minteer, S. D.; Baran, P. S. Scalable and Safe Synthetic Organic Electroreduction Inspired by Li-Ion Battery Chemistry. *Science* **2019**, *363* (6429), 838–845. https://doi.org/10.1126/science.aav5606.

(10) Yang, X.; Kirsch, J.; Fergus, J.; Simonian, A. Modeling Analysis of Electrode Fouling during Electrolysis of Phenolic Compounds. *Electrochimica Acta* **2013**, *94*, 259–268. https://doi.org/10.1016/j.electacta.2013.01.019.

(11) Babai, M.; Gottesfeld, S. Ellipsometric Study of the Polymeric Surface Films Formed on Platinum Electrodes by the Electrooxidation of Phenolic Compounds. *Surface Science* **1980**, *96* (1), 461–475. https://doi.org/10.1016/0039-6028(80)90320-9.

(12) Panizza, M.; Cerisola, G. Direct And Mediated Anodic Oxidation of Organic Pollutants. *Chem. Rev.* **2009**, *109* (12), 6541–6569. https://doi.org/10.1021/cr9001319.

(13) Bard, A. J.; Faulkner, L. R. *Electrochemical Methods: Fundamentals and Applications*, 2nd ed.; Wiley: New York, 2001.

(14) Yang, C.; Magallanes, G.; Maldonado, S.; Stephenson, C. R. J. Electro-Reductive Fragmentation of Oxidized Lignin Models. *J. Org. Chem.* **2021**, acs.joc.1c00346. https://doi.org/10.1021/acs.joc.1c00346.

(15) Loff, S. Veil Nebula Supernova Remnant http://www.nasa.gov/image-feature/veil-nebula-supernova-remnant (accessed 2021 -10 -01).

(16) Winter in Svalbard https://www.arcticholiday.co.uk/galleries/tour-gallery-winter-in-svalbard/ (accessed 2021 -10 -01).

(17) Lightning Storm Over City Purple Light https://www.shutterstock.com/image-photo/lightning-storm-over-city-purple-light-281493026 (accessed 2021 -10 -01).

(18) Electric Propulsion at JPL - Multimedia https://sec353ext.jpl.nasa.gov/ep/multimedia.html (accessed 2021 -10 -01).

(19) Gallery of internal and plasma views https://alltheworldstokamaks.wordpress.com/gallery-of-internal-and-plasma-views/ (accessed 2021 -10 -01).

(20) Air Jordan 1 Neon Light (Chicago) | Limited Edition https://www.mkneon.com/products/air-jordan-1-neon-light-chicago (accessed 2021 -10 -01).

(21) Fridman, A. A. *Plasma Chemistry*; Cambridge University Press: Cambridge; New York, 2008.

(22) Lieberman, M. A.; Lichtenberg, A. J. *Principles of Plasma Discharges and Materials Processing*; Wiley-Interscience: Hoboken, N.J., 2005.

(23) Selwyn, G. S.; Herrmann, H. W.; Park, J.; Henins, I. Materials Processing Using an Atmospheric Pressure, RF-Generated Plasma Source. *Contributions to Plasma Physics* **2001**, *41* (6), 610–619. https://doi.org/10.1002/1521-3986(200111)41:6<610::AID-CTPP610>3.0.CO;2-L.

(24) Dakin, J. T. Nonequilibrium Lighting Plasmas. *IEEE Trans. Plasma Sci.* **1991**, *19* (6), 991–1002. https://doi.org/10.1109/27.125026.

(25) Kortshagen, U. Nonthermal Plasma Synthesis of Nanocrystals: Fundamentals, Applications, and Future Research Needs. *Plasma Chem Plasma Process* **2016**, *36* (1), 73–84. https://doi.org/10.1007/s11090-015-9663-4.

(26) Abedin, S. Z. E.; Pölleth, M.; Meiss, S. A.; Janek, J.; Endres, F. Ionic Liquids as Green Electrolytes for the Electrodeposition of Nanomaterials. *Green Chem.* **2007**, *9* (6), 549–553. https://doi.org/10.1039/B614520E.

(27) Goossens, O.; Dekempeneer, E.; Vangeneugden, D.; Van de Leest, R.; Leys, C. Application of Atmospheric Pressure Dielectric Barrier Discharges in Deposition, Cleaning and Activation. *Surf. Coat. Technol.* **2001**, *142–144*, 474–481. https://doi.org/10.1016/S0257-8972(01)01140-9.

(28) Yi, C. H.; Lee, Y. H.; Yeom, G. Y. The Study of Atmospheric Pressure Plasma for Surface Cleaning. *Surf. Coat. Technol.* **2003**, *171* (1), 237–240. https://doi.org/10.1016/S0257-8972(03)00278-0.

(29) Lee, Y.-H.; Yi, C.-H.; Chung, M.-J.; Yeom, G.-Y. Characteristics of He/O2 Atmospheric Pressure Glow Discharge and Its Dry Etching Properties of Organic Materials. *Surf. Coat. Technol.* **2001**, *146–147*, 474–479. https://doi.org/10.1016/S0257-8972(01)01459-1.

(30) Paetzelt, H.; Böhm, G.; Arnold, T. Etching of Silicon Surfaces Using Atmospheric Plasma Jets. *Plasma Sources Sci. Technol.* **2015**, *24* (2), 025002. https://doi.org/10.1088/0963-0252/24/2/025002.

(31) Williams, T. S.; Yu, H.; Yeh, P.-C.; Yang, J.-M.; Hicks, R. F. Atmospheric Pressure Plasma Effects on the Adhesive Bonding Properties of Stainless Steel and Epoxy Composites. *J. Compos. Mater.* **2014**, *48* (2), 219–233. https://doi.org/10.1177/0021998312470150.

(32) Oldham, T.; Simon, K.; Ferriell, D. R.; Belcher, M. A.; Rubin, A.; Thimsen, E. Highly Uniform Activation of Carbon Fiber Reinforced Thermoplastics by Low-Temperature Plasma. *ACS Appl. Polym. Mater.* **2019**, *1* (10), 2638–2648. https://doi.org/10.1021/acsapm.9b00532.

(33) Shekhter, A. B.; Kabisov, R. K.; Pekshev, A. V.; Kozlov, N. P.; Perov, Yu. L. Experimental and Clinical Validation of Plasmadynamic Therapy of Wounds with Nitric Oxide. *Bull. Exp. Biol. Med.* **1998**, *126* (2), 829–834. https://doi.org/10.1007/BF02446923.

(34) Graves, D. B. The Emerging Role of Reactive Oxygen and Nitrogen Species in Redox Biology and Some Implications for Plasma Applications to Medicine and Biology. *J. Phys. D: Appl. Phys.* **2012**, *45* (26), 263001. https://doi.org/10.1088/0022-3727/45/26/263001.

(35) Graves, D. B. Low Temperature Plasma Biomedicine: A Tutorial Review. *Phys. Plasmas* **2014**, *21* (8), 080901. https://doi.org/10.1063/1.4892534.

(36) Foster, J.; Sommers, B. S.; Gucker, S. N.; Blankson, I. M.; Adamovsky, G. Perspectives on the Interaction of Plasmas With Liquid Water for Water Purification. *IEEE Trans. Plasma Sci.* **2012**, *40* (5), 1311–1323. https://doi.org/10.1109/TPS.2011.2180028.

(37) Hijosa-Valsero, M.; Molina, R.; Schikora, H.; Müller, M.; Bayona, J. M. Removal of Priority Pollutants from Water by Means of Dielectric Barrier Discharge Atmospheric Plasma. *J. Hazard. Mater.* **2013**, *262*, 664–673. https://doi.org/10.1016/j.jhazmat.2013.09.022.

(38) Jiang, B.; Zheng, J.; Qiu, S.; Wu, M.; Zhang, Q.; Yan, Z.; Xue, Q. Review on Electrical Discharge Plasma Technology for Wastewater Remediation. *Chem. Eng. J.* **2014**, *236*, 348–368. https://doi.org/10.1016/j.cej.2013.09.090.

(39) Grinevich, V. I.; Kvitkova, E. Y.; Plastinina, N. A.; Rybkin, V. V. Application of Dielectric Barrier Discharge for Waste Water Purification. *Plasma Chem. Plasma Process.* **2011**, *31* (4), 573–583. https://doi.org/10.1007/s11090-010-9256-1.

(40) Richmonds, C.; Sankaran, R. M. Plasma-Liquid Electrochemistry: Rapid Synthesis of Colloidal Metal Nanoparticles by Microplasma Reduction of Aqueous Cations. *Appl. Phys. Lett.* **2008**, *93* (13), 131501. https://doi.org/10.1063/1.2988283.

(41) Baba, K.; Kaneko, T.; Hatakeyama, R. Efficient Synthesis of Gold Nanoparticles Using Ion Irradiation in Gas–Liquid Interfacial Plasmas. *Appl. Phys. Express* **2009**, *2* (3), 035006. https://doi.org/10.1143/APEX.2.035006.

(42) Chen, Q.; Li, J.; Li, Y. A Review of Plasma–Liquid Interactions for Nanomaterial Synthesis. *J. Phys. D: Appl. Phys.* **2015**, *48* (42), 424005. https://doi.org/10.1088/0022-3727/48/42/424005.

(43) Mariotti, D.; Belmonte, T.; Benedikt, J.; Velusamy, T.; Jain, G.; Švrček, V. Low-Temperature Atmospheric Pressure Plasma Processes for “Green” Third Generation

Photovoltaics. *Plasma Process Polym.* **2016**, *13* (1), 70–90. https://doi.org/10.1002/ppap.201500187.

(44) Laroussi, M.; Leipold, F. Evaluation of the Roles of Reactive Species, Heat, and UV Radiation in the Inactivation of Bacterial Cells by Air Plasmas at Atmospheric Pressure. *International Journal of Mass Spectrometry* **2004**, *233* (1–3), 81–86. https://doi.org/10.1016/j.ijms.2003.11.016.

(45) Burlica, R.; Kirkpatrick, M. J.; Locke, B. R. Formation of Reactive Species in Gliding Arc Discharges with Liquid Water. *Journal of Electrostatics* **2006**, *64* (1), 35–43. https://doi.org/10.1016/j.elstat.2004.12.007.

(46) Lukes, P.; Dolezalova, E.; Sisrova, I.; Clupek, M. Aqueous-Phase Chemistry and Bactericidal Effects from an Air Discharge Plasma in Contact with Water: Evidence for the Formation of Peroxynitrite through a Pseudo-Second-Order Post-Discharge Reaction of H2O2and HNO2. *Plasma Sources Sci. Technol.* **2014**, *23* (1), 015019. https://doi.org/10.1088/0963-0252/23/1/015019.

(47) Rumbach, P.; Bartels, D. M.; Sankaran, R. M.; Go, D. B. The Effect of Air on Solvated Electron Chemistry at a Plasma/Liquid Interface. *J. Phys. D: Appl. Phys.* **2015**, *48* (42), 424001. https://doi.org/10.1088/0022-3727/48/42/424001.

(48) Rumbach, P.; Bartels, D. M.; Sankaran, R. M.; Go, D. B. The Solvation of Electrons by an Atmospheric-Pressure Plasma. *Nat Commun* **2015**, *6* (1), 7248. https://doi.org/10.1038/ncomms8248.

(49) Kondeti, V. S. S. K.; Gangal, U.; Yatom, S.; Bruggeman, P. J. Ag+ Reduction and Silver Nanoparticle Synthesis at the Plasma–Liquid Interface by an RF Driven Atmospheric Pressure Plasma Jet: Mechanisms and the Effect of Surfactant. *Journal of Vacuum Science & Technology A* **2017**, *35* (6), 061302. https://doi.org/10.1116/1.4995374.

(50) Richmonds, C.; Witzke, M.; Bartling, B.; Lee, S. W.; Wainright, J.; Liu, C.-C.; Sankaran, R. M. Electron-Transfer Reactions at the Plasma–Liquid Interface. *J. Am. Chem. Soc.* **2011**, *133* (44), 17582–17585. https://doi.org/10.1021/ja207547b.

(51) D. K. Joshi, *; J. W. Sutton, †; S. Carver, † and; Blanchard‡, J. P. Experiences with Commercial Production Scale Operation of Dissolving Metal Reduction Using Lithium Metal and Liquid Ammonia http://pubs.acs.org/doi/full/10.1021/op050155x (accessed 2021 -01 -15). https://doi.org/10.1021/op050155x.

(52) Forstmann, F.; Díaz-Herrera, E.; Juaristi, E. The Fermi Level in Electrolytes—about Electrochemical Potentials at Electrolyte-Electrode Interfaces. In *AIP Conference Proceedings*; AIP: México City (México), 2008; Vol. 979, pp 181–194. https://doi.org/10.1063/1.2901841.

(53) Dill, K. A.; Bromberg, S. *Molecular Driving Forces: Statistical Thermodynamics in Biology, Chemistry, Physics, and Nanoscience*, 2nd ed.; Garland Science: London ; New York, 2011.

(54) Boettcher, S. W.; Oener, S. Z.; Lonergan, M. C.; Surendranath, Y.; Ardo, S.; Brozek, C.; Kempler, P. A. Potentially Confusing: Potentials in Electrochemistry. *ACS Energy Lett.* **2021**, *6* (1), 261–266. https://doi.org/10.1021/acsenergylett.0c02443.

(55) Gerischer, H.; Ekardt, W. Fermi Levels in Electrolytes and the Absolute Scale of Redox Potentials. *Appl. Phys. Lett.* **1983**, *43* (4), 393–395. https://doi.org/10.1063/1.94356.

(56) Bockris, J. O.; Khan, S. U. M. Fermi Levels in Solution. *Appl. Phys. Lett.* **1983**, *42* (1), 124–125. https://doi.org/10.1063/1.93745.

(57) Rumbach, P.; Witzke, M.; Sankaran, R. M.; Go, D. B. Decoupling Interfacial Reactions between Plasmas and Liquids: Charge Transfer vs Plasma Neutral Reactions. *J. Am. Chem. Soc.* **2013**, *135* (44), 16264–16267. https://doi.org/10.1021/ja407149y.

(58) Rumbach, P.; Xu, R.; Go, D. B. Electrochemical Production of Oxalate and Formate from CO2 by Solvated Electrons Produced Using an Atmospheric-Pressure Plasma. *J. Electrochem. Soc.* **2016**, *163* (10), F1157. https://doi.org/10.1149/2.0521610jes.

(59) Mota-Lima, A. The Electrified Plasma/Liquid Interface as a Platform for Highly Efficient CO2 Electroreduction to Oxalate. *J. Phys. Chem. C* **2020**, *124* (20), 10907–10915. https://doi.org/10.1021/acs.jpcc.0c00099.

(60) Chen, H.; Yuan, D.; Wu, A.; Lin, X.; Li, X. Review of Low-Temperature Plasma Nitrogen Fixation Technology. *Waste Dispos. Sustain. Energy* **2021**, *3* (3), 201–217. https://doi.org/10.1007/s42768-021-00074-z.

(61) Mehta, P.; Barboun, P.; Herrera, F. A.; Kim, J.; Rumbach, P.; Go, D. B.; Hicks, J. C.; Schneider, W. F. Overcoming Ammonia Synthesis Scaling Relations with Plasma-Enabled Catalysis. *Nat Catal* **2018**, *1* (4), 269–275. https://doi.org/10.1038/s41929-018-0045-1.

(62) Wang, S.; Lu, A.; Zhong, C.-J. Hydrogen Production from Water Electrolysis: Role of Catalysts. *Nano Convergence* **2021**, *8* (1), 4. https://doi.org/10.1186/s40580-021-00254-x.

(63) Rumbach, P.; Bartels, D. M.; Sankaran, R. M.; Go, D. B. The Solvation of Electrons by an Atmospheric-Pressure Plasma. *Nat Commun* **2015**, *6* (1), 1–7. https://doi.org/10.1038/ncomms8248.

(64) Kaneko, T.; Baba, K.; Harada, T.; Hatakeyama, R. Novel Gas-Liquid Interfacial Plasmas for Synthesis of Metal Nanoparticles. *Plasma Processes and Polymers* **2009**, *6* (11), 713–718. https://doi.org/10.1002/ppap.200900029.

(65) Höfft, O.; Endres, F. Plasma Electrochemistry in Ionic Liquids: An Alternative Route to Generate Nanoparticles. *Phys. Chem. Chem. Phys.* **2011**, *13* (30), 13472–13478. https://doi.org/10.1039/C1CP20501C.

(66) Ghosh, S.; Hawtof, R.; Rumbach, P.; Go, D. B.; Akolkar, R.; Sankaran, R. M. Quantitative Study of Electrochemical Reduction of Ag+ to Ag Nanoparticles in Aqueous Solutions by a Plasma Cathode. *J. Electrochem. Soc.* **2017**, *164* (13), D818–D824. https://doi.org/10.1149/2.0541713jes.

(67) Naitali, M.; Kamgang-Youbi, G.; Herry, J.-M.; Bellon-Fontaine, M.-N.; Brisset, J.-L. Combined Effects of Long-Living Chemical Species during Microbial Inactivation Using Atmospheric Plasma-Treated Water. *Appl. Environ. Microbiol.* **2010**, *76* (22), 7662–7664. https://doi.org/10.1128/AEM.01615-10.

(68) Ma, R.; Wang, G.; Tian, Y.; Wang, K.; Zhang, J.; Fang, J. Non-Thermal Plasma-Activated Water Inactivation of Food-Borne Pathogen on Fresh Produce. *Journal of Hazardous Materials* **2015**, *300*, 643–651. https://doi.org/10.1016/j.jhazmat.2015.07.061.

(69) Volkov, A. G.; Bookal, A.; Hairston, J. S.; Roberts, J.; Taengwa, G.; Patel, D. Mechanisms of Multielectron Reactions at the Plasma/Water Interface: Interfacial Catalysis, RONS, Nitrogen Fixation, and Plasma Activated Water. *Electrochimica Acta* **2021**, *385*, 138441. https://doi.org/10.1016/j.electacta.2021.138441.

(70) Miyahara, T.; Oizumi, M.; Nakatani, T.; Sato, T. Effect of Voltage Polarity on Oxidation-Reduction Potential by Plasma in Water. *AIP Advances* **2014**, *4* (4), 047115. https://doi.org/10.1063/1.4871475.

(71) Nordstrom, D. K.; Wilde, F. D. *Chapter A6. Section 6.5. Reduction-Oxidation Potential (Electrode Method)*, Version 1.2.; Techniques of Water-Resources Investigations; Report 09-A6.5; Reston, VA, 2005. https://doi.org/10.3133/twri09A6.5.

(72) Cartier, C. A.; Kumsa, D.; Feng, Z.; Zhu, H.; Scherson, D. A. Quantitative Aspects of Ohmic Microscopy. *Anal. Chem.* **2012**, *84* (16), 7080–7084. https://doi.org/10.1021/ac301361w.

(73) Bastos, A. C.; Quevedo, M. C.; Karavai, O. V.; Ferreira, M. G. S. Review—On the Application of the Scanning Vibrating Electrode Technique (SVET) to Corrosion Research. *J. Electrochem. Soc.* **2017**, *164* (14), C973–C990. https://doi.org/10.1149/2.0431714jes.

(74) Isaacs, H.; Vyas, B. Scanning Reference Electrode Techniques in Localized Corrosion. In *Electrochemical Corrosion Testing*; Mansfeld, F., Bertocci, U., Eds.; ASTM International: 100 Barr Harbor Drive, PO Box C700, West Conshohocken, PA 19428-2959, 1981; pp 3-3–31. https://doi.org/10.1520/STP28024S.

(75) Rosenfeld, I. L.; Danilov, I. S. Electrochemical Aspects of Pitting Corrosion. *Corrosion Science* **1967**, *7* (3), 129–142. https://doi.org/10.1016/S0010-938X(67)80073-8.

(76) Voruganti, V. S.; Luft, H. B.; DeGeer, D.; Bradford, S. A. Scanning Reference Electrode Technique for the Investigation of Preferential Corrosion of Weldments in Offshore Applications. *CORROSION* **1991**, *47* (5), 343–351. https://doi.org/10.5006/1.3585264.

(77) Griffiths, D. J. *Introduction to Electrodynamics*, Fourth edition.; Cambridge University Press: Cambridge, United Kingdom ; New York, NY, 2018.

(78) Bigalke, J.; Grabner, E. W. The Geobattery Model: A Contribution to Large Scale Electrochemistry. *Electrochimica Acta* **1997**, *42* (23–24), 3443–3452. https://doi.org/10.1016/S0013-4686(97)00053-4.

(79) Raĭzer, I. P. *Gas Discharge Physics*; Springer: Berlin; New York, 1997.

(80) Laimer, J.; Störi, H. Glow Discharges Observed in Capacitive Radio-Frequency Atmospheric-Pressure Plasma Jets. *Plasma Processes and Polymers* **2006**, *3* (8), 573–586. https://doi.org/10.1002/ppap.200600046.

(81) Sato, M.; Ohgiyama, T.; Clements, J. S. Formation of Chemical Species and Their Effects on Microorganisms Using a Pulsed High-Voltage Discharge in Water. *IEEE Transactions on Industry Applications* **1996**, *32* (1), 106–112. https://doi.org/10.1109/28.485820.

(82) Fridman, G.; Friedman, G.; Gutsol, A.; Shekhter, A. B.; Vasilets, V. N.; Fridman, A. Applied Plasma Medicine. *Plasma Processes and Polymers* **2008**, *5* (6), 503–533. https://doi.org/10.1002/ppap.200700154.

(83) Bauer, G.; Graves, D. B. Mechanisms of Selective Antitumor Action of Cold Atmospheric Plasma-Derived Reactive Oxygen and Nitrogen Species. *Plasma Processes and Polymers* **2016**, *13* (12), 1157–1178. https://doi.org/10.1002/ppap.201600089.

(84) Gjika, E.; Pal-Ghosh, S.; Tang, A.; Kirschner, M.; Tadvalkar, G.; Canady, J.; Stepp, M. A.; Keidar, M. Adaptation of Operational Parameters of Cold Atmospheric Plasma for in Vitro Treatment of Cancer Cells. *ACS Appl. Mater. Interfaces* **2018**, *10* (11), 9269–9279. https://doi.org/10.1021/acsami.7b18653.

(85) Kitazaki, S.; Koga, K.; Shiratani, M.; Hayashi, N. Growth Enhancement of Radish Sprouts Induced by Low Pressure O2 Radio Frequency Discharge Plasma Irradiation. *Jpn. J. Appl. Phys.* **2012**, *51* (1S), 01AE01. https://doi.org/10.1143/JJAP.51.01AE01.

(86) Min, S. C.; Roh, S. H.; Niemira, B. A.; Sites, J. E.; Boyd, G.; Lacombe, A. Dielectric Barrier Discharge Atmospheric Cold Plasma Inhibits Escherichia Coli O157:H7,

Salmonella, Listeria Monocytogenes, and Tulane Virus in Romaine Lettuce. *International Journal of Food Microbiology* **2016**, *237*, 114–120. https://doi.org/10.1016/j.ijfoodmicro.2016.08.025.

(87) Mariotti, D.; Patel, J.; Švrček, V.; Maguire, P. Plasma–Liquid Interactions at Atmospheric Pressure for Nanomaterials Synthesis and Surface Engineering. *Plasma Processes and Polymers* **2012**, *9* (11–12), 1074–1085. https://doi.org/10.1002/ppap.201200007.

(88) Lu, X.; Naidis, G. V.; Laroussi, M.; Reuter, S.; Graves, D. B.; Ostrikov, K. Reactive Species in Non-Equilibrium Atmospheric-Pressure Plasmas: Generation, Transport, and Biological Effects. *Physics Reports* **2016**, *630*, 1–84. https://doi.org/10.1016/j.physrep.2016.03.003.

(89) Lu, X.; Laroussi, M. Optimization of Ultraviolet Emission and Chemical Species Generation from a Pulsed Dielectric Barrier Discharge at Atmospheric Pressure. *Journal of Applied Physics* **2005**, *98* (2), 023301. https://doi.org/10.1063/1.1980530.

(90) Gils, C. A. J. van; Hofmann, S.; Boekema, B. K. H. L.; Brandenburg, R.; Bruggeman, P. J. Mechanisms of Bacterial Inactivation in the Liquid Phase Induced by a Remote RF Cold Atmospheric Pressure Plasma Jet. *J. Phys. D: Appl. Phys.* **2013**, *46* (17), 175203. https://doi.org/10.1088/0022-3727/46/17/175203.

(91) Deng, X.; Galli, F.; Koper, M. T. M. In Situ Electrochemical AFM Imaging of a Pt Electrode in Sulfuric Acid under Potential Cycling Conditions. *J Am Chem Soc* **2018**, *140* (41), 13285–13291. https://doi.org/10.1021/jacs.8b07452.

(92) Hoeben, W. F. L. M.; van Ooij, P. P.; Schram, D. C.; Huiskamp, T.; Pemen, A. J. M.; Lukeš, P. On the Possibilities of Straightforward Characterization of Plasma Activated Water. *Plasma Chem Plasma Process* **2019**, *39* (3), 597–626. https://doi.org/10.1007/s11090-019-09976-7.

(93) Tratnyek, P. G.; Reilkoff, T. E.; Lemon, A. W.; Scherer, M. M.; Balko, B. A.; Feik, L. M.; Henegar, B. D. Visualizing Redox Chemistry: Probing Environmental Oxidation–Reduction Reactions with Indicator Dyes. *Chem. Educator* **2001**, *6* (3), 172–179. https://doi.org/10.1007/s00897010471a.

(94) Stargardt, J. F.; Hawkridge, F. M. Computer Decomposition of the Ultraviolet-Visible Absorption Spectrum of the Methyl Viologen Cation Radical and Its Dimer in Solution. *Analytica Chimica Acta* **1983**, *146*, 1–8. https://doi.org/10.1016/S0003-2670(00)80586-3.

(95) Bahnemann, D. W.; Fischer, C.-H.; Janata, E.; Henglein, A. The Two-Electron Oxidation of Methyl Viologen. Detection and Analysis of Two Fluorescing Products. *J. Chem. Soc., Faraday Trans. 1* **1987**, *83* (8), 2559–2571. https://doi.org/10.1039/F19878302559.

(96) Bader, H.; Sturzenegger, V.; Hoigné, J. Photometric Method for the Determination of Low Concentrations of Hydrogen Peroxide by the Peroxidase Catalyzed Oxidation of N,N-Diethyl-p-Phenylenediamine (DPD). *Water Research* **1988**, *22* (9), 1109–1115. https://doi.org/10.1016/0043-1354(88)90005-X.

(97) Michaelis, L.; Hill, E. S. THE VIOLOGEN INDICATORS. *J Gen Physiol* **1933**, *16* (6), 859–873.

(98) Ito, M.; Kuwana, T. Spectroelectrochemical Study of Indirect Reduction of Triphosphopyridine Nucleotide: I. Methyl Viologen, Ferredoxin-TPN-Reductase and TPN. *Journal of Electroanalytical Chemistry and Interfacial Electrochemistry* **1971**, *32* (3), 415–425. https://doi.org/10.1016/S0022-0728(71)80144-4.

(99) Bruinink, J.; Kregting, C. G. A.; Ponjeé, J. J. Modified Viologens with Improved Electrochemical Properties for Display Applications. *J. Electrochem. Soc.* **1977**, *124* (12), 1854–1858. https://doi.org/10.1149/1.2133175.

(100) Bird, C. L.; Kuhn, A. T. Electrochemistry of the Viologens. *Chem. Soc. Rev.* **1981**, *10* (1), 49–82. https://doi.org/10.1039/CS9811000049.

(101) S. Monk, P. M.; D. Fairweather, R.; D. Ingram, M.; A. Duffy, J. Evidence for the Product of the Viologen Comproportionation Reaction Being a Spin-Paired Radical Cation Dimer. *Journal of the Chemical Society, Perkin Transactions 2* **1992**, *0* (11), 2039–2041. https://doi.org/10.1039/P29920002039.

(102) Elofson, R. M.; Edsberg, R. L. Polarographic Behavior of the Viologen Indicators. *Can. J. Chem.* **1957**, *35* (7), 646–650. https://doi.org/10.1139/v57-093.

(103) Monk, P. M. S. *The Viologens: Physicochemical Properties, Synthesis, and Applications of the Salts of 4,4'-Bipyridine*; Wiley: Chichester ; New York, 1998.

(104) Heyrovský, M. The Electroreduction of Methyl Viologen. *J. Chem. Soc., Chem. Commun.* **1987**, No. 24, 1856–1857. https://doi.org/10.1039/C39870001856.

(105) Makarov, S. V.; Kudrik, E. V.; Eldik, R. van; Naidenko, E. V. Reactions of Methyl Viologen and Nitrite with Thiourea Dioxide. New Opportunities for an Old Reductant. *J. Chem. Soc., Dalton Trans.* **2002**, No. 22, 4074–4076. https://doi.org/10.1039/B209195J.

(106) Clark, C. D.; Debad, J. D.; Yonemoto, E. H.; Mallouk, T. E.; Bard, A. J. Effect of Oxygen on Linked Ru(Bpy)32+−Viologen Species and Methylviologen: A Reinterpretation of the Electrogenerated Chemiluminescence. *J. Am. Chem. Soc.* **1997**, *119* (43), 10525–10531. https://doi.org/10.1021/ja9718432.

(107) Weiss, M.; Barz, J.; Ackermann, M.; Utz, R.; Ghoul, A.; Weltmann, K.-D.; Stope, M. B.; Wallwiener, D.; Schenke-Layland, K.; Oehr, C.; Brucker, S.; Loskill, P. Dose-Dependent Tissue-Level Characterization of a Medical Atmospheric Pressure Argon Plasma Jet. *ACS Appl. Mater. Interfaces* **2019**, *11* (22), 19841–19853. https://doi.org/10.1021/acsami.9b04803.

(108) Wenzel, T.; Carvajal Berrio, D. A.; Daum, R.; Reisenauer, C.; Weltmann, K.-D.; Wallwiener, D.; Brucker, S. Y.; Schenke-Layland, K.; Brauchle, E.-M.; Weiss, M. Molecular Effects and Tissue Penetration Depth of Physical Plasma in Human Mucosa Analyzed by Contact- and Marker-Independent Raman Microspectroscopy. *ACS Appl. Mater. Interfaces* **2019**, *11* (46), 42885–42895. https://doi.org/10.1021/acsami.9b13221.

(109) Labay, C.; Roldán, M.; Tampieri, F.; Stancampiano, A.; Bocanegra, P. E.; Ginebra, M.-P.; Canal, C. Enhanced Generation of Reactive Species by Cold Plasma in Gelatin Solutions for Selective Cancer Cell Death. *ACS Appl. Mater. Interfaces* **2020**, *12* (42), 47256–47269. https://doi.org/10.1021/acsami.0c12930.

(110) Bratescu, M. A.; Cho, S.-P.; Takai, O.; Saito, N. Size-Controlled Gold Nanoparticles Synthesized in Solution Plasma. *J. Phys. Chem. C* **2011**, *115* (50), 24569–24576. https://doi.org/10.1021/jp207447c.

(111) Maguire, P.; Rutherford, D.; Macias-Montero, M.; Mahony, C.; Kelsey, C.; Tweedie, M.; Pérez-Martin, F.; McQuaid, H.; Diver, D.; Mariotti, D. Continuous In-Flight Synthesis for On-Demand Delivery of Ligand-Free Colloidal Gold Nanoparticles. *Nano Lett.* **2017**, *17* (3), 1336–1343. https://doi.org/10.1021/acs.nanolett.6b03440.

(112) Borude, R. R.; Sugiura, H.; Ishikawa, K.; Tsutsumi, T.; Kondo, H.; Ikarashi, N.; Hori, M. Single-Step, Low-Temperature Simultaneous Formations and in Situ Binding of Tin Oxide Nanoparticles to Graphene Nanosheets by In-Liquid Plasma for Potential

Applications in Gas Sensing and Lithium-Ion Batteries. *ACS Appl. Nano Mater.* **2019**, *2* (2), 649–654. https://doi.org/10.1021/acsanm.8b02201.

(113) Locke, B. R.; Sato, M.; Sunka, P.; Hoffmann, M. R.; Chang, J.-S. Electrohydraulic Discharge and Nonthermal Plasma for Water Treatment. *Ind. Eng. Chem. Res.* **2006**, *45* (3), 882–905. https://doi.org/10.1021/ie050981u.

(114) Stratton, G. R.; Dai, F.; Bellona, C. L.; Holsen, T. M.; Dickenson, E. R. V.; Mededovic Thagard, S. Plasma-Based Water Treatment: Efficient Transformation of Perfluoroalkyl Substances in Prepared Solutions and Contaminated Groundwater. *Environ. Sci. Technol.* **2017**, *51* (3), 1643–1648. https://doi.org/10.1021/acs.est.6b04215.

(115) Singh, R. K.; Fernando, S.; Baygi, S. F.; Multari, N.; Thagard, S. M.; Holsen, T. M. Breakdown Products from Perfluorinated Alkyl Substances (PFAS) Degradation in a Plasma-Based Water Treatment Process. *Environ. Sci. Technol.* **2019**, *53* (5), 2731–2738. https://doi.org/10.1021/acs.est.8b07031.

(116) Sakakura, T.; Murakami, N.; Takatsuji, Y.; Haruyama, T. Nitrogen Fixation in a Plasma/Liquid Interfacial Reaction and Its Switching between Reduction and Oxidation. *J. Phys. Chem. C* **2020**, *124* (17), 9401–9408. https://doi.org/10.1021/acs.jpcc.0c02392.

(117) Toth, J. R.; Abuyazid, N. H.; Lacks, D. J.; Renner, J. N.; Sankaran, R. M. A Plasma-Water Droplet Reactor for Process-Intensified, Continuous Nitrogen Fixation at Atmospheric Pressure. *ACS Sustainable Chem. Eng.* **2020**, *8* (39), 14845–14854. https://doi.org/10.1021/acssuschemeng.0c04432.

(118) Mizuno, T.; Akimoto, T.; Azumi, K.; Ohmori, T.; Aoki, Y.; Takahashi, A. Hydrogen Evolution by Plasma Electrolysis in Aqueous Solution. *Jpn. J. Appl. Phys.* **2005**, *44* (1R), 396. https://doi.org/10.1143/JJAP.44.396.

(119) Mota-Lima, A.; do Nascimento, J. F.; Chiavone-Filho, O.; Nascimento, C. A. O. Electrosynthesis via Plasma Electrochemistry: Generalist Dynamical Model To Explain Hydrogen Production Induced by a Discharge over Water. *J. Phys. Chem. C* **2019**, *123* (36), 21896–21912. https://doi.org/10.1021/acs.jpcc.9b04777.

(120) Rezaei, F.; Vanraes, P.; Nikiforov, A.; Morent, R.; De Geyter, N. Applications of Plasma-Liquid Systems: A Review. *Materials (Basel)* **2019**, *12* (17). https://doi.org/10.3390/ma12172751.

(121) Zhou, R.; Zhou, R.; Wang, P.; Xian, Y.; Mai-Prochnow, A.; Lu, X.; Cullen, P. J.; Ostrikov, K. (Ken); Bazaka, K. Plasma-Activated Water: Generation, Origin of Reactive Species and Biological Applications. *J. Phys. D: Appl. Phys.* **2020**, *53* (30), 303001. https://doi.org/10.1088/1361-6463/ab81cf.

(122) Oldham, T.; Chen, M.; Sharkey, S.; Parker, K. M.; Thimsen, E. Electrochemical Characterization of the Plasma-Water Interface. *J. Phys. D: Appl. Phys.* **2020**, *53* (16), 165202. https://doi.org/10.1088/1361-6463/ab6e9c.

(123) Witzke, M.; Rumbach, P.; Go, D. B.; Sankaran, R. M. Evidence for the Electrolysis of Water by Atmospheric-Pressure Plasmas Formed at the Surface of Aqueous Solutions. *J. Phys. D: Appl. Phys.* **2012**, *45* (44), 442001. https://doi.org/10.1088/0022-3727/45/44/442001.

(124) Bardwell, J. A.; Foulds, I. G.; Webb, J. B.; Tang, H.; Fraser, J.; Moisa, S.; Rolfe, S. J. A Simple Wet Etch for GaN. *Journal of Elec Materi* **1999**, *28* (10), L24–L26. https://doi.org/10.1007/s11664-999-0254-0.

(125) Hwang, Z. H.; Hwang, J. M.; Hwang, H. L.; Hung, W. H. Electrodeless Wet Etching of GaN Assisted with Chopped Ultraviolet Light. *Appl. Phys. Lett.* **2004**, *84* (19), 3759–3761. https://doi.org/10.1063/1.1737799.

(126) Green, R. T.; Tan, W. S.; Houston, P. A.; Wang, T.; Parbrook, P. J. Investigations on Electrode-Less Wet Etching of GaN Using Continuous Ultraviolet Illumination. *Journal of Elec Materi* **2007**, *36* (4), 397–402. https://doi.org/10.1007/s11664-006-0070-8.

(127) Eisenberg, G. Colorimetric Determination of Hydrogen Peroxide. *Ind. Eng. Chem. Anal. Ed.* **1943**, *15* (5), 327–328. https://doi.org/10.1021/i560117a011.

(128) McDonnell-Worth, C.; MacFarlane, D. R. Ion Effects in Water Oxidation to Hydrogen Peroxide. *RSC Adv.* **2014**, *4* (58), 30551–30557. https://doi.org/10.1039/C4RA05296J.

(129) Siahrostami, S.; Li, G.-L.; Viswanathan, V.; Nørskov, J. K. One- or Two-Electron Water Oxidation, Hydroxyl Radical, or H2O2 Evolution. *J. Phys. Chem. Lett.* **2017**, *8* (6), 1157–1160. https://doi.org/10.1021/acs.jpclett.6b02924.

(130) Shi, X.; Siahrostami, S.; Li, G.-L.; Zhang, Y.; Chakthranont, P.; Studt, F.; Jaramillo, T. F.; Zheng, X.; Nørskov, J. K. Understanding Activity Trends in Electrochemical Water Oxidation to Form Hydrogen Peroxide. *Nat Commun* **2017**, *8* (1), 701. https://doi.org/10.1038/s41467-017-00585-6.

(131) Spitler, M. T.; Modestino, M. A.; Deutsch, T. G.; Xiang, C. X.; Durrant, J. R.; Esposito, D. V.; Haussener, S.; Maldonado, S.; Sharp, I. D.; Parkinson, B. A.; Ginley, D. S.; Houle, F. A.; Hannappel, T.; Neale, N. R.; Nocera, D. G.; McIntyre, P. C. Practical Challenges in the Development of Photoelectrochemical Solar Fuels Production. *Sustainable Energy Fuels* **2020**, *4* (3), 985–995. https://doi.org/10.1039/C9SE00869A.

(132) Bosque, I.; Magallanes, G.; Rigoulet, M.; Kärkäs, M. D.; Stephenson, C. R. J. Redox Catalysis Facilitates Lignin Depolymerization. *ACS Cent. Sci.* **2017**, *3* (6), 621–628. https://doi.org/10.1021/acscentsci.7b00140.

(133) Iniesta, J. Electrochemical Oxidation of Phenol at Boron-Doped Diamond Electrode. *Electrochimica Acta* **2001**, *46* (23), 3573–3578. https://doi.org/10.1016/S0013-4686(01)00630-2.

(134) Feng, Y.; Yang, L.; Liu, J.; Logan, B. E. Electrochemical Technologies for Wastewater Treatment and Resource Reclamation. *Environ. Sci.: Water Res. Technol.* **2016**, *2* (5), 800–831. https://doi.org/10.1039/C5EW00289C.

(135) Scholtz, V.; Pazlarova, J.; Souskova, H.; Khun, J.; Julak, J. Nonthermal Plasma — A Tool for Decontamination and Disinfection. *Biotechnology Advances* **2015**, *33* (6, Part 2), 1108–1119. https://doi.org/10.1016/j.biotechadv.2015.01.002.

(136) Hawtof, R.; Ghosh, S.; Guarr, E.; Xu, C.; Mohan Sankaran, R.; Renner, J. N. Catalyst-Free, Highly Selective Synthesis of Ammonia from Nitrogen and Water by a Plasma Electrolytic System. *Science Advances 5* (1), eaat5778. https://doi.org/10.1126/sciadv.aat5778.

(137) Čechová, L.; Krčma, F.; Kalina, M.; Man, O.; Kozáková, Z. Preparation of Silver and Gold Nanoparticles by the Pinhole DC Plasma System. *Journal of Applied Physics* **2021**, *129* (23), 233304. https://doi.org/10.1063/5.0044054.

(138) Bruggeman, P. J.; Frontiera, R. R.; Kortshagen, U. R.; Kushner, M. J.; Linic, S.; Schatz, G. C.; Andaraarachchi, H.; Exarhos, S.; Jones, L. O.; Mueller, C. M.; Rich, C. C.; Xu, C.; Yue, Y.; Zhang, Y. Plasma-Driven Solution Electrolysis. *Journal of Applied Physics* **2021**, *129* (20), 200902. https://doi.org/10.1063/5.0044261.

(139) *Dusty Plasmas: Physics, Chemistry, and Technological Impacts in Plasma Processing*; Bouchoule, A., Ed.; Wiley: Chichester ; New York, 1999.

(140) Kempkens, H.; Uhlenbusch, J. Scattering Diagnostics of Low-Temperature Plasmas (Rayleigh Scattering, Thomson Scattering, CARS). *Plasma Sources Sci. Technol.* **2000**, *9* (4), 492–506. https://doi.org/10.1088/0963-0252/9/4/305.

(141) Sande, M. van de; Sande, M. J. van de. *Laser Scattering on Low Temperature Plasmas: High Resolution and Stray Light Rejection*; Technische Universiteit Eindhoven: Eindhoven, 2002.

(142) *Plasma Scattering of Electromagnetic Radiation: Experiment, Theory and Computation*, 1st ed.; Sheffield, J., Ed.; Elsevier: Amsterdam ; Boston, 2011.

(143) Marshall, K. A.; Hieftje, G. M. Measurement of True Gas Kinetic Temperatures in an Inductively Coupled Plasma by Laser-Light Scattering. Plenary Lecture. *J. Anal. At. Spectrom.* **1987**, *2* (6), 567–571. https://doi.org/10.1039/JA9870200567.

(144) Vaughan, G.; Wareing, D. P.; Pepler, S. J.; Thomas, L.; Mitev, V. Atmospheric Temperature Measurements Made by Rotational Raman Scattering. *Appl. Opt., AO* **1993**, *32* (15), 2758–2764. https://doi.org/10.1364/AO.32.002758.

(145) Belostotskiy, S. G.; Wang, Q.; Donnelly, V. M.; Economou, D. J.; Sadeghi, N. Three-Dimensional Gas Temperature Measurements in Atmospheric Pressure Microdischarges Using Raman Scattering. *Appl. Phys. Lett.* **2006**, *89* (25), 251503. https://doi.org/10.1063/1.2404594.

(146) Palomares, J. M.; Iordanova, E.; van Veldhuizen, E. M.; Baede, L.; Gamero, A.; Sola, A.; van der Mullen, J. J. A. M. Thomson Scattering on Argon Surfatron Plasmas at Intermediate Pressures: Axial Profiles of the Electron Temperature and Electron Density. *Spectrochimica Acta Part B: Atomic Spectroscopy* **2010**, *65* (3), 225–233. https://doi.org/10.1016/j.sab.2010.03.001.

(147) Gessel, A. F. H. van; Carbone, E. A. D.; Bruggeman, P. J.; Mullen, J. J. A. M. van der. Laser Scattering on an Atmospheric Pressure Plasma Jet: Disentangling Rayleigh, Raman and Thomson Scattering. *Plasma Sources Sci. Technol.* **2012**, *21* (1), 015003. https://doi.org/10.1088/0963-0252/21/1/015003.

(148) Penney, C. M.; St. Peters, R. L.; Lapp, M. Absolute Rotational Raman Cross Sections for N_2, O_2, and CO_2. *J. Opt. Soc. Am.* **1974**, *64* (5), 712. https://doi.org/10.1364/JOSA.64.000712.

(149) Obrusník, A.; Synek, P.; Hübner, S.; Mullen, J. J. A. M. van der; Zajíčková, L.; Nijdam, S. Coherent and Incoherent Thomson Scattering on an Argon/Hydrogen Microwave Plasma Torch with Transient Behaviour. *Plasma Sources Sci. Technol.* **2016**, *25* (5), 055018. https://doi.org/10.1088/0963-0252/25/5/055018.

(150) Benilov, M. S.; Coulombe, S. Modeling a Collision-Dominated Space-Charge Sheath in High-Pressure Arc Discharges. *Physics of Plasmas* **2001**, *8* (9), 4227–4233. https://doi.org/10.1063/1.1387473.

(151) Benilov, M. S. The Child–Langmuir Law and Analytical Theory of Collisionless to Collision-Dominated Sheaths. *Plasma Sources Sci. Technol.* **2009**, *18* (1), 014005. https://doi.org/10.1088/0963-0252/18/1/014005.

(152) Langmuir, I. The Effect of Space Charge and Residual Gases on Thermionic Currents in High Vacuum. *Phys. Rev.* **1913**, *2* (6), 450–486. https://doi.org/10.1103/PhysRev.2.450.

(153) Oskam, H. J.; Mittelstadt, V. R. Ion Mobilities in Helium, Neon, and Argon. *Phys. Rev.* **1963**, *132* (4), 1435–1444. https://doi.org/10.1103/PhysRev.132.1435.

(154) *Handbuch Vakuumtechnik*, 12., neu bearbeitete Auflage.; Jousten, K., Ed.; Springer Reference Technik; Springer Vieweg: Wiesbaden [Heidelberg], 2018.
(155) Li, S.-Z.; Lim, J.-P.; Kang, J. G.; Uhm, H. S. Comparison of Atmospheric-Pressure Helium and Argon Plasmas Generated by Capacitively Coupled Radio-Frequency Discharge. *Physics of Plasmas* **2006**, *13* (9), 093503. https://doi.org/10.1063/1.2355428.
(156) Hughes, T. P. *Plasmas and Laser Light*; Wiley: New York, 1975.
(157) Bivona, S.; Daniele, R.; Ferrante, G. Laser-Assisted Inverse Bremsstrahlung in a Weakly Ionised Plasma. *J. Phys. B: Atom. Mol. Phys.* **1982**, *15* (10), 1585–1599. https://doi.org/10.1088/0022-3700/15/10/018.
(158) Carbone, E. A. D.; Palomares, J. M.; Hübner, S.; Iordanova, E.; Mullen, J. J. A. M. van der. Revision of the Criterion to Avoid Electron Heating during Laser Aided Plasma Diagnostics (LAPD). *J. Inst.* **2012**, *7* (01), C01016–C01016. https://doi.org/10.1088/1748-0221/7/01/C01016.
(159) Raizer, Y. P. S.; Mikhail N. Yatsenko, N. A. *Radiofrequency Capacitive Discharges.*; CRC Press: Boca Raton, FL, 1995.
(160) Goldston, R. J.; Rutherford, P. H. *Introduction to Plasma Physics*; Institute of Physics Pub: Bristol, UK ; Philadelphia, 1995.
(161) *Dusty Plasmas: Physics, Chemistry, and Technological Impacts in Plasma Processing*; Bouchoule, A., Ed.; Wiley: Chichester ; New York, 1999.
(162) Hutchinson, I. H. *Principles of Plasma Diagnostics*, 2nd ed.; Cambridge University Press: Cambridge ; New York, 2002.
(163) Roth, J. R. *Industrial Plasma Engineering*; Institute of Physics Pub: Bristol ; Philadelphia, 1995.
(164) Roth, J. R. *Industrial Plasma Engineering. 2: Applications to Nonthermal Plasma Processing*; Institute of Physics: Bristol, 2001.